

University of Nevada, Reno

**Petrography And Geochemistry Of Hypogene Mineralization at the Mike Gold -
Copper Deposit, Eureka County, Nevada**

A thesis submitted in partial fulfillment of the requirements for a Masters of
Science degree in Geology.

by

Benjamin M. Parrish

Dr. Tommy B. Thompson/Thesis Advisor

August, 2014

Copyright by Benjamin M. Parrish 2014

All Rights Reserved



THE GRADUATE SCHOOL

We recommend that the thesis
prepared under our supervision by

BENJAMIN M. PARRISH

Entitled

**Petrography And Geochemistry Of Hypogene Mineralization At The Mike Gold -
Copper Deposit, Eureka County, Nevada**

be accepted in partial fulfillment of the
requirements for the degree of

MASTER OF SCIENCE

Tommy B. Thompson, Ph.D., Advisor

Peter Vikre, Ph.D., Committee Member

Thom Seal, Ph.D., Graduate School Representative

David W. Zeh, Ph.D., Dean, Graduate School

August, 2014

Abstract

The Mike Carlin-type gold and copper deposit is an exploration property within the central Carlin trend, 9 miles northwest of the town of Carlin in Eureka County, Nevada. The deposit is hosted in Paleozoic lower-plate rocks in the Carlin window, a fenster in the Roberts Mountains allochthon, and is localized along the Good Hope fault and Tusc Corridor in the historic Maggie Creek mining district. Gold and copper mineralization is localized along the intersection of northeast-striking faults that intersect the northwest-striking Good Hope fault, and is stratigraphically controlled. The deposit is characterized by an extensive leached zone of iron and copper oxide minerals where supergene copper enrichment has occurred at paleo-water table levels. Previous work has been done in the form of a master's thesis and Newmont reports to characterize the geology of the Mike deposit as well as mineralogy and distribution of supergene copper. The primary focus of this thesis is characterization of the unoxidized portion of the Mike deposit to determine the primary source of hypogene copper through bulk deposit geochemistry and petrographic analysis of sulfide minerals. This thesis focuses on statistical analysis of geochemical data sets and petrographic analysis of ore and gangue mineralogy and textures. Combined data from multiple Spearman coefficient correlation matrices, correspondence analysis, and principal component analysis confirm a strong association between gold, silver, arsenic, antimony, thallium and lesser association with tellurium. Notable correlations also exist between copper, bismuth, tin, tellurium, and tungsten and moderate correlations between lead, silver, and molybdenum. Geochemical correlation patterns of gold are similar to those of other Carlin-type gold deposits where gold

correlates with arsenic, antimony, and thallium, though the Mike deposit gold also shows correlations with silver and tellurium. Copper correlations suggest a magmatic source of hypogene copper based on bismuth, tin, and tungsten associations with copper and indicates that the copper and gold ore events are discrete. Petrographic analysis has identified silicification and carbonatization replacement textures as well as open space quartz vein textures, skarn, and hornfels. Identified gangue minerals include quartz, multiple carbonate phases, sericite, smectite, kaolinite, adularia, wollastonite, chondrodite, magnetite, vesuvianite, epidote, diopside, hematite, and goethite. Sulfide ore-related mineral phases include chalcopyrite, bornite, chalcocite, covellite, digenite, pyrrotite, bourmonite, marcasite, and pyrite. Petrographic observations indicate that copper, zinc, and lead sulfides post-date Carlin-type gold mineralization, which is in the form of arsenic-rich pyrite. $\delta^{34}\text{S}$ analyses implies an igneous source for base metal sulfides with some assimilation of sedimentary sulfur, and depositional temperature range of sphalerite and galena between $401^\circ\text{C} - 355^\circ\text{C} \pm 20^\circ$. Qualitative examination of base metal sulfide and Carlin-type pyrite rims by SEM-EDS analysis shows minor arsenic enrichment in rims and overgrowths on pyrite where base metals are also present, supporting paragenetic interpretations.

Acknowledgements

I would like to take the time to thank those that were involved in helping me in the completion of my thesis. Specifically, I would like to thank Dr. Tommy Thompson for his advisement, guidance, and mentorship through my coursework at UNR and during my thesis work.

I would also like to thank the members of my committee, Dr. Peter Vikre and Dr. Thom Seal for their help through the thesis process by suggesting different analytical techniques and being available to answer my questions about the thesis. Dr. John Muntean and the CREG program also have my sincere thanks for their financial support for analyses.

Rachel Burgess and Dr. Mike Ressel from Newmont, along with many other Newmont geologists and employees, played large roles in helping me to navigate my way through the large amounts of quality data and my summer field season on the Carlin trend. This thesis would not have been possible without their continued support.

Dr. Jim Carr and Dr. Mark Coolbaugh have my sincere thanks for their invaluable assistance in helping me to understand certain geostatistical methods and principles. Their help allowed me to better perform quality bulk geochemical analysis and understand methods to working with increasingly large geochemical and geostatistical datasets.

Finally, I would like to thank my friends and family for their continued, immeasurable support. Thank you Dad, for instilling in me a wonderment and awe for

the power of nature and all its beauty. Without your gentle guidance, I would not have discovered the wonderful science of geology, and I am indebted to you for everything I have become. And Arielle, without whom I would not have been able to accomplish my goals. Your love, wisdom, and patience, as well as your no-nonsense attitude, have propelled me to strive ever higher to reach my potential and complete this thesis.

Table of Contents

Abstract.....	i
Acknowledgements.....	iii
Table of Contents.....	v
List of Tables.....	viii
List of Figures.....	ix
Introduction.....	1
Exploration History and Discovery.....	3
Previous Research.....	4
Regional and Deposit Geology.....	5
Stratigraphy.....	8
Roberts Mountains Formation:.....	8
Popovich Formation:.....	9
Rodeo Creek Unit:.....	9
Tertiary Sedimentary deposits:.....	9
Structure.....	10
Faults:.....	10
Petrography.....	15
Petrographic Methodology.....	15
Alteration mineralogy and textures.....	16

Sulfide and ore mineralogy and textures:	26
SEM Analysis	38
Methods	38
SEM-EDS Results.....	38
Geochemistry	42
Geochemical Methodology.....	42
Correlation Matrices	46
Correspondence Analysis plots.....	53
Principal Component Analysis	69
Sulfur Isotope Analysis.....	78
Methods	78
$\delta^{34}\text{S}$ Results.....	78
Discussion and Conclusions	84
Petrography.....	84
Sulfide Paragenesis	85
SEM Analysis	85
Geochemistry	86
Stable S Isotopes.....	87
Future Work.....	88

Deposit Model.....	90
References.....	92

List of Tables

Table 1: Table of PCA results of data from below the leached cap.	71
Table 2: Table of PCA results from intervals below the leached cap where gold is anomalous.	73
Table 3: Table of PCA results of copper anomalous intervals below the leached cap.	75
Table 4: Table of sulfur isotope results and calculated equilibrium temperature.	79

List of Figures

Figure 1: Location map showing the Mike deposit in relation to other Carlin trend deposits and location within Nevada.	6
Figure 2: Maggie Creek District geology map.	7
Figure 3: Two cross sections from Norby and Orobona (2002) that show gold, copper oxide, and zinc metal zones at the Mike deposit and supergene-hypogene boundary.	8
Figure 4: Schematic geologic cross section of the Mike area.....	13
Figure 5: Schematic geologic cross section of the Mike area.....	14
Figure 6: Transmitted light photomicrograph of sample REB-148-1750 displaying multiple silicification quartz textures.....	17
Figure 7: Photomicrograph of sample REB-148-1750.	18
Figure 8: Photomicrograph of sample REB-148-1633 that displays open-space-filling quartz textures.....	18
Figure 9: Quartz vein texture of open-space-filling quartz grains from REB-195A-1911.	19
Figure 10: Photomicrographs and hand sample of argillic alteration of REB-149-1976.	21
Figure 11: Photomicrograph and hand sample of skarn minerals from REB-149-1445 and REB-153-1872	22
Figure 12: Photomicrographs of calc-silicate hornfels assemblage.....	24
Figure 13: Subcrop map annotated with calc-silicate hornfels locations	25
Figure 14: Reflected light photomicrograph of REB-148-1633 that shows anhedral, broken pyrite and open-space-filling quartz and adularia.....	27

Figure 15: Photomicrograph of arsenian rims on arsenopyrite taken from sample REB-199-1773.	27
Figure 16: Reflected light photomicrograph of arsenian rims on pyrite-marcasite intergrowths from sample REB-148-1443.	28
Figure 17: Two hand samples from core of pyrite morphology at the Mike deposit, associated with Carlin-type mineralization and gold.	28
Figure 18: Reflected light photomicrograph from sample REB-148-1594.	32
Figure 19: Photomicrograph of Carlin-type pyrite rims and base metal sulfides.	32
Figure 20: Reflected light photomicrograph of sample REB-153-1670.	33
Figure 21: Core photo and macroscopic hand sample showing location for Figures 22 and 24.	33
Figure 22: Photomicrograph of Carlin and base metal mineralization in REB-195A-1911	34
Figure 23: Photomicrograph of pyrite with arsenian pyrite rims printed over by sphalerite from sample REB-199-1773	34
Figure 24: Photomicrograph of sample REB-195A-1911 showing Carlin-style arsenian pyrite rims and base metal sulfides	35
Figure 25: Photomicrograph from REB-153-1978 of arsenian rim on pyrite core and base metal sulfides.	35
Figure 26: Photomicrograph from sample REB-199-1773 showing base metal sulfides in relation to arsenian rims on fractured pyrite.	36
Figure 27: Photomicrograph from REB-199-1773 showing base metal sulfide textures.	36

Figure 28: Photomicrograph of sample REB-199-1773 showing base metal sulfide textures.....	37
Figure 29: Photomicrograph of sample REB-153-1831 that showing copper sulfide intergrowths.	37
Figure 30: Annotated photomicrographs of REB-195A-1911 selected for SEM analysis and relevant SEM-EDS plots.....	39
Figure 31: Photomicrograph and qualitative plots from SEM-EDS analysis of REB-153-1978 including grayscale image of the sample.	41
Figure 32: Spearman correlation matrix of bulk deposit multi-element ICP data.....	49
Figure 33: Spearman correlation for data below the leached cap.....	50
Figure 34: Spearman correlation of ICP data from gold anomalous intervals below the leached cap.....	51
Figure 35: Spearman correlation for ICP data from copper intervals >700ppm below the leached cap.....	52
Figure 36: Correspondence analysis plot of factors 1 and 2 for all intervals below the oxide zone.....	57
Figure 37: Correspondence analysis factor plot for factors 1 and 3 from data below the leached cap.....	58
Figure 38: Correspondence analysis of below leach cap factor plot for factors 2 and 3 with elements of interest circled.	59
Figure 39: Correspondence analysis plot of factors 1 and 2 of elevated gold values below the oxide zone.....	60

Figure 40: Correspondence plot of factors 2 and 3 for anomalous gold values below the oxide zone.	61
Figure 41: Correspondence analysis plot of factors 1 and 3 for anomalous gold values below the oxide zone..	62
Figure 42: Correspondence analysis plot of factors 1 and 4 for intervals below the oxide zone with anomalous gold.	63
Figure 43: Correspondence analysis plot for anomalous gold intervals below the leached cap.	64
Figure 44: Correspondence analysis plot for intervals with anomalous copper. Plot of factors 1 and 2 with elements of interest circled.....	65
Figure 45: Correspondence analysis plot for factors 2 and 3 from data below the leach cap where copper is anomalous..	66
Figure 46: Correspondence analysis of anomalous copper intervals below leach cap. Plot of factors 1 and 3 with elements of interest circled.	67
Figure 47: Correspondence plot of anomalous copper intervals below leach cap. Plot of factors 1 and 4 with elements of interest circled.....	68
Figure 48: Spatial plot of PC2 from PCA of data below the leached cap. enclosures of PC2 with annotated low (blue) and high (brown) grade gold shells.....	76
Figure 49: Spatial plot of PC3 from analysis of data below the leached cap.	77
Figure 50: Range of $\delta^{34}\text{S}$ values for sedimentary and igneous rocks as well as meteorites. (Ohmoto and Rye, 1979).....	80
Figure 51: Figure showing measured sulfur isotope values for sulfides and sulfates from specific porphyry copper deposits (Ohmoto and Rye, 1979)	81

Figure 52: Table of geothermometry equations for sulfide pairs from Ohmoto and Rye (1979).....	82
Figure 53: Modified figure from Cline et al. (2005) that shows aggregated sulfur isotope values for three parts of the Carlin trend.. ..	83
Figure 54: Interpreted paragenetic diagram of hypogene sulfide and abundant gangue minerals at the Mike deposit based on petrographic analysis.....	85

Introduction

The Mike deposit is a gold-copper deposit located along the Carlin trend 9 miles northwest of Carlin, NV and is a Newmont property (Fig. 1). The deposit is located along the Good Hope reverse fault within the Tusc corridor of the Maggie Creek mining district (Fig. 2). The deposit has undergone extensive deformation, alteration, and oxidation, making previous attempts to establish paragenetic relationships between gold and copper mineralization difficult. Mike has been evaluated previously, including a master's thesis that addressed supergene copper concentration within the deposit (Bawden, 2002) and by a GSN publication in 2002 that describes the characteristics of the Mike deposit (Norby and Orobona, 2002), but a study has not been carried out on the hypogene portions of the deposit. The main objectives of this thesis project are: (1) Determining hypogene ore and alteration assemblage mineralogy and paragenesis; (2) bulk deposit geochemistry of the deposit; and (3) trace element spatial distribution. This thesis is not only important in helping to determine the genesis of copper and base metals at the Mike deposit, but also serves to help in the understanding of district scale geologic history in the context of magmatic-related base metal enrichment.

Carlin-type gold deposits have been described in depth in summary papers by Hofstra and Cline (2000) and Cline et al. (2005). Carlin-type gold deposits are large, bulk disseminated gold deposits hosted primarily in carbonaceous silty limestones. Gold is hosted in arsenian rims on pyrite (Wells and Mullens, 1973; Cline et al., 2005). Carlin-type gold deposits are characterized by decarbonatization, argillization, and silicification

alteration styles (Hofstra and Cline, 2000). Gold mineralization at the Mike deposit is Carlin-type (Norby and Orobona, 2002).

Porphyry copper deposits have been described in detail by Titley (1982) and summarized by Guilbert and Park (1986) and John et al. (2010). Porphyry copper deposits are characterized by copper bearing sulfides localized in fracture-controlled veins and veinlets, known as stockwork. Copper mineralization can also occur as disseminations within host rocks. Mineralization is related to and hosted in silicic intrusive igneous stocks and dikes. Alteration styles include outward propylitic, phyllic, argillic, and potassic alteration. Skarn and hornfels may occur outboard of igneous rocks, and may also contain copper-base metal mineralization (John et al., 2010). Hypogene mineralization is defined as primary mineralization from ascending fluids from the source. In the hypogene parts of a porphyry copper deposit, copper occurs in the form of chalcopyrite, bornite, and enargite (John et al., 2010). Porphyry copper deposits can undergo oxidation due to fluctuations in paleo-water tables, resulting in the remobilization and concentration of copper in the form of chalcocite, cuprite, azurite, malachite, and other copper "oxides." Hematite, goethite, and jarosite are also common oxidation products (Titley, 1982). These zones of secondary, or post-mineral, concentration are referred to as supergene zones. The resulting oxide zone above the supergene zone, or blanket, and deeper hypogene mineralization is referred to as a "leached cap," (Titley, 1982). Figure 3 shows the approximate location of the supergene-hypogene boundary at the Mike deposit, which is located roughly along the Rodeo Creek unit - Popovich Formation contact at West Mike. Figure 3 also shows gold, copper oxide, and zinc bearing zones from Norby and Orobona (2002). Zinc and lead

mineralization become more dominant over copper mineralization outboard of the central porphyry copper deposit (Guilbert and Park, 1986; John et al., 2010). This feature is seen in hypogene mineralization at Mike, where chalcopyrite and bornite are less abundant than sphalerite and galena.

Exploration History and Discovery

Historical Exploration and Production

The earliest prospecting in the area coincided with the completion of the Transcontinental railroad and took place at the Good Hope mine in 1869. The shaft of the Good Hope mine crossed the Good Hope fault and targeted barite, galena, silver, and various copper carbonates (Rota, 1986). In the 1880's, copper oxide mineralization was discovered at what would be the Copper King claims approximately one mile southeast of the later discovered Mike deposit and immediately southwest of the future Tusc mine (Norby and Orobona, 2002). The Copper King Company developed the Copper King mine in 1952 and through 1958 produced 14,800 short tons of copper oxide ore that averaged 3.4% copper (Norby and Orobona, 2002).

The Occidental Minerals Corporation explored to the northwest of the Copper King mine, looking for an extension of the ore body and drilled three holes in the early 1970s. Occidental Minerals discovered a secondary copper oxide and chalcocite blanket in the Paleozoic rocks that plunged under the Tertiary Carlin Formation to the northwest, but did not define economic mineralization (Norby and Orobona, 2002). In 1989, Newmont Mining Corporation discovered the Main Mike gold deposit after a series of economic discoveries at Gold Quarry, Mac, and Tusc to the southeast during the late

1970s and 1980s (Bawden, 2002). Charles Ekburg and Robert Ryneer discovered the Main Mike deposit through tracking gold mineralization along the northwest extension of the Good Hope reverse fault from Gold Quarry and Tusc under post-mineral cover to the postulated intersection with the Soap Creek fault (Norby and Orobona, 2002). The deposit is named for Michael Wilson who, with Brian Arkell, performed follow up exploration and definition of the deposit through infill drilling. Exploration continued into 1994 and resulted in the discovery of the West Mike gold deposit and expansion of both copper and gold resources at both West and Main Mike (Norby and Orobona, 2002). Exploration once again continued after a three year hiatus in 1997 and defined the West Mike lower gold zone and expanded the West Mike copper resource as well as the discovery of a deposit-wide zinc blanket (Norby and Orobona, 2002).

Previous Research

Since the discovery of the Mike deposit, periodic evaluation has researched some of the deposit characteristics including ore hosts and controlling stratigraphy and structures. A master's thesis was completed by Bawden in 2002 that investigated the supergene enrichment of copper at the Mike deposit. He chronicled the extent of conichalcite, a rare copper arsenate mineral, and the supergene weathering profile of the Mike deposit (Bawden, 2002). In addition to this thesis, multiple Newmont annual reports, audits of geology and mineral inventories, as well as deposit summaries have contributed to knowledge of the contact metamorphic, epithermal, supergene mineral systems, and structural setting at the Mike deposit (Norby and Orobona, 2002).

Regional and Deposit Geology

District Geology

The Mike gold-copper deposit is located in Eureka County, Nevada, approximately 9 miles northwest of the town of Carlin (Fig. 1) in the Maggie Creek mining district (Fig. 2). The deposit is controlled by Newmont Mining Corporation and is located within the central part of the Carlin trend. The Mike deposit, along with Gold Quarry, Tusc, and Mac are hosted within lower-plate Devonian and Silurian carbonate and clastic rocks in the Carlin window. The Carlin window is a fenster in siliceous and carbonate-clastic Devonian to Ordovician rocks of the Roberts Mountain overthrust and is bound by high angle normal faults on the southeastern, southwestern, and northwestern flanks of the Schroeder Mountain uplift (Norby and Orobona, 2002; Bawden, 2002).

The Welches Canyon stock is located 2.3 miles southwest of the Mike deposit (Fig. 2). The stock is comprised of 37 Ma granodiorite, 38.34 ± 0.33 Ma porphyritic andesite, and 37.19 ± 0.11 Ma rhyolite dike. The Richmond stock crops out 4.2 miles to the northwest of Mike in the Tuscarora Mountains. The stock is dated at 112.4 ± 0.6 Ma and shows some similar hornfels and base metal mineralization features to those found at Mike (Norby and Orobona, 2002).

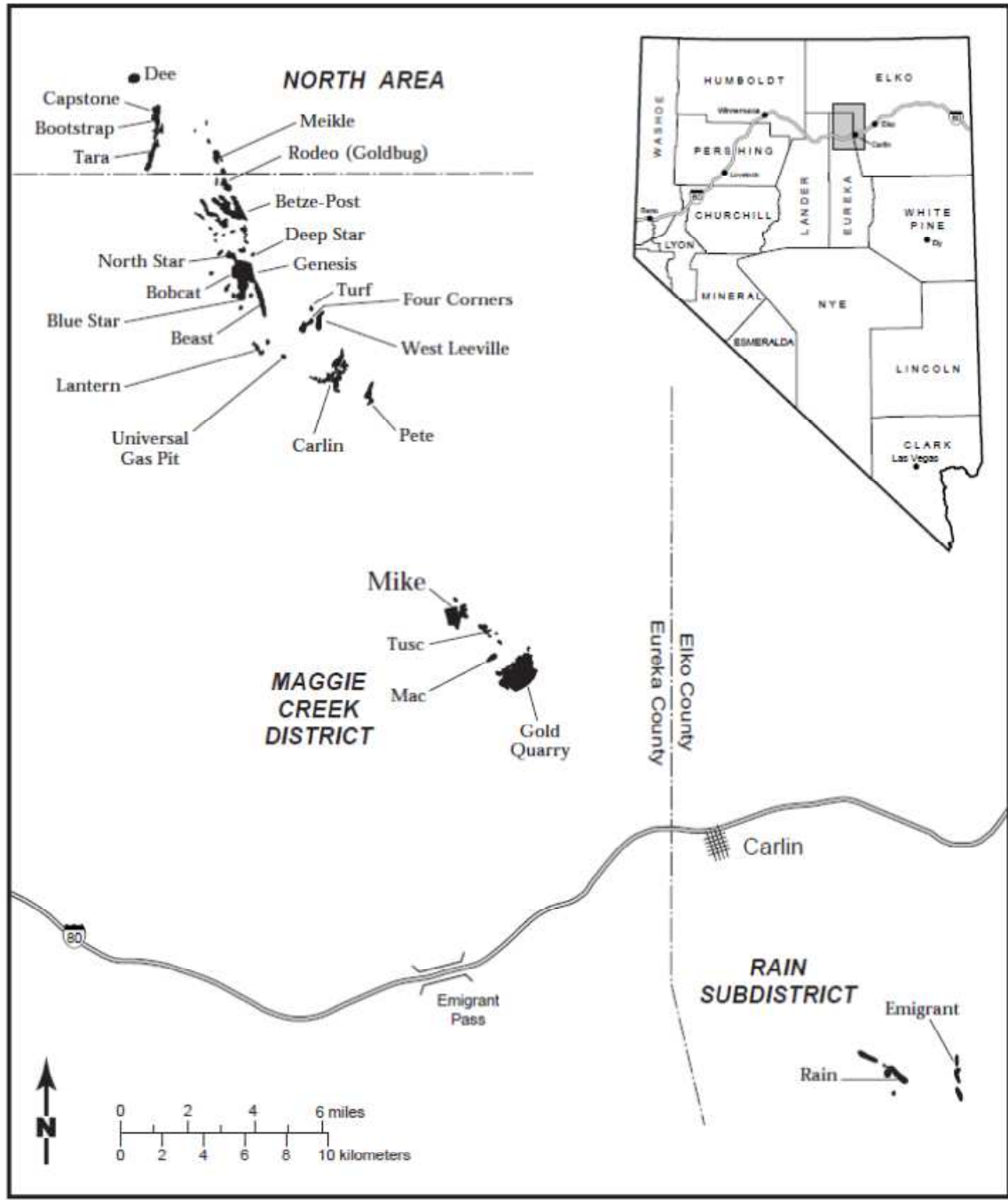


Figure 1: Location map showing the Mike deposit in relation to other Carlin trend deposits and location within Nevada. Modified from Norby and Orobona, 2002.

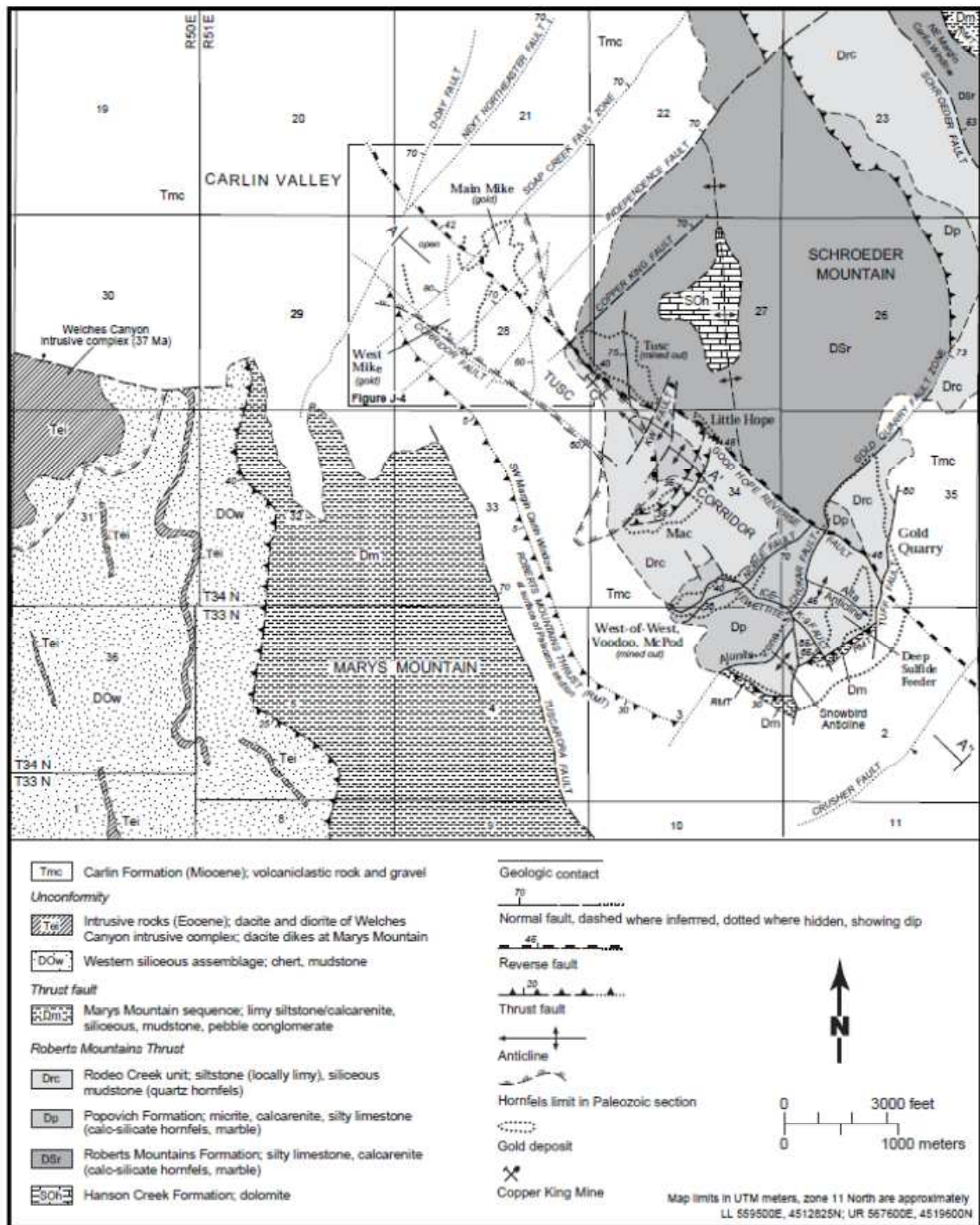


Figure 2: Maggie Creek District geology map showing major stratigraphic units, structures, and the Mike deposit within the Tusc Corridor. Modified from Norby and Orobona, 2002.

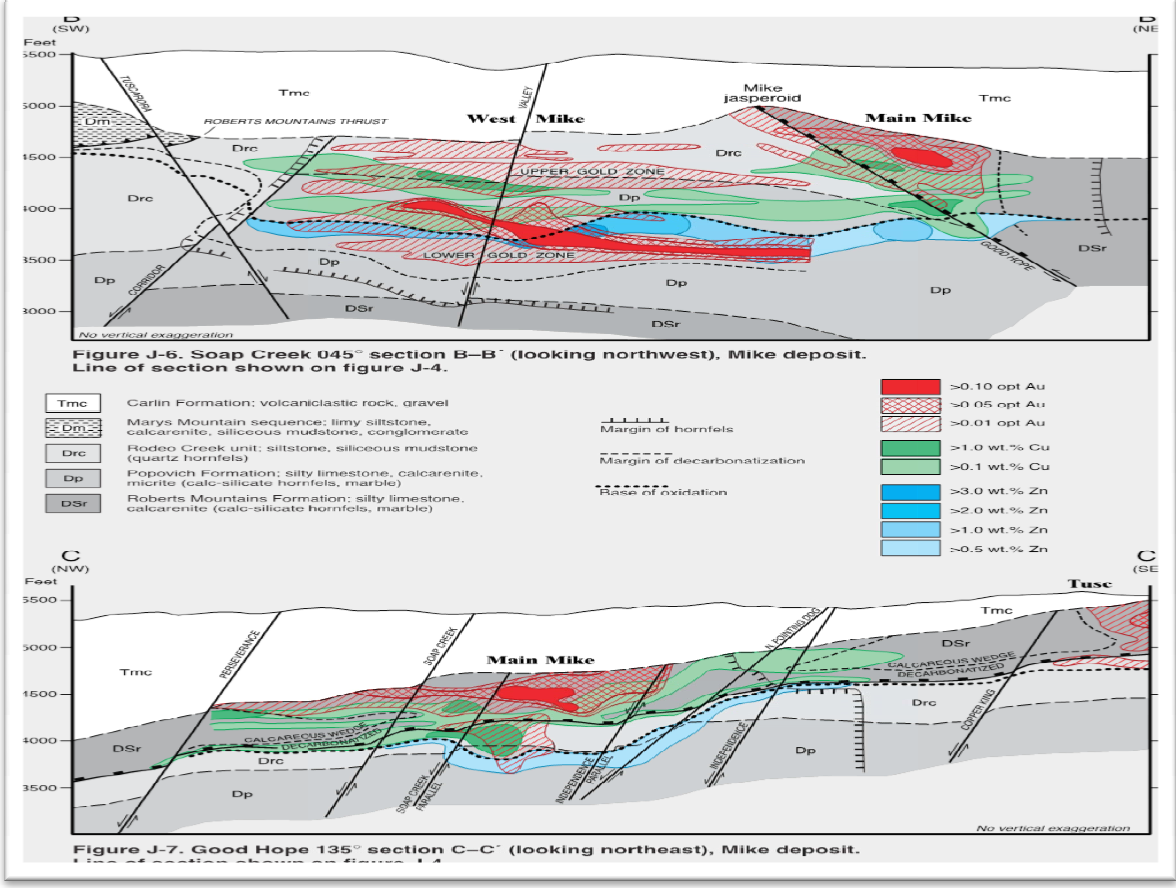


Figure 3: Two cross sections from Norby and Orobona (2002) that show gold, copper oxide, and zinc metal zones at the Mike deposit and approximated supergene-hypogene boundaries (dashed lines). Newly drilled hypogene mineralization is below this boundary.

Stratigraphy

Gold and copper mineralization at the Mike deposit is hosted in the Roberts Mountains Formation, Popovich Formation, and Rodeo Creek Unit, which are briefly described below in ascending order.

Roberts Mountains Formation: In the Maggie Creek district, the Roberts Mountains Formation is coarse grained, gray, carbonaceous, planar-laminated silty

limestone. Wispy laminated intervals in the upper Roberts Mountains Formation have proved to be an important gold host along the Carlin Trend (Norby and Orobona, 2002). The unit is 1200 to 1500 feet thick in the Maggie Creek district and dated at Early Silurian to Early Devonian. The Roberts Mountains Formation serves as a gold and secondary-copper mineral host at the Main Mike deposit (Norby and Orobona, 2002; Bawden, 2002).

Popovich Formation: The Popovich Formation is comprised of massive micrites, silty limestones, debris-flow limestones, and calcarenites. Total thickness is between 1200 to 1300 feet and the formation is Middle to Late Devonian. The Popovich Formation serves as an important gold host at Gold Quarry, and is the dominant gold, copper, and zinc host at the West Mike deposit (Norby and Orobona, 2002).

Rodeo Creek Unit: The Rode Creek unit lies above the Popovich Formation and is a medium to dark gray, planar-laminated limy siltstone. It is interbedded with thin to medium bedded siliceous mudstones in the basal portion of the section (Norby and Orobona, 2002). The Late Devonian Rodeo Creek Unit is approximately 1050 feet thick. At West Mike, between 300 and 700 feet of the unit have been eroded and the unit occurs as a brown to purple-tan planar laminated quartz hornfels. The Rodeo Creek unit is a major host of gold and secondary copper mineral at West Mike (Norby and Orobona, 2002).

Tertiary Sedimentary deposits: Lacustrine and volcanoclastic deposits rest

unconformably on Paleozoic bedrock in the Carlin Window. These units, of the Pliocene Carlin Formation, are over 900 feet thick in the area and consist of tuffaceous siltstone, conglomerate, diatomite, shale, limestone, and rhyolite tuffs (Rota, 1986).

Structure

Faults: The entire Mike deposit is covered by post-mineral volcanoclastic sediments and gravel, resulting in structural features having to be identified and interpreted through a combinations of drill-hole cross sections, lateral projections from bedrock exposures, geophysical data from gravity and magnetic surveys, and topographic lineaments (Norby and Orobona, 2002). Six fault sets have been identified and are briefly described below and are shown in the drill hole location - geologic subcrop combination map in Figure 4 as well as Figure 2.

The Roberts Mountains thrust: The Roberts Mountains thrust separates autochthonous rocks (lower plate) of the Carlin window, including all host rocks at the Mike deposit, from allochthonous rocks (upper plate). This structure is not exposed apart from within the Gold Quarry pit and its traces northwest through the Tusc corridor. Shear planes in the lower plate section are evidence of smaller, related thrusts and shear fabric seen in the Popovich Formation at West Mike. Erosion has moved the trace of the Roberts Mountains thrust to the southwest of the Mike deposit, but prior to erosion, the thrust may have been over the Carlin window and acted as an impermeable cap atop an antiform, which focused gold-bearing, hydrothermal fluid (Norby and Orobona, 2002).

The Good Hope fault: The Good Hope fault is a reverse fault that strikes between N40-50°W and dips approximately 40°E, as indicated by drill hole intersections and airborne magnetic surveys. Reverse motion has juxtaposed the hanging wall Roberts Mountains Formation against the footwall Rodeo Creek unit and drill hole data indicate a minimum of 2500 feet of throw (Norby and Orobona, 2002). Within the fault zone is a 50 to 150 foot zone of multilithic, unhealed clay-matrix fault breccia developed along several shear planes. The fault is silicified below the Mike jasperoid where it is intersected by the Soap Creek fault zone. Mafic to intermediate dikes occur in the Good Hope fault zone. Several deposits along the Tusc corridor are hosted along the Good Hope fault zone (Norby and Orobona, 2002).

The Corridor fault: The Corridor fault shows no geophysical and only minor topographic expression, and is interpreted from Newmont drill-hole cross sections. It is a 20-50 foot wide, clay-matrix breccia zone that strikes approximately N50°W and dips approximately 60°SW, showing apparent normal displacement. The Corridor fault is coincident with the southwestern limit of hornfels along the Tusc Corridor and acts as an important control for secondary copper and zinc mineralization at West Mike (Norby and Orobona, 2002).

Northeast-striking faults: A number of northeast-striking faults including the Perseverance, Soap Creek, and Independence fault zones cut the Mike deposit area (Figs. 2 and 4). Structures are spaced between 400 and 1000 feet apart, strike approximately

N40-50°E and dip 70-80°NW. These measurements are interpreted through horizontal gravity gradients and drill sections (Norby and Orobona, 2002). These faults display apparent-normal displacement in a stair-step fashion towards the northwest, collectively dropping Paleozoic bedrock more than 500 feet. Locally within the Mike deposit area, northeast-striking faults control gold mineralization and down-drop the base of oxidation, the West Mike deposit being hosted at the intersection of the Soap Creek fault zone and the Good Hope fault (Bawden, 2002; Norby and Orobona, 2002).

North-striking structures: North-striking faults predate gold mineralization at Mike and are coincident with the highest-grade gold trends of both the West Mike and main Mike deposits (Norby and Orobona, 2002). These faults include the North-Pointing Dog, Nebulous, Valley, Hillside, and D-Day faults (Figs. 2 and 4). Strikes are north to north-northeast and dip between 60-80°W and are spaced between 500 and 1000 feet apart (Norby and Orobona, 2002).

Tuscarora range-front fault zone: The Tuscarora range-front fault zone is a series of steep, northeast dipping shear planes on the southwest margin of the Tusc Corridor (Fig. 2). Apparent normal displacement increases to the northwest from the Mac deposit toward the Mike deposit area. The fault postdates gold, base metal mineralization and the oxide zone development. Thick Carlin Formation cover, upwards of 900 feet, on the northeast side of the fault presents a major geotechnical and economic challenge to the development of the Mike deposit (Norby and Orobona, 2002).

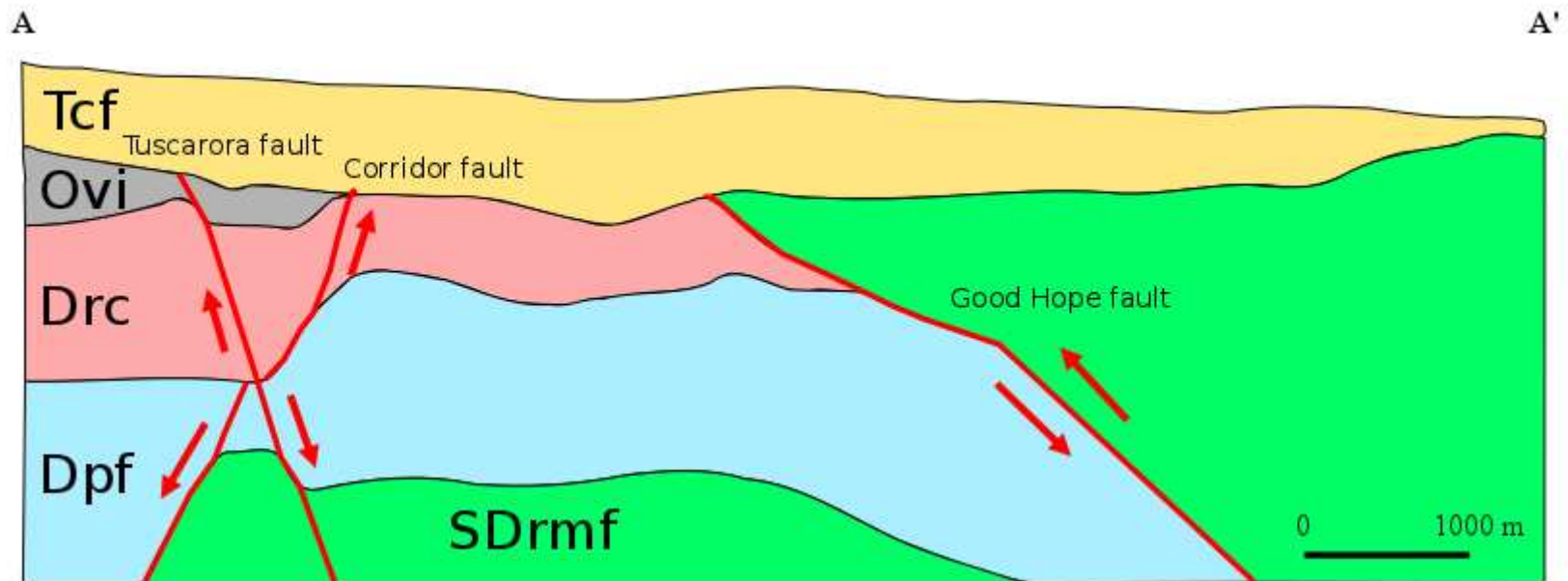


Figure 5: Schematic geologic cross section of the Mike area including lithologic contacts (Tertiary Carlin formation, Ordovician Vinini Formation (not a significant lithology at the Mike deposit), Devonian Rodeo Creek unit, Devonian Popovich, Silurian-Devonian Roberts Mountain Formations), and major faults. Looking NW, line A - A'. Created using combination of drill hole data, Newmont 3D models, and drill hole logging data in LeapFrog Geo.

Petrography

Petrographic Methodology

During the 2013 summer field season, 10 diamond drill core holes from the 2011 and 2012 Newmont infill drill campaigns were selected and relogged for the purpose of identifying samples from below the leached cap for petrographic analysis (Fig. 4). Core samples were selected to gather a representative suite of various alteration types, diversity of sulfide mineralogy and textures, and gold and copper grades. Samples were labeled according to drill hole number and footage of the sample and transported back to UNR at the end of the field season. Specific samples were then selected from all the core samples collected to be made into thin sections.

Petrologic samples were selected to create a comprehensive suite of sections for petrographic analysis that included the criteria of different alteration types, sulfide mineralogy and textures, and gold and copper grades. The samples were cut to size using the UNR rock saw lab and then sent to Spectrum Petrographics Inc. in Vancouver, WA to be made into polished thin sections. A total of 105 polished thin sections were created and paid for by a combination of CREG and Newmont Mining Corporation research funds.

Polished thin sections were examined using a combination of transmitted and reflected light in order to identify ore and gangue mineral assemblages, textures and paragenetic relationships. The samples were also examined for high temperature alteration features including texture, and mineral assemblages. During and following the petrographic study, samples were selected for SEM and sulfur isotope analysis.

Alteration mineralogy and textures

Gangue minerals at Mike are predominantly quartz and multiple varieties of carbonate minerals, both of which locally comprise nearly 90% of the rock samples. Alteration styles within the unoxidized zone at Mike consist of silica-hornfels, calc-silicate skarn, calc-silicate hornfels, and decarbonated, sericitized, silicified, or argillized rock.

Decarbonatization: Decarbonatization plays a pivotal role in Carlin type mineralization, serving as a method for increasing permeability for later mineralizing fluids to deposit metals. Decarbonatization textures are seen throughout Mike and are characterized by dissolution collapse breccias and rock that was formerly carbonate-rich that is now silicified. Decarbonated rock is a favorable host for "sooty sulfide" mineralization associated with gold deposition (Fig. 17).

Silicification: Various replacement silicification textures are present including aphanitic quartz groundmass indicative of recrystallization, and open space textures. Quartz grain sizes range from very fine microcrystalline to open-space filling prismatic quartz crystals in veins. Feathery quartz crystals are present in thin veins and veinlets (Fig. 7). Jigsaw and interlocking quartz grains are present in larger veins with and without pyrite (Figs. 6 - 9). Hydrothermal apatite is commonly associated with larger quartz grains as inclusions as well as interstitial to quartz crystals. Hydrothermal and primary quartz are pervasive throughout the host rocks at Mike, and is present in rock

matrix as well as within sulfide dominant veins, barren quartz veins, and vein breccia matrix.

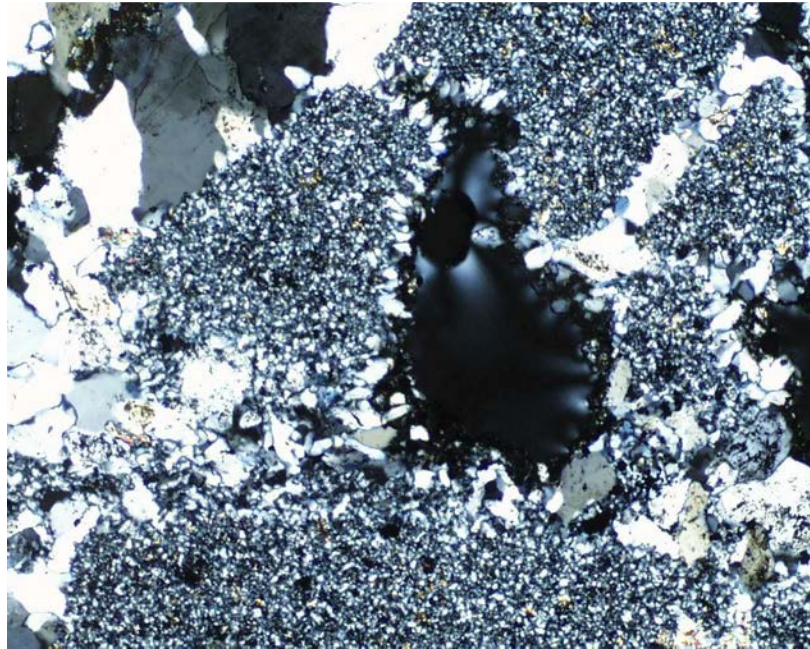


Figure 6: Transmitted light photomicrograph of sample REB-148-1750 displaying multiple silicification quartz textures including fine grained silicification, and open-space-filling prismatic quartz. Larger quartz prisms in a veinlet are in the upper left of the photo. 50X magnification, XPL.



Figure 7: Photomicrograph of sample REB-148-1750 showing feathery quartz in a veinlet juxtaposed against fine grained quartz and sericite replacement of the primary rock matrix. 50X magnification, XPL.

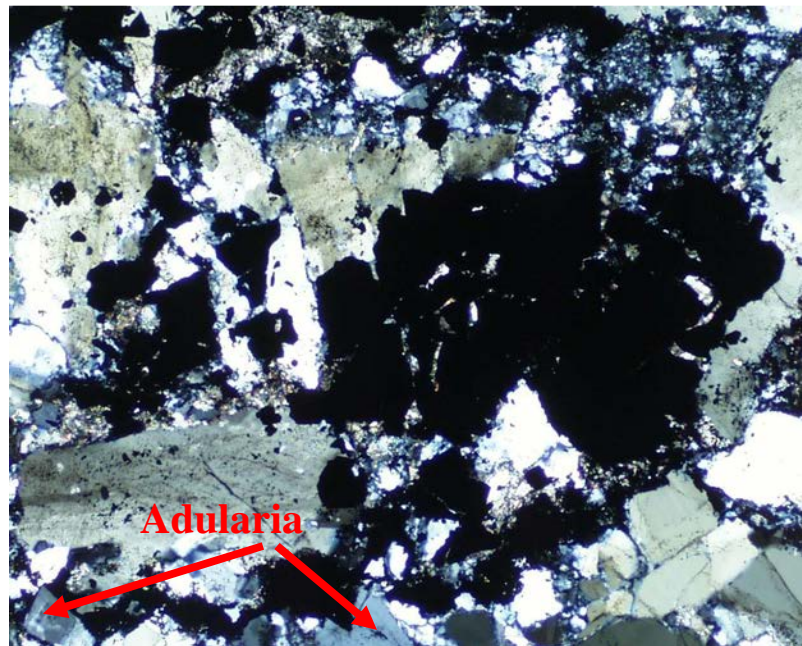


Figure 8: Photomicrograph of sample REB-148-1633 that displays open-space-filling quartz textures. Rhombohedral adularia crystals are seen in the lower left quadrant and are gray in color (annotated with red arrow). XPL transmitted light at 100X magnification.

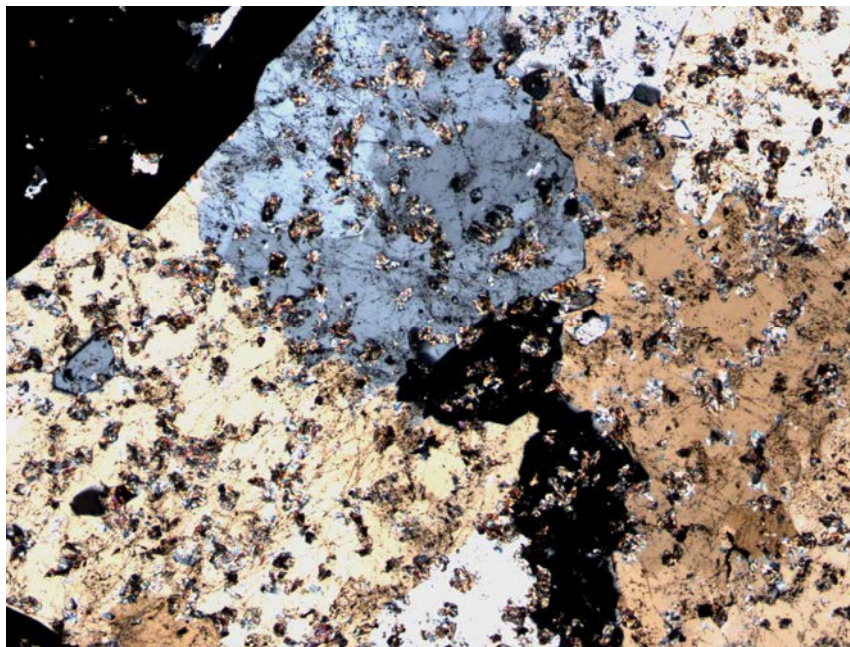


Figure 9: Quartz vein texture of open-space-filling quartz grains from REB-195A-1911. Interstitial pyrite (black) and sericite overprint quartz and pyrite. PPL transmitted light at 50X magnification and 4.32 mm FOV.

Sericitization: Fine-grained sericite is pervasive across the deposit and is present in nearly all thin sections examined. Sericite is locally interstitial to quartz crystals and fills fractures in quartz and carbonate (Fig. 9). Sericite is also common in the fringes of pyrite aggregates.

Argillization: Fine-grained clay is common as an overprint feature, and has been preliminarily identified as illite-smectite and lesser kaolinite. Clay is locally found flooding groundmass of altered rock (Fig. 10A, 10B, and 10C). Clays are found along faults and within small fractures. Argillic clay alteration is best seen as complete groundmass replacement of a lamprophyre dike from the 1970 foot level of drill hole REB-149. In this dike, the only intact primary phenocryst is magmatic biotite containing saogenitic rutile. Other phenocrysts and groundmass have been completely flooded and replaced by clay alteration (Fig. 10A - 10D). The relatively uncommon amount of

argillically altered rock within the samples of this study is likely due to the majority of the parent rock being silty limestones of the Popovich Formation. Argillic alteration is best developed within mafic to felsic dikes.

Oxides minerals are present replacing primary sulfides and magnetite and include hematite and lesser local goethite (Fig. 18). Oxides are largely absent from the intervals examined in this thesis, due to the focus being on unoxidized material from below the leached cap.

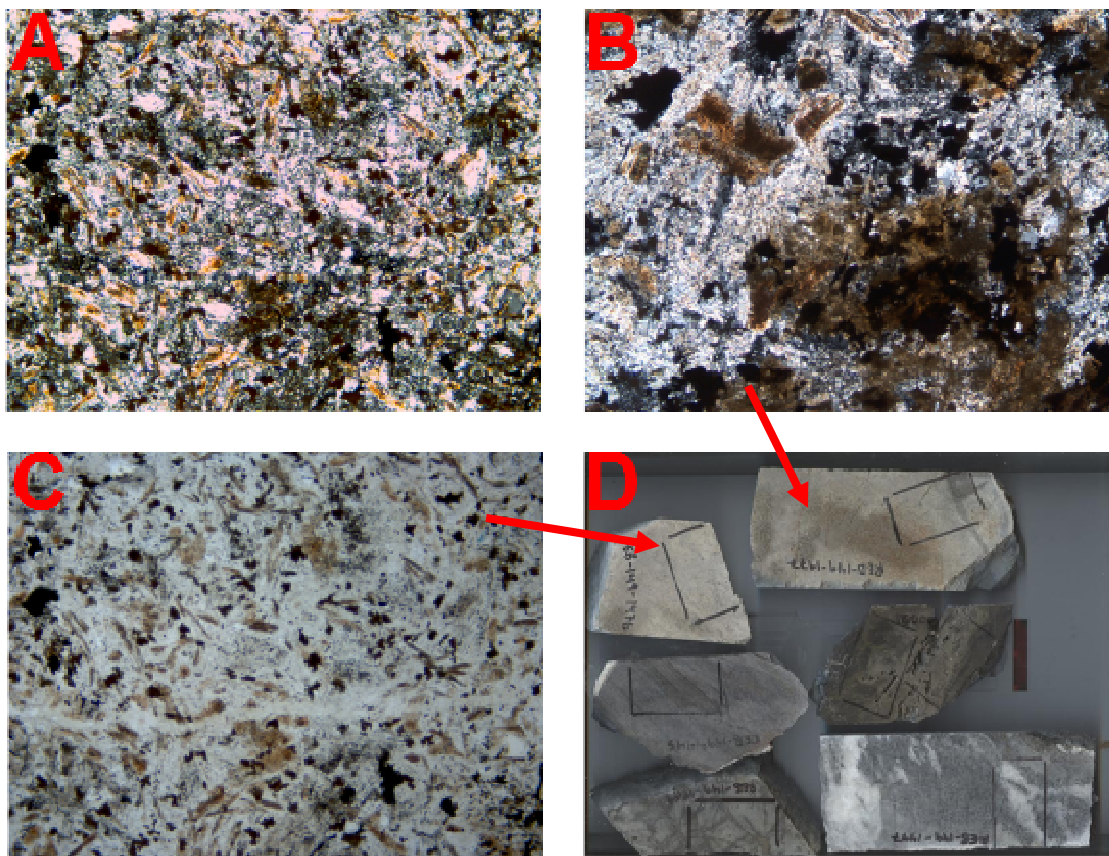


Figure 10: A: Plane transmitted light photomicrograph of argillically altered lamprophyre dike from REB-149-1976. Primary biotite grains are the only remaining phenocrysts. FOV: 2.16 mm. B: Same view as A, but in cross polarized light. High birefringent minerals are paragenetically late clay minerals around biotite phenocrysts. C. Photomicrograph of argillically altered lamprophyre dike from REB-149-1977 showing clay alteration (high birefringence) around biotite phenocrysts. Later anatase is the amorphous brown material around the opaque minerals and is only found in this sample. FOV: 1.08 mm. D: Several samples from drill hole REB-149. The Argillically altered dike is annotated by the two red arrows, and also show where photos B and C are located.

Skarn alteration: Skarn minerals are found predominantly within the northwestern-most drill holes included in this study, and highlighted in the annotated map in Figure 13. Skarn assemblage gangue minerals include calcite, wollastonite, chondrodite, rare vesuvianite, and magnetite. Wollastonite occurs in predominantly small (<1 mm) radial patches and locally as larger radiating fibrous crystals, and is found

in rock logged as "calc-silicate hornfels," by Newmont geologists. Chondrodite occurs as radiating, fibrous crystals and is a member of the wollastonite group. It has been locally replaced by calcite and pyrite along relict cleavage (Fig. 11A).

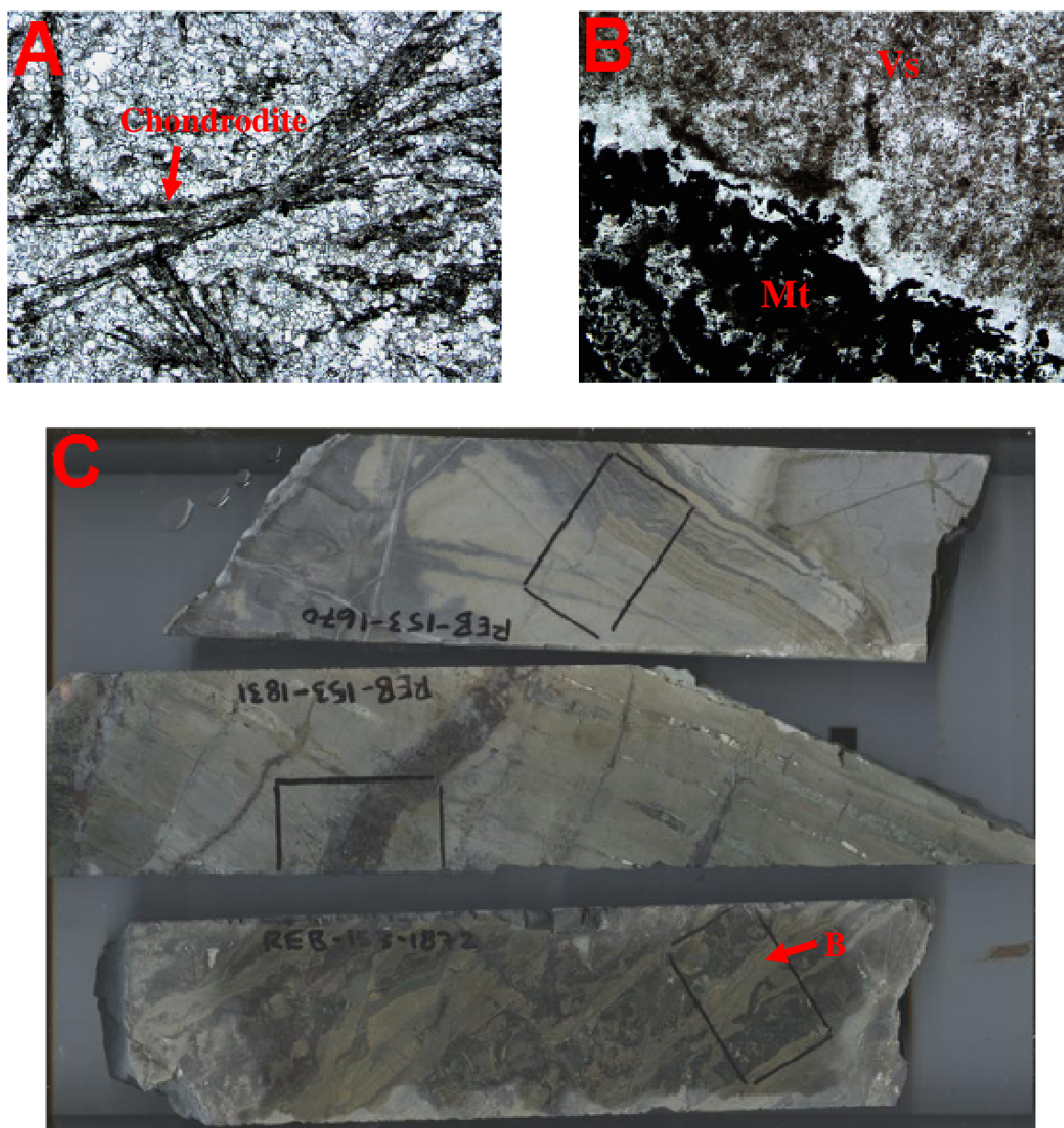


Figure 11: Skarn assemblage minerals in photomicrographs from samples A) REB-149-1445 and B) REB-153-1872. A: Chondrodite fibrous crystals replaced by carbonate (calcite) and pyrite. Plane transmitted light at 50X magnification. FOV: 4.32 mm. B: Fine aggregate of vesuvianite (Vs) (high relief, pale green to clear mineral) and interstitial magnetite (Mg) altered by later stage clay and chlorite. Plane transmitted light at 100X, FOV: 2.16 mm. C: Several samples of calc-silicate altered rocks from drill hole REB-153.

Hornfels alteration: Hornfels occurs as two main types, silica hornfels and calc-silicate hornfels. Silica hornfels intervals are comprised of intervals where the rock has undergone complete fine-grained silica and clay recrystallization. Clay is too small a size to identify optically, but is likely an illite-smectite mixture. Silica hornfels grades into calc-silicate hornfels. Calc-silicate hornfels assemblage includes epidote, calcite, and diopside and is found predominantly in the northwestern-most drill holes of this study (Fig. 13). Epidote occurs as euhedral, grains up to 1 mm in length. Diopside occurs in predominantly high relief fine-grained aggregates and as intergrowths with calcite that host euhedral epidote crystals (Figs. 12A, 12B, and 12C).

Adularia is rare, appearing in only two thin sections from one drill hole. Adularia occurs as thin bands on the edges of quartz veins as well as flooding replacement of groundmass in a hornfelsed rock with smectite. Rhombohedral grains are easily identifiable while flooding replacement makes identification more difficult (Fig. 8 and 14). Staining with sodium cobaltinitrite assists in positive identification. Adularia is likely related to calc-silicate alteration, and found in hornfelsed rocks. The best example is found in a hydrothermal vein, related to base metal mineralization.

Carbonate minerals are calcite and dolomite, though it is difficult to distinguish the two in some intervals. Another carbonate phase is intergrown with calcite and dolomite, displaying orange to pink-tinted birefringence. This carbonate mineral is possibly ferroan in composition due to iron abundance based on birefringence colors (T. Thompson, personal communication, 2014), and is also identified by Bawden (2002). Carbonate textures range from rounded, granular crystals, to large interlocking euhedra ranging from <0.5mm to >1mm. Carbonate minerals also occur as fine-grained

replacement, or flooding, of groundmass in altered rocks and are associated with calc-silicate minerals (Fig. 12A - 12C). Multiple stages of carbonate minerals are likely, as they are ubiquitous in both calc-silicate rocks, as well as associated with all sulfides.

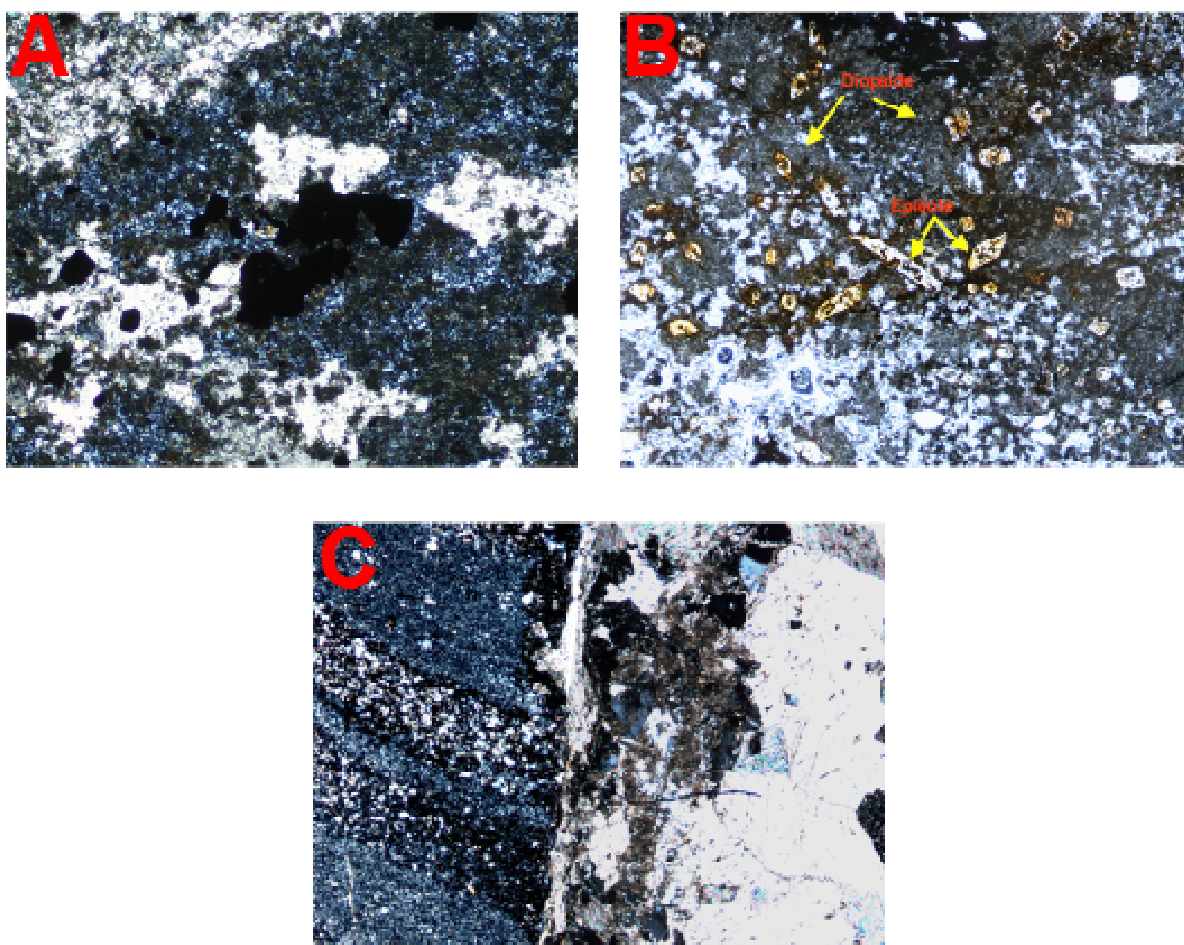


Figure 12: Photomicrographs of calc-silicate hornfels assemblage. A) Sample REB-153-1670 - white colored material is patchy carbonate. Blue-gray-green fine grained intergrown groundmass is minor K-feldspar and clay flooding, or fine-grained replacement, of groundmass interstitial to diopside (darker gray). Opaque minerals are chalcopyrite and pyrrhotite. Combined transmitted and reflected light in XPL. Photo taken at 100X magnification, FOV: 2.16 mm. B) Annotated photo of sample REB-199-1597 that shows euhedral epidote crystals in a carbonate (white zones)-diopside matrix. Diopside is aggregates of fine grained crystals 50X; FOV:4.32 mm. C) Photomicrograph of diopside-carbonate hornfels overprinting primary bedding with a large carbonate vein running through (large white patch in right of photo). 50X; FOV: 4.32mm.

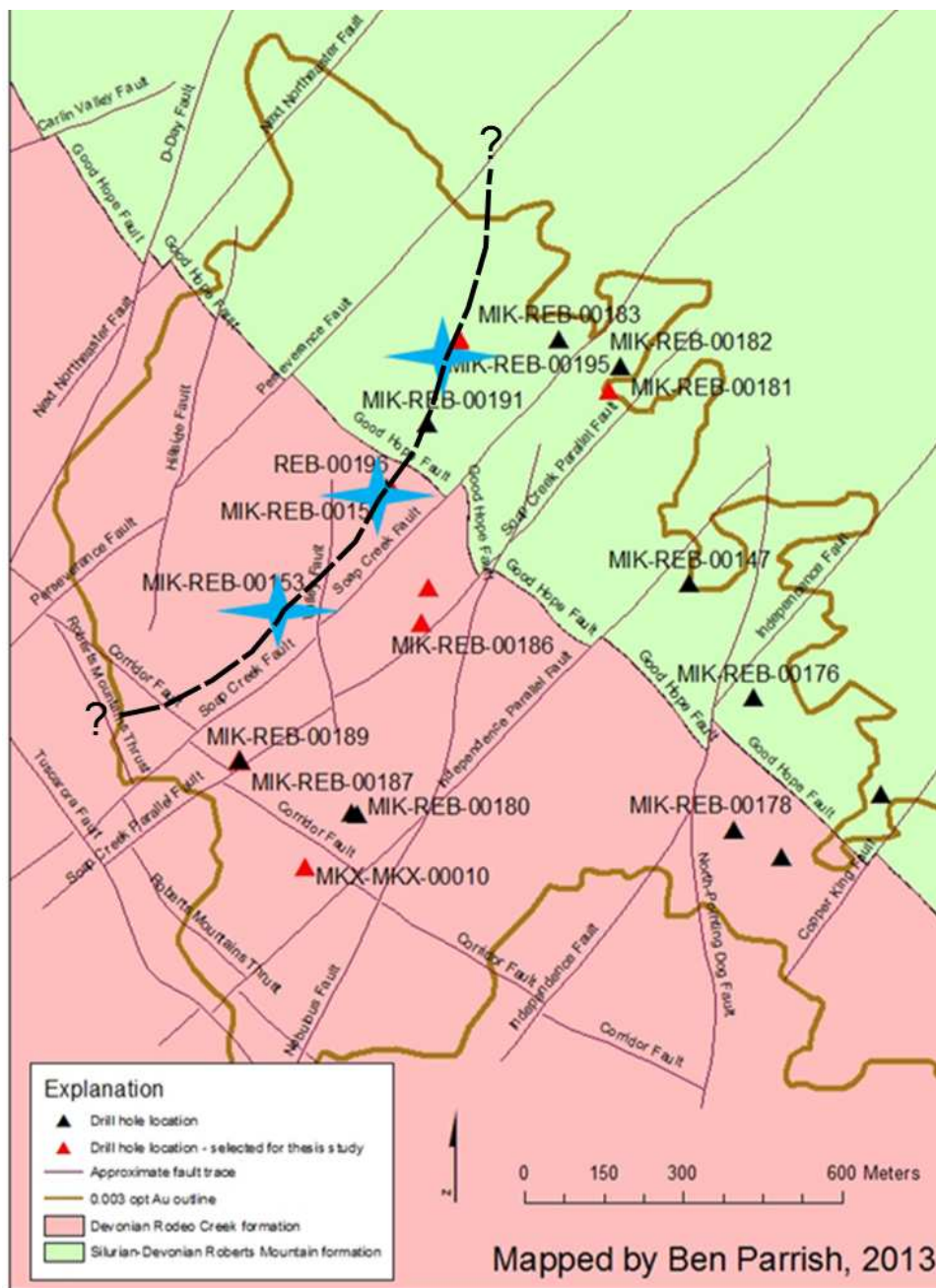


Figure 13: Previous subcrop map with stars indicating drill holes where calc-silicate hornfels and skarn alteration were positively identified and strongest. Dashed line is an approximated contact of calc-silicate alteration including calc-silicate hornfels and skarn alteration with calc-silicate alteration increasing to the northwest. Location is approximated from combined published data in Bawden (2002) and Norby and Orobona (2002) as well as Newmont data and thesis drill hole logging.

Sulfide and ore mineralogy and textures:

Sulfide minerals in the samples analyzed include pyrite, marcasite, arsenopyrite, chalcopyrite, pyrrhotite, bornite, digenite, covellite, chalcocite, sphalerite, galena, and bournonite.

Carlin-type gold stage: Pyrite and marcasite show extensive compositional variation and subsequent optical variation due to elemental substitutions. Reflected light colors for pyrite and marcasite range from pale yellow to yellow-gray to yellow-white. Bireflectance and pleochroism show considerable variability depending on compositional changes in pyrite and marcasite, and more locally within "arsenic-rich-rims." Rims on pyrite have a fine grained nature and are assumed to be where Carlin-type gold is hosted, much like the other deposits located along the Carlin Trend (Bawden, 2002) (Norby and Orobona, 2002; Cline et al., 2005). Examples of Carlin-type arsenian rims are seen in Figures 15 and 16.

Pre-ore pyrite is euhedral, and marcasite intergrowth with pyrite is commonplace (Fig. 15). Marcasite occurs as tabular crystal aggregates with or without pyrite and both marcasite and pyrite have fine grained rims of arsenic rich pyrite (Fig. 15). Both pyrite and marcasite occur as fine grained disseminations and within veins and veinlets with or without carbonate which is typical of other Carlin deposits (Fig. 17) (Cline et al., 2005). Pyrite is ubiquitous and there are likely multiple pyrite events pre-Carlin-type ore stage, post-Carlin-type ore stage, and associated with base metal mineralization as well as hydrothermal overprints upon both systems.

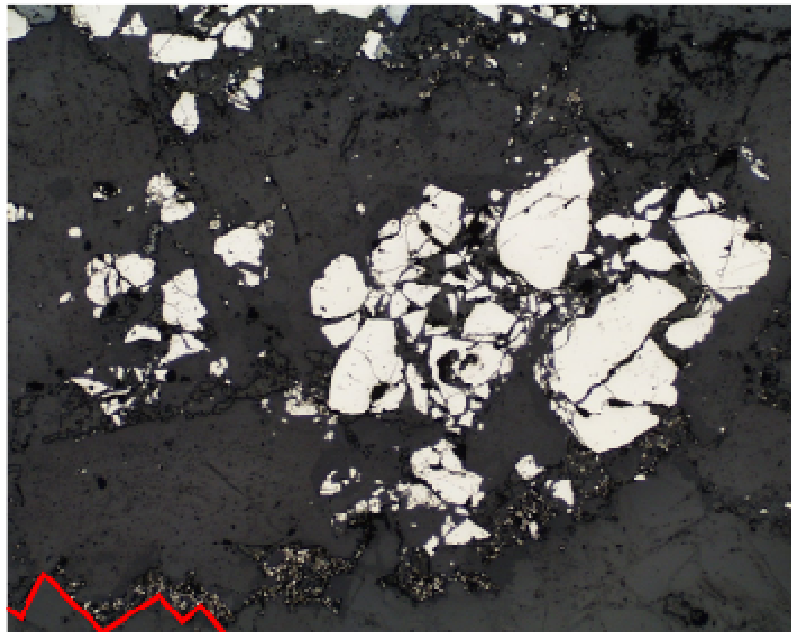


Figure 15: Reflected light photomicrograph of REB-148-1633 that shows anhedral, broken pyrite in open-space-filling quartz. Also shows fine-grained pyrite and adularia, annotated by the red outline and also seen in Figure 7. Photo was taken at 100X magnification, FOV: 2.16 mm.

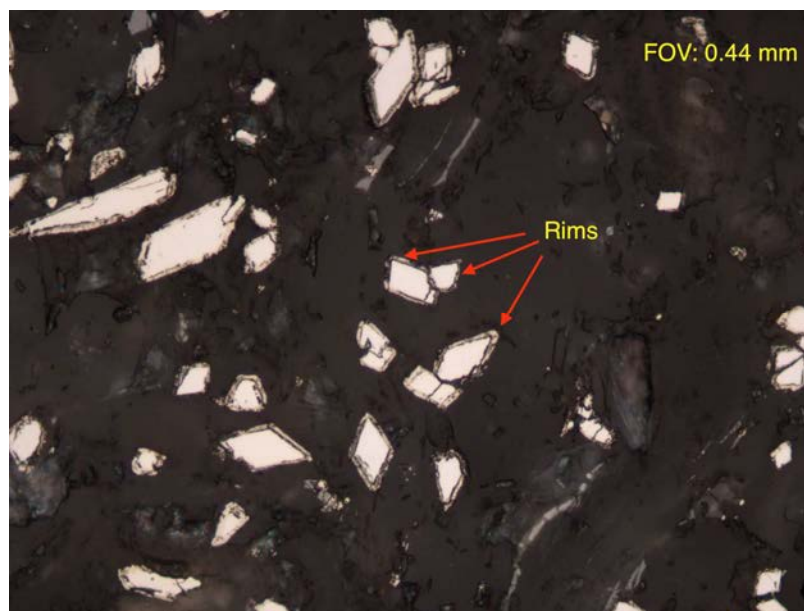


Figure 14: Photomicrograph taken from sample REB-199-1773. Annotation points out prominent arsenian pyrite rims around arsenopyrite (rhombohedral crystal shape) and marcasite. Rims are of the same morphology as those described by Wells and Mullens (1973), Hofstra and Cline (2000), and Cline et al. (2005). Transmitted reflected light, 500X FOV: 0.44mm.

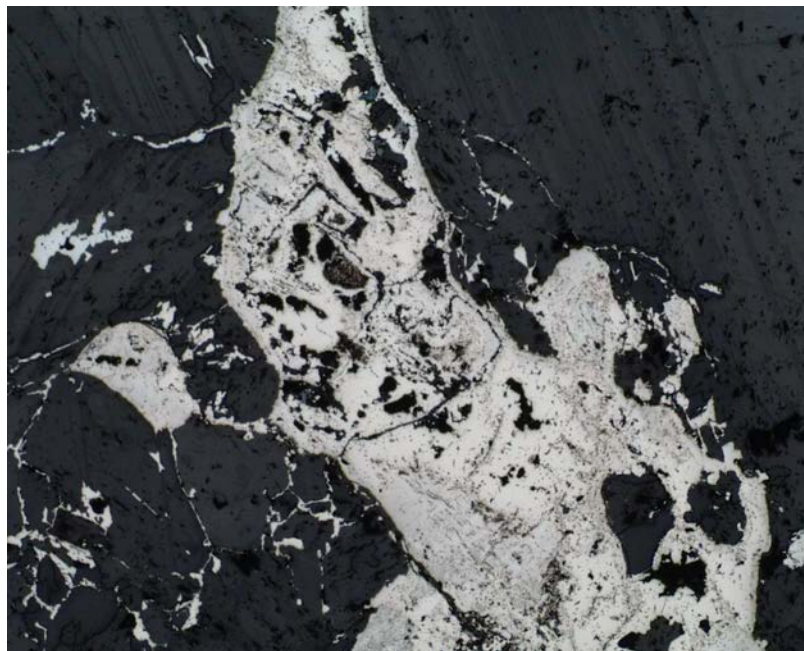


Figure 16: Reflected light photomicrograph of arsenic rich rims on pyrite-marcasite intergrowths from sample REB-148-1433. Photo was taken at 100X magnification and shows fracture filling of sulfide material in gangue material. FOV: 2.16 mm.



Figure 17: Two hand samples from core of pyrite morphology at the Mike deposit, associated with Carlin type mineralization and gold. Left: REB-199-1577 showing sooty disseminated sulfide in decarbonatized and lightly clay altered rock. Right: REB-186-1737 sulfide stringers parallel to bedding and small pyrite-carbonate veinlet parallel to bedding, possibly hydrothermal in origin.

Base metal associated sulfides and textures: Base metals at Mike, below the leached cap, consist of copper, zinc, and lead sulfides. These minerals are found locally, where higher grade Carlin-gold mineralization occurs. Where both base metal mineralization, especially copper minerals, and gold-rich arsenian rims on pyrite occur together, the base metals appear to be later in age. This is in contrast to the model established by Norby and Orobona (2002) and Bawden (2002) and sulfide paragenesis will be summarized and discussed within the discussion section.

Pyrrhotite is distinctly pink-yellow and was found in two intervals in close association with chalcopyrite and sphalerite, but is not a significant mineral. Pyrrhotite was only found in calc-silicate assemblages (Fig. 20).

Chalcopyrite is the dominant copper mineral in the hypogene zone at Mike. It is not the dominant base metal sulfide at Mike, and only locally identifiable macroscopically. It is commonly found within veinlets in association with other base metals and variable amounts of calcite and quartz. Fine-grained disseminations are also common, parallel to some bedding, but these grains are not macroscopically identifiable. Chalcopyrite replaces pyrrhotite where both are in association (Fig. 20). Chalcopyrite and bornite are also in close association and display replacement and veining of each other (Fig. 29). Both chalcopyrite and bornite are replaced by covellite and digenite, but their occurrence is minor in the hypogene zone.

Chalcocite locally occurs on chalcopyrite and bornite, but is erratically distributed throughout the hypogene zone. It occurs as rims and peripheral replacements on chalcopyrite and bornite grains (Figs. 18 and 29). These copper associated sulfides are anhedral, and commonly occur in veinlets with carbonate and quartz.

Sphalerite and galena are the most dominant base metal sulfides within the samples examined from the unoxidized portion of the Mike deposit. Sphalerite is found within veins and veinlets in association with pyrite and galena as well as carbonate and quartz (Figs. 20 - 25, 27, and 28). Sphalerite shows local fine disseminations of chalcopyrite, known as chalcopyrite disease, and fills in fractures and surrounds pyrite and chalcopyrite. Dissemination of pyrite in sphalerite is also common, and mainly restricted to high-iron sphalerite that is brown to red in color. Sphalerite also occurs as a light brown to yellow form, due to lower iron content. Low-iron sphalerite appears to be paragenetically earlier than higher iron sphalerite, though cross cutting relationships are only observed in one sample. Sphalerite is rarely individual grains, and is predominantly large patches of overgrowths and aggregates of crystals. Where sphalerite occurs in relation to arsenian rims on pyrite, it appears to be later in age (Figs. 19, 22 - 28). Framboidal "biogenetic" sphalerite identified within the leached cap and redox boundary by Bawden (2002) was not identified within the unoxidized hypogene occurrences of sphalerite found in this study.

Galena is more rare than sphalerite in the thin sections, but is commonly found in proximity to red-brown sphalerite where present (Figs. 22, 24, and 28). Where present, galena is in association with pyrite, arsenopyrite, chalcopyrite, and sphalerite. It occurs as anhedral growths on other sulfide minerals. Galena appears to be later than Carlin-type arsenian pyrite rims (Figs. 22, 24, and 28). Galena is also identified by Norby and Orobona (2002) as "argentiferous," and containing most of the silver at Mike. This is confirmed by ICP data that shows that lead and silver are commonly anomalous over the same regions. Silver is also shown to correlate with lead in the geochemical study of this

thesis (see geochemistry section). Galena is commonly replaced by bournonite, which displays a more mottled, speckled appearance in thin section, but is difficult to discern optically and was not identified macroscopically. Bournonite may also contain silver (T. Thompson, personal communication, 2014).

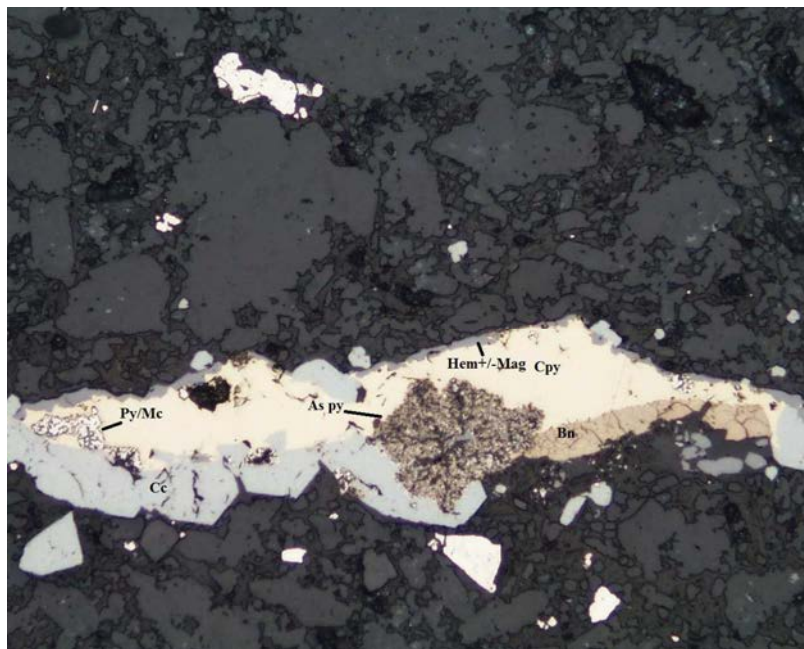


Figure 18: Reflected light photomicrograph from sample REB-148-1594. Annotation shows pyrite-marcasite intergrowth (Py/Mc), chalcopyrite (cpy), bornite (Bn), chalcocite (Cc), arsenian pyrite (As py), hematite and magnetite (hem±mag). 100X magnification; FOV: 2.16 mm.

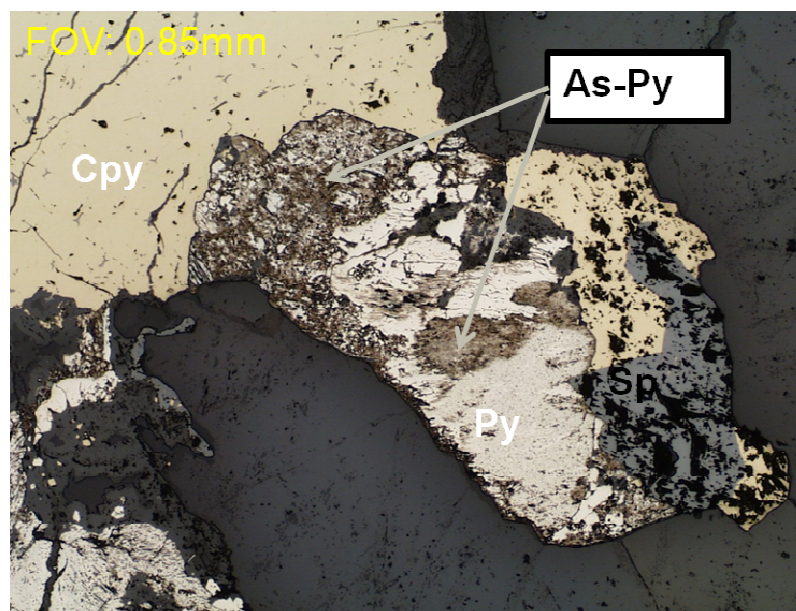


Figure 19: Photomicrograph of arsenian pyrite (fine grained and annotated by As-py) in relation to earlier pyrite (py). Later chalcopyrite (cpy) and sphalerite (sp) growing around pyrite grains. Photo taken at 100X; FOV: 0.85 mm.

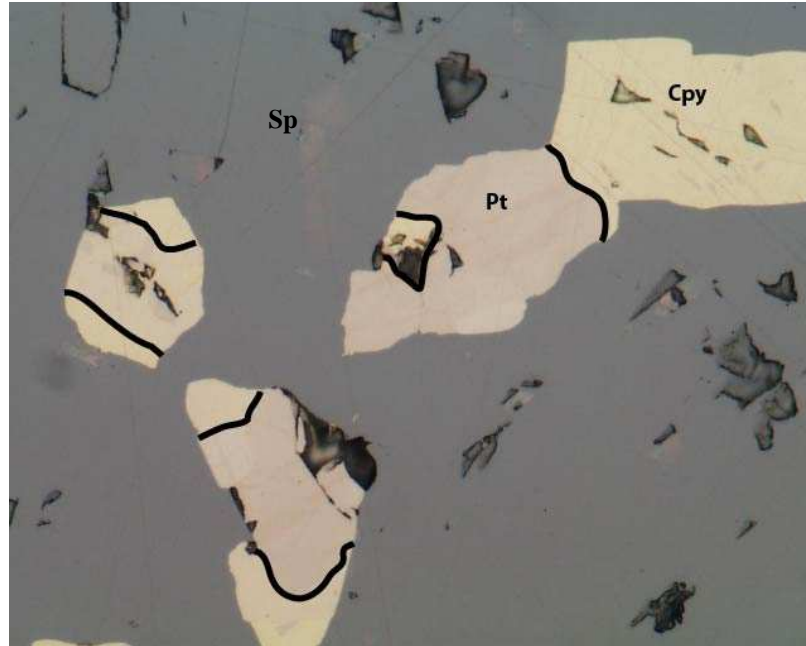


Figure 20: Reflected light photomicrograph of sample REB-153-1670 that shows pyrrhotite (Pt) and chalcopyrite (Cpy) hosted within a sphalerite matrix. Photo was taken at 200X magnification, FOV: 1.08 mm.

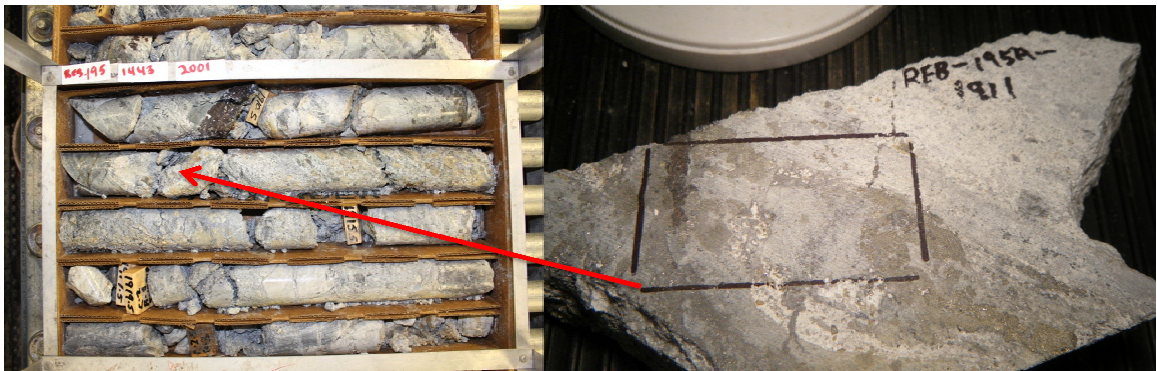


Figure 21: Core photo and macroscopic hand sample showing where sample for Figures 22 and 24 came from. Shows an example of morphology of base metal sulfide distribution within host rock as vein. Rock has undergone intermediate clay alteration.

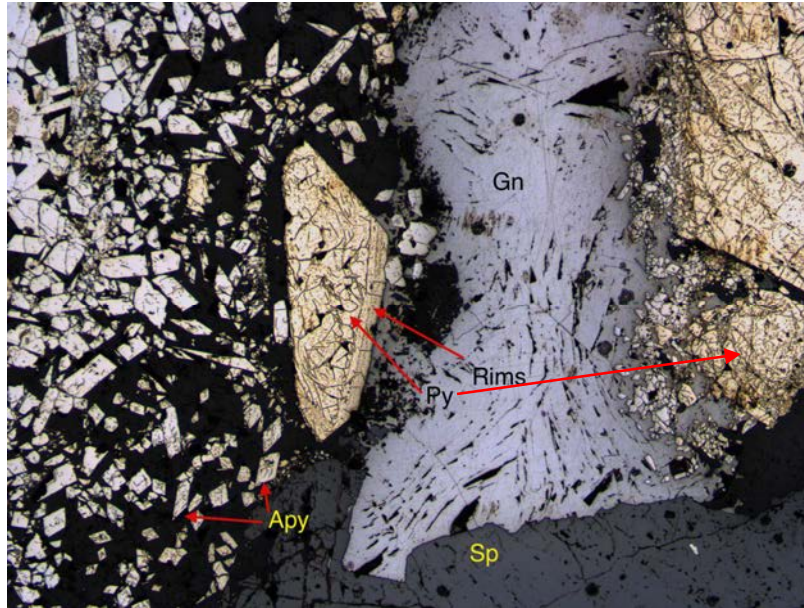


Figure 22: Photomicrograph of REB-195A-1911 that shows partial arsenian rims on fractured pyrite and base metal sulfides. Galena (gn) and sphalerite (sp) appear to be later than the rims on pyrite (py). Arsenopyrite also appears to be later (apy). FOV: 2.16 mm.

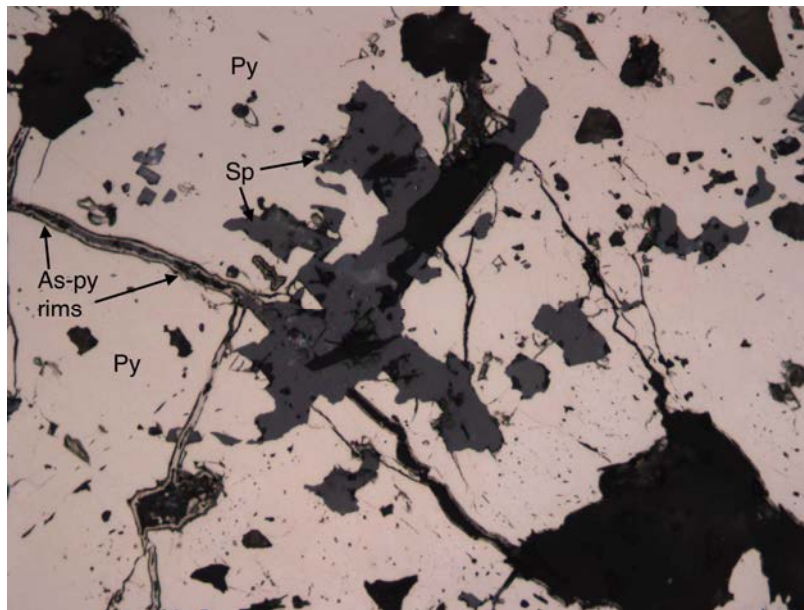


Figure 23: Pyrite (py) with arsenian pyrite rims (as-py) over printed by later sphalerite (sp). Photomicrograph is from sample REB-199-1773 and was taken at 500X, FOV: 0.44 mm.

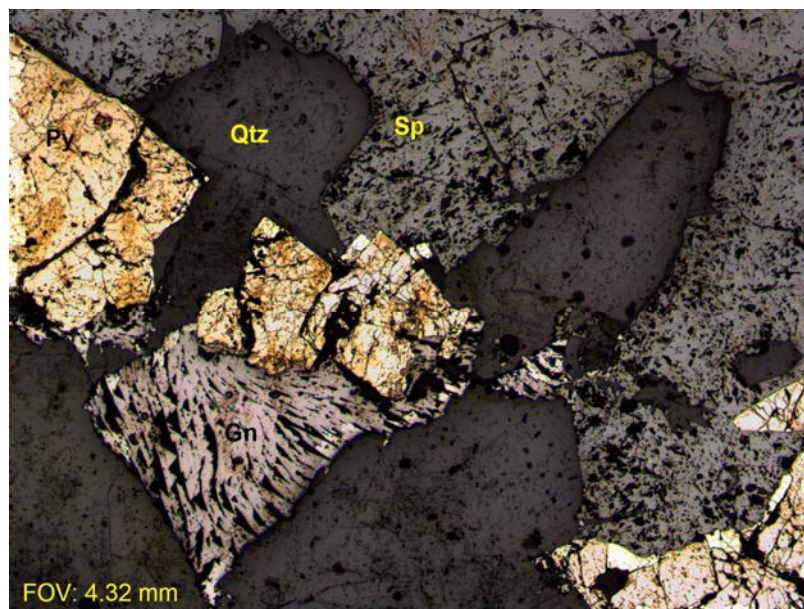


Figure 24: Photomicrograph of sample REB-195A-1911 that shows hydrothermal pyrite with Carlin-type arsenian rims overprinted by galena (gn) and sphalerite (sp). Quartz (qtz) is also found between base metal sulfides and pyrite. Reflected plane light taken at 50X, FOV: 4.32 mm.

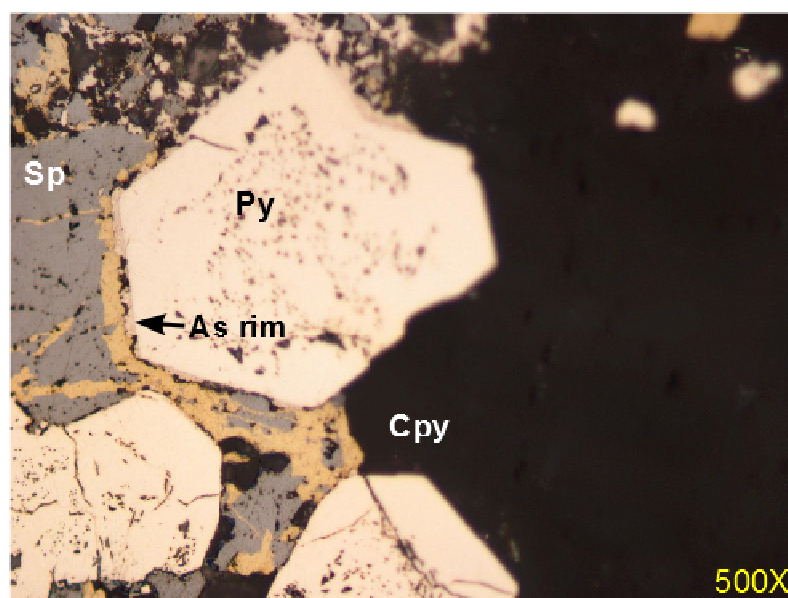


Figure 25: Photomicrograph from REB-153-1978 that shows pyrite core with a faint arsenian rim. Arsenian rim identified optically, and confirmed by SEM-EDS. Rim is overprinted by sphalerite (gray) and chalcopyrite (golden yellow). Chalcopyrite is veining sphalerite. Photo taken at 500X plane reflected light; FOV: 0.44 mm.

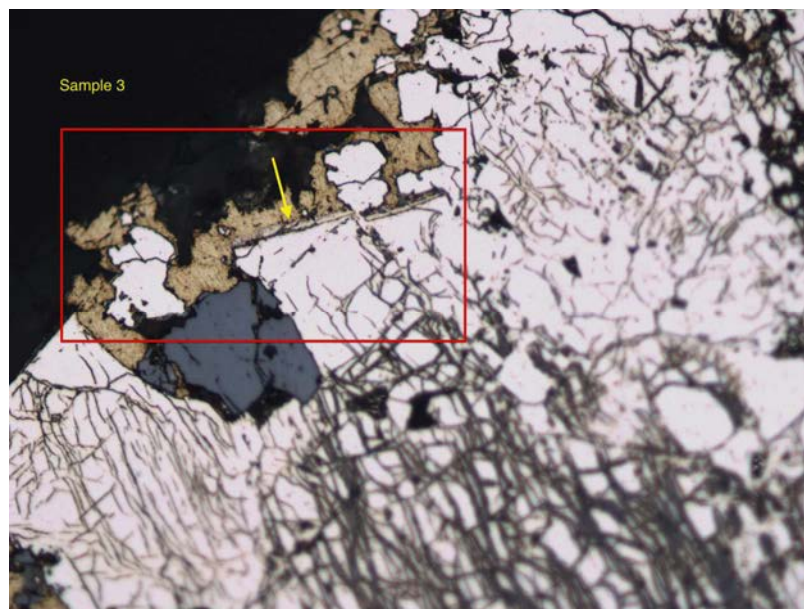


Figure 26: Photomicrograph from sample REB-199-1773 showing hydrothermal pyrite with sphalerite veining (gray stringers) and arsenian rims identified optically (yellow arrow). Chalcopyrite (gold colored mineral) overprints the rims on the pyrite. Photo taken at 500X; FOV: 0.44 mm. Sample selected for SEM-EDS analysis (red box and label).

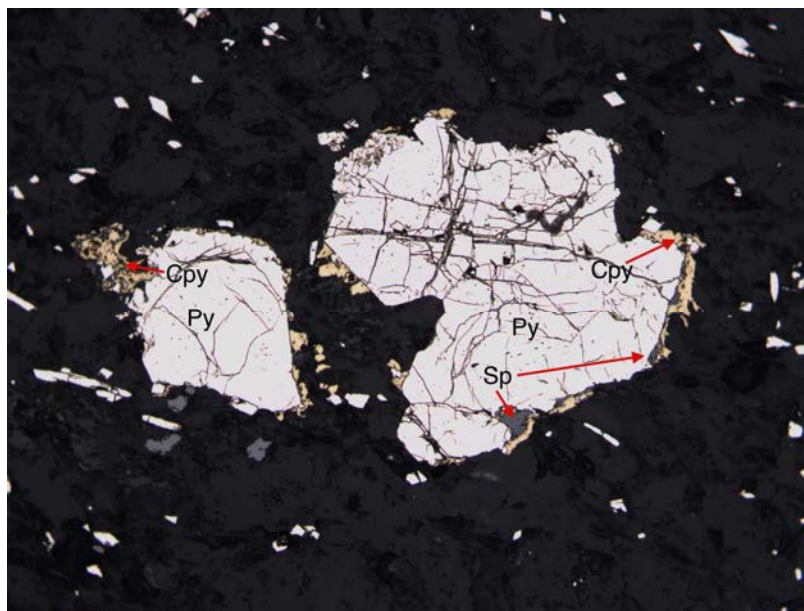


Figure 27: Photomicrograph from REB-199-1773 that shows chalcopyrite (Cpy, yellow) rimming and replacing pyrite (Py). Sphalerite (Sp) is also found on the edges of pyrite. 200X magnification; FOV: 1.08 mm.

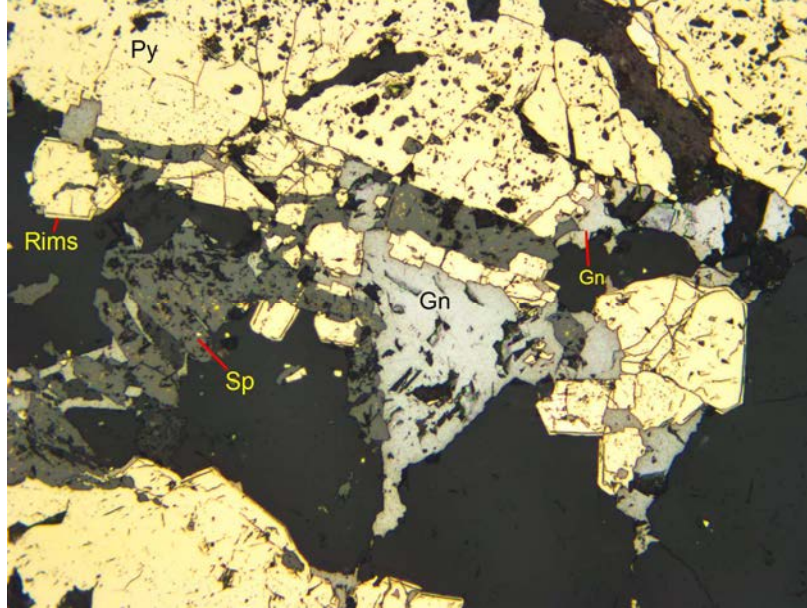


Figure 28: Photomicrograph of sample REB-199-1773 showing paragenetically later sphalerite (sp) and galena (gn) partially replacing arsenian rims on sieve-textured pyrite. Photo taken at 200X; FOV: 1.08 mm.

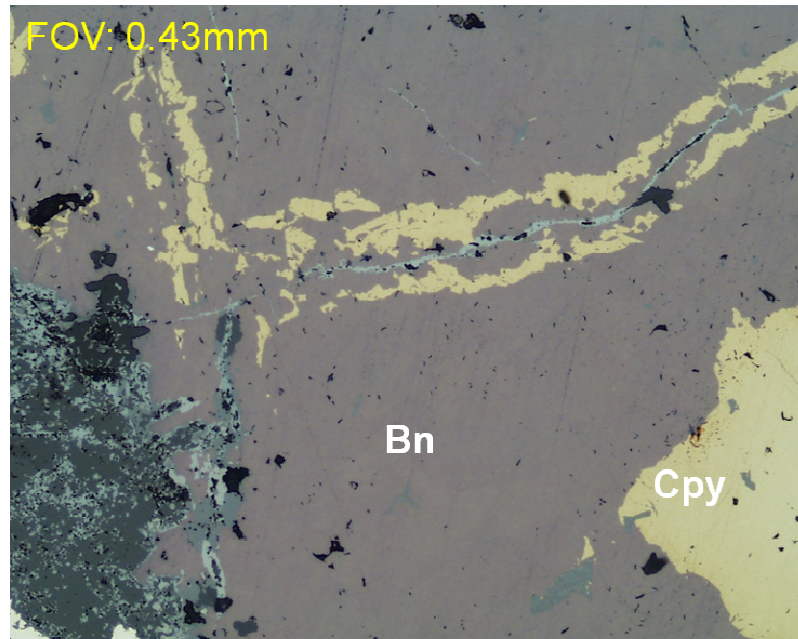


Figure 29: Photomicrograph of sample REB-153-1831 that shows bornite (Bn) veined and replaced by chalcopyrite (cpy) and later stringers of chalcocite (light blue-gray). Taken at 500X; FOV: 0.43mm.

SEM Analysis

Methods

After paragenetic relationships between base metal and Carlin-type gold mineralization were established petrographically, three polished thin sections that displayed the best textures of base metal sulfides occurring later than suspected arsenian rims on pyrite were selected. These samples were documented through photomicrographs, and outlined on the thin sections and submitted to The Mineral Lab in Golden, Colorado for SEM imaging and EDS analysis. This analysis was done to document trace element distributions within pyrite, arsenian rims, and base metals sulfides similar to the study done by Large et al. (2009).

SEM-EDS Results

Two locations within the sample REB-195A-1911 were examined, annotated with numbers and arrows in Figure 30. Zone 1 (labeled as 1) is an image of a pyrite core with a very minor, later hydrothermal rim and very fine grained, later arsenopyrite. The pyrite and arsenopyrite are surrounded by quartz, which is black in the grayscale image in zone 1. The iron distribution in zone 1 clearly outlines the iron sulfides against the quartz, which has very low concentrations of iron in comparison. The arsenic image of zone 1 shows higher concentrations of arsenic within the arsenopyrite as well as an increase in concentration along the edge of the larger pyrite grain, within the hydrothermal rim. This concentration is not as high as the arsenopyrite (larger patches of blue pixels), but is more so than the earlier, barren pyrite phase (Fig. 30).

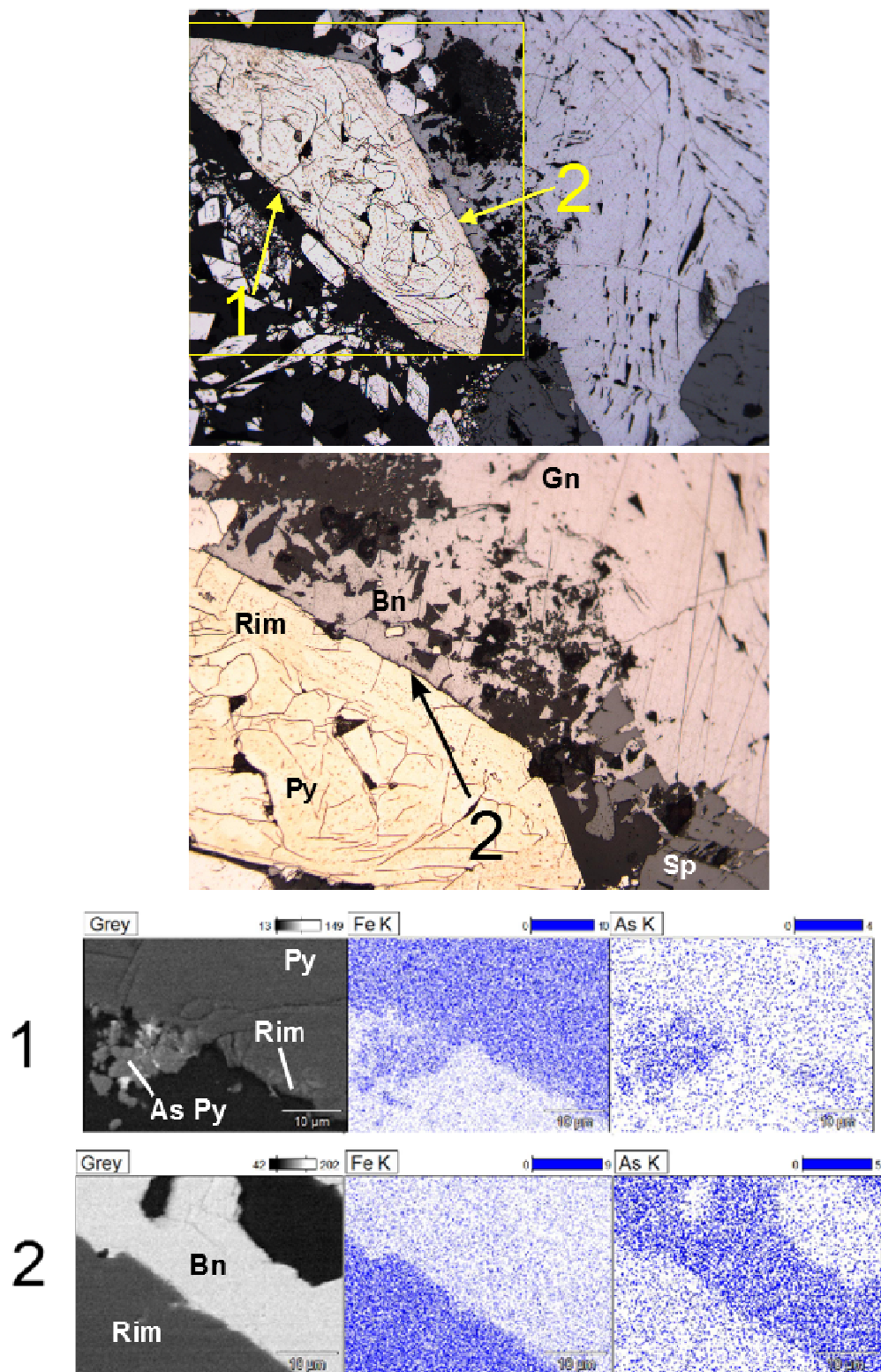


Figure 30: Annotated photomicrograph of pyrite with hydrothermal rim and overprinting base metal sulfides and sulfosalts (bournonite - Bn) from REB-195A-1911. Two zones were analyzed from this sample and are denoted by the labels for zones 1 and 2. The lower photomicrograph is an enhanced view of zone 2 at 400X magnification and is annotated for minerals. Qualitative diagrams of relative iron and arsenic abundance are inset next to the grayscale SEM image of the area. See Fig. 19 for more detailed description of the first photo.

Zone 2 shows an area where pyrite and a faint hydrothermal rim, are in contact with bournonite (Bn in Figure 30). In the grayscale image, the pyrite is in the lower left and darker gray, while the bournonite is the lighter gray in the middle to upper right. Iron clearly shows the boundary of the pyrite grain, while arsenic shows increases in abundance within galena as well as a smaller, noticeable increase along the margin of the pyrite, within the fine-grained hydrothermal rim (Fig. 30).

Sample REB-153-1978 was also submitted for analysis to examine trace element distributions within a similar hydrothermal pyrite rim juxtaposed against later chalcopyrite and sphalerite. More trace elements were reported in the analysis of this sample due to those elements being above detection limits. Within the grayscale image in Figure 31, the hydrothermal pyrite rim is easily visible on the larger, euhedral pyrite grain. The lighter area to the left in the image is chalcopyrite. Arsenic, antimony, copper, and zinc all show higher concentrations within the chalcopyrite. Arsenic also seems to increase toward the edge of the pyrite and hydrothermal pyrite rim, but this increase is difficult to discern against the easily visible higher abundance of arsenic in the chalcopyrite (Fig. 31).

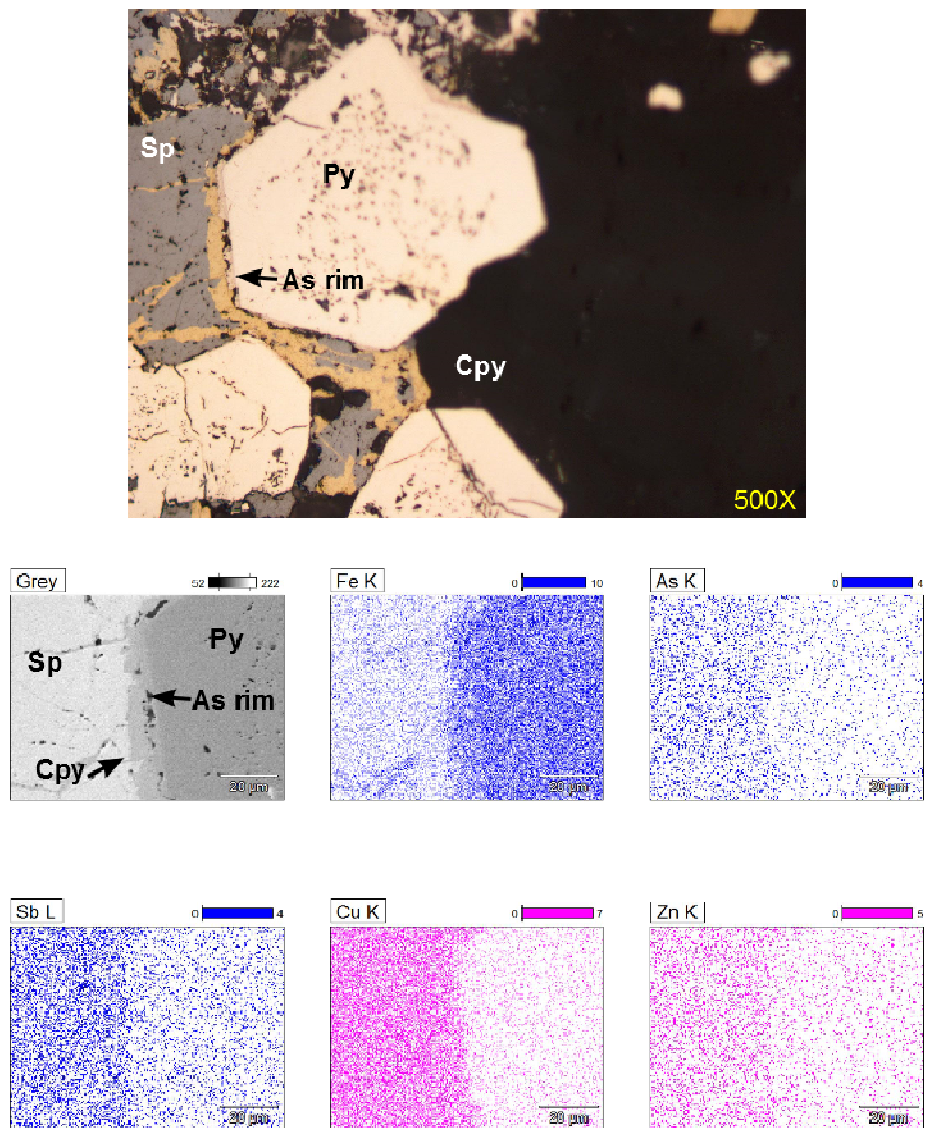


Figure 31: Photomicrograph and qualitative plots from SEM-EDS analysis of REB-153-1978 including grayscale image of the sample.

LA-ICPMS analysis was not available for this study, and so SEM-EDS was chosen instead. SEM-EDS results are more qualitative than quantitative, and follow-up analysis by LA-ICPMS or SIMS would help to more confidently show qualitative concentrations of gold and arsenic in hydrothermal rims on pyrite. Not all the samples chosen contained enough arsenic to be plotted, and so other elements that were above detection limits were reported by the lab instead, but these were predominantly sulfur and silicon.

Geochemistry

Geochemical Methodology

During the 2011 and 2012 drilling campaigns, drill cuttings and core samples were submitted by Newmont to American Assay Laboratories for 73-element suite ICP analysis, including ICP-MS and ICP-AES methods. Samples consisted of 0.5 g composited over 20 feet, partially digested in a two acid solution ($\text{HNO}_3 + \text{HCl}$) for two hours. Digested samples were analyzed with Agilent Vista ICP-AES and Bruker ICP-MS instruments (M. Mendoza, American Assay Labs, personal communication, 2014). Element abundances were reported in ppm and provided to the author in an Excel database by Newmont geologists. Data reported as below detection limits, listed as non-numeric values, were changed to reflect one-half of reported detection limits of each element in order to be useable in correlation coefficient calculations. Drill holes that encountered water in the bedrock, or an over abundance of Tertiary Carlin Formation were discarded from the data set due to the possibility of sample dilution by ground water and contamination by Tertiary Carlin Formation (R. Burgess, personal communication,

2013). The resulting "good" data, nearly all of which were derived from diamond drill core, were analyzed during the Fall 2013 and Spring 2014 semesters using Microsoft Excel, ioGas, and the Visual Data geostatistical software package. The phrase "leached cap," should be synonymous with the oxide boundary due to the elevation of the paleo-water table.

Data were transformed using ioGas' built-in dataset manipulation tools including log transformation of raw concentrations and calculation of Z-scores in order to limit the influence of outliers and the magnitude of concentrations (M. Coolbaugh, personal communication, 2014). Elements that showed very little variation and/or were consistently below detection limits were removed from the dataset as well.

Correlation matrices were calculated using ioGas' built-in statistical analysis using the Spearman method. Spearman correlation coefficients are considered more reliable for trace element geochemical analysis according to Patterson and Muntean (2011), due to the correlations being based on monotonical increases between elements as opposed to linear increasing relationships, such as in the Pearson method. Outliers do not manipulate data in a Spearman correlation to the same degree that they do in the Pearson method, yielding a more robust correlation coefficient between two variables (J. Carr, personal communication, 2014). Correlations were made at first using all "good" ICP data from the 2011 and 2012 drilling campaigns. Data were further refined to calculate matrices for smaller subsets of data to evaluate bulk geochemical patterns of the unoxidized portion of the Mike deposit, followed by eliminating all intervals of data except where gold was elevated above 0.005 troy ounce per ton, or 0.171 ppm, and a separate calculation of copper above 700 ppm. Multiple matrices were created in order to

compare and confirm correlations of elements and to determine deposit geochemical signatures.

The dataset for anomalous copper intervals is the smallest of the other data sets, and the correlations should be considered less robust than the other data sets. Anomalous copper is defined as concentrations above 700 ppm.

Factor analysis was recommended by my advisor, as well as Mike Ressel, Newmont North American Chief Geologist, as a way to analyze the geochemical database to help determine groupings of elements and their distribution in the bulk deposit (M. Ressel, personal communication, 2013). Correspondence analysis was chosen as a preferred method due to its mathematical derivation and robustness compared to other types of principal component analysis. This method examines correspondence, or relationships, between columns and rows in the data matrix and plots the variables in a two dimensional plot of a sample and its expected value (J. Carr, personal communication, 2014). When evaluating the resulting plots, elements that are grouped closely to one another show close associations, while two elements with large gaps between the two points, display a negative association. The same segregated datasets were chosen for factor analysis as in the correlation matrices calculations: bulk deposit, all data below the leached cap, gold anomalous intervals below the leached cap, and copper anomalous intervals below the leached cap. Plots were printed, then visually evaluated, and elemental associations were compared across multiple plots of different factors, and against correlations from the Spearman plots to look for in common correlations.

Following the completion of correspondence analysis, principal component analysis (PCA) was suggested by John Muntean and Mark Coolbaugh, as a second factor analysis method in order to compare against the results of correspondence analysis. PCA was performed using the same datasets that were used in the calculations of the Spearman matrices and correspondence analysis. Factors that represent the most covariance have been selected and are shown in Tables 1, 2, and 3.

Trace elements that showed consistent associations with copper and gold across correlation matrices, CA, and PCA were chosen to be modeled using the LeapFrog Geo 3D modeling software. This was done in the form of modeling the spatial extent of the strongest principal component factors that also were of high enough resolution to show meaningful plots. This was done in order to attempt to show spatial distribution between gold and copper within the hypogene system. PCA factors hypothesized to represent the gold and copper ore systems, as well as the negative skarn/calc-silicate factor were used in order to create interpolants. Due to varying drill hole spacing, the parameters of the algorithm used by LeapFrog Geo were adjusted in order to limit the distance from drill hole values considered in the calculation of interpolants. The algorithm was adjusted based on visual results of the calculation and in comparison to modeled gold and copper ore shells from Newmont, due to LeapFrog Geo lacking the capability of plotting data against a variogram. These figures are included at the end of this section.

Correlation Matrices

Spearman correlation coefficients (Figs. 32-35) were calculated and formatted in correlation matrices using ioGas for consecutively succinct data sets from bulk deposit to only those of elevated gold and copper in the unoxidized portion of the deposit. Correlations were calculated after the datasets had been leveled by removing trace elements consistently at or below detection limits, performing a log transformation, and calculating z-scores. Green cells are coefficients greater than 0.5 and are considered strong correlations. Yellow cells are coefficients between 0.35 and 0.49. Weak to moderate negative correlations, between -0.35 and -0.49, are also denoted by yellow highlighting. Red cells are negative coefficients that are less than -0.5 and are considered strong negative correlations.

Bulk deposit

Au: Within the Spearman correlation matrix for all recent drill data that were identified as "good," gold had several strong correlations. Gold most strongly correlates with silver (0.63), arsenic (0.50), bismuth (0.52), antimony (0.62), and tellurium (0.53) (Fig. 29). More moderate correlations with gold include copper (0.37), lead (0.44), tin (0.46), and tungsten (0.38).

Cu: Copper shows strong correlations with bismuth (0.63), tin (0.55), tellurium (0.52), and tungsten (0.58). Moderate correlations exist between copper and gold (0.37), silver (0.49), arsenic (0.38), lead (0.47), and antimony (0.4) (Fig. 32).

Below the leached cap

Au: Within the unoxidized portion of the Mike deposit, gold correlates with silver (0.65), arsenic (0.71), antimony (0.62), tellurium (0.55), and thallium (0.51). Lesser correlations exist between gold and bismuth (0.43) and sulfur (0.39) (Fig. 33).

Cu: Copper strongly correlates with bismuth (0.64), tin (0.56), and tellurium (0.59). Lesser correlations include copper and silver (0.36), lead (0.38), and tungsten (0.38) (Fig. 33).

Ag: Silver has many of the same strong correlations as gold, including with arsenic (0.6), bismuth (0.53), antimony (0.53), and tellurium (0.54). Silver also strongly correlates with iron (0.5), and lead (0.66). Lesser correlations exist between silver and zinc (0.42), copper (0.36), tin (0.49), and tellurium (0.42) (Fig. 33).

Anomalous gold intervals below the leached cap

Au: In intervals below the leached cap where gold values were above 0.171 ppm, gold showed no strong correlations; however, there is a moderate correlation with silver (0.44). Gold also negatively correlates with selenium (-0.40) (Fig. 34).

Cu: Copper correlates strongly with bismuth (0.57), tin (0.71), uranium (0.61), vanadium (0.5), and tungsten (0.59). Moderate copper correlations include molybdenum (0.37), and phosphorus (0.46) (Fig. 34).

Ag: Silver only strongly correlates with lead (0.53), and shows moderate correlations with phosphorus (0.37) and sulfur (0.35) (Fig. 34).

Zn: Zinc shows moderate correlations with arsenic (0.35), selenium (0.44), and tin (0.39) (Fig. 34).

Anomalous copper intervals below the leached cap

Au: Gold correlates with silver (0.59), arsenic (0.62), mercury (0.5), and antimony (0.68). Gold moderately correlates with lead (0.48) and sulfur (0.42) (Fig. 35).

Cu: Copper shows a strong correlation with tellurium (0.52) and weak to moderate correlations with bismuth (0.36), molybdenum (0.41), and thallium (0.37). There is also a negative moderate correlation with lead (-0.41) (Fig. 35).

Ag: Silver shows a strong correlation with gold (0.59), arsenic (0.66), phosphorus (0.60), lead (0.71), sulfur (0.62), antimony (0.82), tin (0.77) and zinc (0.53). Silver also shows a moderate correlation with bismuth (0.45) (Fig. 35).

Bulk Deposit Spearman Correlation of Trace Elements																
	Au	Ag	As	Bi	Cu	Fe	Hg	Pb	S	Sb	Se	Sn	Te	Tl	W	Zn
Au	1	0.63	0.5	0.52	0.37	0.25	0.28	0.44	0.079	0.62	0.015	0.46	0.53	-0.082	0.38	0.015
Ag	0.63	1	0.43	0.67	0.49	0.33	0.38	0.72	0.1	0.52	0.072	0.6	0.61	-0.025	0.43	0.18
As	0.5	0.43	1	0.35	0.38	0.7	0.38	0.33	0.41	0.37	0.35	0.46	0.28	0.41	0.27	0.49
Bi	0.52	0.67	0.35	1	0.63	0.26	0.19	0.63	-0.14	0.6	0.058	0.72	0.82	-0.18	0.61	0.087
Cu	0.37	0.49	0.38	0.63	1	0.23	0.28	0.47	-0.068	0.4	0.25	0.55	0.52	-0.12	0.58	0.13
Fe	0.25	0.33	0.7	0.26	0.23	1	0.33	0.29	0.42	0.26	0.36	0.5	0.14	0.47	0.25	0.66
Hg	0.28	0.38	0.38	0.19	0.28	0.33	1	0.21	0.45	0.19	0.43	0.25	0.12	0.28	0.17	0.29
Pb	0.44	0.72	0.33	0.63	0.47	0.29	0.21	1	-0.11	0.55	-0.01	0.59	0.54	-0.13	0.51	0.16
S	0.079	0.1	0.41	-0.14	-0.068	0.42	0.45	-0.11	1	-0.06	0.43	0.03	-0.18	0.56	-0.29	0.45
Sb	0.62	0.52	0.37	0.6	0.4	0.26	0.19	0.55	-0.06	1	-0.1	0.58	0.58	-0.3	0.49	-0.032
Se	0.015	0.072	0.35	0.058	0.25	0.36	0.43	-0.01	0.43	-0.1	1	0.13	-0.098	0.37	0.1	0.38
Sn	0.46	0.6	0.46	0.72	0.55	0.5	0.25	0.59	0.03	0.58	0.13	1	0.58	-0.016	0.56	0.26
Te	0.53	0.61	0.28	0.82	0.52	0.14	0.12	0.54	-0.18	0.58	-0.098	0.58	1	-0.22	0.54	-0.012
Tl	-0.082	-0.025	0.41	-0.18	-0.12	0.47	0.28	-0.13	0.56	-0.3	0.37	-0.016	-0.22	1	-0.27	0.63
W	0.38	0.43	0.27	0.61	0.58	0.25	0.17	0.51	-0.29	0.49	0.1	0.56	0.54	-0.27	1	0.034
Zn	0.015	0.18	0.49	0.087	0.13	0.66	0.29	0.16	0.45	-0.032	0.38	0.26	-0.012	0.63	0.034	1

Figure 32: Spearman correlation matrix of bulk deposit multi-element ICP data. Green is a correlation coefficient >0.5 , considered strong, and yellow is between 0.35 and 0.49 and considered moderate.

Below Leached Cap Spearman Correlation of Trace Elements															
	Au	Ag	As	Bi	Cu	Fe	Hg	Pb	S	Sb	Sn	Te	Tl	W	Zn
Au	1	0.65	0.71	0.43	0.27	0.25	0.33	0.34	0.39	0.62	0.31	0.55	0.51	0.091	0.15
Ag	0.65	1	0.6	0.53	0.36	0.5	0.29	0.66	0.48	0.53	0.49	0.54	0.42	0.06	0.42
As	0.71	0.6	1	0.38	0.17	0.46	0.45	0.33	0.68	0.65	0.39	0.44	0.73	0.067	0.31
Bi	0.43	0.53	0.38	1	0.64	0.32	0.14	0.45	0.23	0.43	0.62	0.7	0.26	0.13	0.38
Cu	0.27	0.36	0.17	0.64	1	-0.04	0.29	0.38	0.13	0.24	0.56	0.59	0.013	0.38	0.071
Fe	0.25	0.5	0.46	0.32	-0.04	1	-0.085	0.31	0.44	0.38	0.49	0.18	0.4	-0.26	0.75
Hg	0.33	0.29	0.45	0.14	0.29	-0.085	1	0.2	0.45	0.39	0.13	0.29	0.5	0.3	-0.028
Pb	0.34	0.66	0.33	0.45	0.38	0.31	0.2	1	0.31	0.32	0.44	0.37	0.18	0.027	0.39
S	0.39	0.48	0.68	0.23	0.13	0.44	0.45	0.31	1	0.47	0.34	0.26	0.64	0.013	0.28
Sb	0.62	0.53	0.65	0.43	0.24	0.38	0.39	0.32	0.47	1	0.42	0.4	0.65	0.02	0.31
Sn	0.31	0.49	0.39	0.62	0.56	0.49	0.13	0.44	0.34	0.42	1	0.48	0.31	0.14	0.46
Te	0.55	0.54	0.44	0.7	0.59	0.18	0.29	0.37	0.26	0.4	0.48	1	0.32	0.24	0.17
Tl	0.51	0.42	0.73	0.26	0.013	0.4	0.5	0.18	0.64	0.65	0.31	0.32	1	-0.1	0.3
W	0.091	0.06	0.067	0.13	0.38	-0.26	0.3	0.027	0.013	0.02	0.14	0.24	-0.1	1	-0.25
Zn	0.15	0.42	0.31	0.38	0.071	0.75	-0.028	0.39	0.28	0.31	0.46	0.17	0.3	-0.25	1

Figure 33: Spearman correlation for data below the leached cap. Green is a correlation coefficient > 0.5, Yellow is between 0.35 and 0.49.

Anomalous Intervals of Au Below Leached Cap Spearman Correlation of Trace Elements																	
	Au	Ag	As	Bi	Cu	Hg	Mo	P	Pb	S	Sb	Se	Sn	Te	Tl	W	Zn
Au	1	0.44	0.079	-0.24	-0.24	0.078	-0.052	-0.21	-0.051	0.1	0.16	-0.4	-0.27	0.046	0.22	-0.19	-0.34
Ag	0.44	1	0.19	0.04	0.15	0.26	0.13	0.37	0.53	0.35	0.31	-0.13	0.16	0.14	0.23	0.26	-0.095
As	0.079	0.19	1	0.24	0.049	0.44	-0.21	0.1	0.13	0.5	0.41	-0.061	0.23	0.31	0.54	0.044	0.35
Bi	-0.24	0.04	0.24	1	0.57	0.065	0.21	0.38	0.31	0.016	0.26	0.27	0.54	0.61	0.033	0.52	0.34
Cu	-0.24	0.15	0.049	0.57	1	0.12	0.37	0.46	0.21	-0.092	0.18	0.27	0.71	0.3	-0.22	0.59	0.093
Hg	0.078	0.26	0.44	0.065	0.12	1	0.34	0.23	0.016	0.42	0.7	-0.12	0.11	0.17	0.72	0.3	-0.32
Mo	-0.052	0.13	-0.21	0.21	0.37	0.34	1	0.2	0.022	-0.1	0.24	0.043	0.19	0.28	0.014	0.34	-0.28
P	-0.21	0.37	0.1	0.38	0.46	0.23	0.2	1	0.38	0.14	0.28	0.2	0.53	0.31	0.045	0.44	0.03
Pb	-0.051	0.53	0.13	0.31	0.21	0.016	0.022	0.38	1	0.11	0.18	-0.089	0.25	0.19	-0.02	0.21	0.19
S	0.1	0.35	0.5	0.016	-0.092	0.42	-0.1	0.14	0.11	1	0.34	0.045	0.18	0.07	0.54	-0.033	0.26
Sb	0.16	0.31	0.41	0.26	0.18	0.7	0.24	0.28	0.18	0.34	1	-0.18	0.31	0.25	0.55	0.31	-0.096
Se	-0.4	-0.13	-0.061	0.27	0.27	-0.12	0.043	0.2	-0.089	0.045	-0.18	1	0.34	-0.048	-0.21	0.24	0.44
Sn	-0.27	0.16	0.23	0.54	0.71	0.11	0.19	0.53	0.25	0.18	0.31	0.34	1	0.3	-0.017	0.47	0.39
Te	0.046	0.14	0.31	0.61	0.3	0.17	0.28	0.31	0.19	0.07	0.25	-0.048	0.3	1	0.16	0.33	0.13
Tl	0.22	0.23	0.54	0.033	-0.22	0.72	0.014	0.045	-0.02	0.54	0.55	-0.21	-0.017	0.16	1	-0.035	-0.075
W	-0.19	0.26	0.044	0.52	0.59	0.3	0.34	0.44	0.21	-0.033	0.31	0.24	0.47	0.33	-0.035	1	-0.011
Zn	-0.34	-0.095	0.35	0.34	0.093	-0.32	-0.28	0.03	0.19	0.26	-0.096	0.44	0.39	0.13	-0.075	-0.011	1

Figure 34: Spearman correlation of ICP data from gold anomalous intervals below the leached cap. Green is a correlation coefficient > 0.5, Yellow is between 0.35 and 0.49, and between -0.35 and -0.49.

Anomalous Intervals of Cu Below Leached Cap Spearman Correlation of Trace Elements																		
	Au	Ag	As	Bi	Cu	Hg	Mo	P	Pb	S	Sb	Se	Sn	Te	Tl	W	Zn	
Au	1	0.59	0.62	-0.056	-0.29	0.5	-0.34	0.22	0.48	0.42	0.68	-0.073	0.32	-0.22	-0.082	0.3	0.089	
Ag	0.59	1	0.66	0.45	0.038	-0.0019	-0.069	0.6	0.71	0.62	0.82	-0.34	0.77	0.18	-0.005	0.21	0.53	
As	0.62	0.66	1	-0.027	-0.076	0.33	-0.006	0.65	0.31	0.87	0.46	-0.12	0.44	-0.23	0.11	0.57	-0.016	
Bi	-0.056	0.45	-0.027	1	0.36	-0.57	0.32	0.12	0.16	0.13	0.25	-0.52	0.58	0.78	0.22	-0.33	0.42	
Cu	-0.29	0.038	-0.076	0.36	1	-0.12	0.41	-0.1	-0.41	0.13	0.069	-0.32	0.21	0.52	0.37	-0.16	-0.24	
Hg	0.5	-0.0019	0.33	-0.57	-0.12	1	-0.48	-0.13	-0.1	0.051	0.23	0.13	-0.25	-0.45	0.19	0.013	-0.49	
Mo	-0.34	-0.069	-0.006	0.32	0.41	-0.48	1	-0.035	-0.4	0.32	-0.35	-0.26	0.082	0.57	0.37	-0.04	-0.15	
P	0.22	0.6	0.65	0.12	-0.1	-0.13	-0.035	1	0.49	0.58	0.22	0.19	0.38	-0.27	-0.35	0.59	0.29	
Pb	0.48	0.71	0.31	0.16	-0.41	-0.1	-0.4	0.49	1	0.18	0.68	0.035	0.61	-0.21	-0.34	0.28	0.83	
S	0.42	0.62	0.87	0.13	0.13	0.051	0.32	0.58	0.18	1	0.31	-0.15	0.44	0.02	0.23	0.55	0.042	
Sb	0.68	0.82	0.46	0.25	0.069	0.23	-0.35	0.22	0.68	0.31	1	-0.42	0.72	0.097	-0.022	0.05	0.45	
Se	-0.073	-0.34	-0.12	-0.52	-0.32	0.13	-0.26	0.19	0.035	-0.15	-0.42	1	-0.59	-0.69	-0.4	0.46	-0.16	
Sn	0.32	0.77	0.44	0.58	0.21	-0.25	0.082	0.38	0.61	0.44	0.72	-0.59	1	0.33	0.012	0.13	0.58	
Te	-0.22	0.18	-0.23	0.78	0.52	-0.45	0.57	-0.27	-0.21	0.02	0.097	-0.69	0.33	1	0.48	-0.66	0.17	
Tl	-0.082	-0.005	0.11	0.22	0.37	0.19	0.37	-0.35	-0.34	0.23	-0.022	-0.4	0.012	0.48	1	-0.43	-0.11	
W	0.3	0.21	0.57	-0.33	-0.16	0.013	-0.04	0.59	0.28	0.55	0.05	0.46	0.13	-0.66	-0.43	1	-0.056	
Zn	0.089	0.53	-0.016	0.42	-0.24	-0.49	-0.15	0.29	0.83	0.042	0.45	-0.16	0.58	0.17	-0.11	-0.056	1	

Figure 35: Spearman correlation for ICP data from copper intervals >700ppm below the leached cap. Green is >0.5, yellow is between 0.35 and 0.49 and between -0.35 and -0.49, and red is <-0.5.

Correspondence Analysis plots

Correspondence analysis plots are preliminary and should be evaluated as such. Analysis is ongoing to further identify elemental groupings and correlations. Circles drawn on the plots identify elements with possible groupings, but do not identify the only possible groupings. Annotated factor plots are located at the end of this section.

Below leached cap: Factor 1 of the correspondence analysis for data below the leach cap accounts for 62.9% of the variance of the data. Factor 2 accounts for 13.3% of the variance and factor 3 accounts for 6.1%.

Factors 1 and 2 show copper and tellurium in a moderately close grouping (Fig. 36). Silver does not show a close association with other base metal associated elements, but is in close proximity to niobium. Mercury, lithium, arsenic, and bismuth all group together, along with the more minor elements, based on abundance, of tantalum, germanium, and erbium. Gold, thallium, sulfur, rhenium, antimony, cobalt, and aluminum also show a close grouping (Fig. 36).

In the plot of factor 1 and factor 3, (Fig. 37), copper, antimony, thallium, and sulfur show a close association. Arsenic, mercury, bismuth, germanium, and lithium group closely. Zinc shows an association with fluorine. Gold also shows an association with magnesium. Of note is silver and lead show no close association with other elements, and a large space between each other.

In the plot of factor 2 and factor 3 (Fig. 38), antimony, tin, sulfur, rhenium, and thallium show a close association. Arsenic, bismuth, lithium, mercury and germanium

comprise another group. Of note is gold and copper, neither of which show any close groupings. Silver shows an association with rubidium.

Anomalous gold intervals below the oxide zone: Factors 1 through 4 were used and account for the following percentages of variance in this data set: Factor 1 - 64.4%, factor 2 - 14.0%, factor 3 - 5.8%, factor 4 -4.4%.

In the factor 1 and factor 2 plot (Fig. 39), arsenic and bismuth show a close association, along with yttrium and dysprosium, both of which are very low in concentration. Tin, sulfur, antimony, thallium, tungsten, phosphorus, and rhenium show a moderate grouping. Silver, copper, and zinc show no close associations, with a possible moderate to weak association between silver and copper. Tellurium is also isolated, but near beryllium and lanthanum.

The plot of factors 2 and 3 (Fig. 40) again shows lead and tungsten as far removed from all other elements, including each other. Gold is removed from most other elements, with cesium being the closest. Thallium, arsenic, sulfur, and antimony have a loose grouping. Zinc and vanadium are closely associated. Copper, silver and mercury are loosely grouped along with a host of other elements.

The factors 1 and 3 plot (Fig. 41) shows tungsten, lead, and zinc as having no close associations with any elements. Gold is in close association with antimony, tellurium, cesium, and tin. Copper is in close association with sulfur, selenium, aluminum, silver, and tantalum. Thallium and arsenic are removed from their expected Carlin or base-metal associations.

The plot of factors 1 and 4 (Fig. 42) shows a wide groupings of gold, tin, copper, selenium, and sulfur. Another cluttered association includes mercury, bismuth, antimony, and arsenic along with other lower concentrated elements. Zinc is notably removed from other elements as well as silver. Lead is very far removed from all other elements.

The factors 2 and 4 plot (Fig. 43) also shows lead as removed from all other elements. Gold shows no close relationship with other elements. Antimony, sulfur, and thallium show close associations while arsenic, mercury, zinc, and bismuth comprise another group. Copper is closest with magnesium while both silver and tin don't associate with any other highly concentrated elements.

Anomalous copper values below the oxide zone: Factor percentage of variance is as follows: Factor 1 - 59.2%, factor 2 - 19.2%, factor 3 - 10.7%, factor 4 - 3.96%.

Factors 1 and 2 (Fig. 44) show a loose grouping of copper, magnesium, and zinc along with terbium, which has low concentrations. Antimony and gold show a very close association. Silver, tungsten, and lead show no associations with other elements. Arsenic and mercury are closely associated and are near germanium and thorium.

Factors 2 and 3 (Fig. 45) show copper, gold, lead, and silver with no close associations. Gold is closest to sulfur, tin, bismuth, and selenium, however. Arsenic, thorium and germanium are close in association, but thorium is of low concentration. Thallium is noticeably removed from other elements.

Factors 1 and 3 (Fig. 46) show gold associated with bismuth, mercury, selenium, and weakly with lead and zinc. Copper is distinctly separated from most other elements.

Carlin-related trace elements of arsenic and antimony are in association, along with tungsten and germanium. Silver and tellurium show a close grouping.

The plot for factors 1 and 4 (Fig. 47) show a very close association of gold and copper as well as with bismuth, silver, and tellurium. Arsenic, tin and mercury plot further from the main group that includes gold. Zinc, lead, and tungsten all plot away from the gold group.

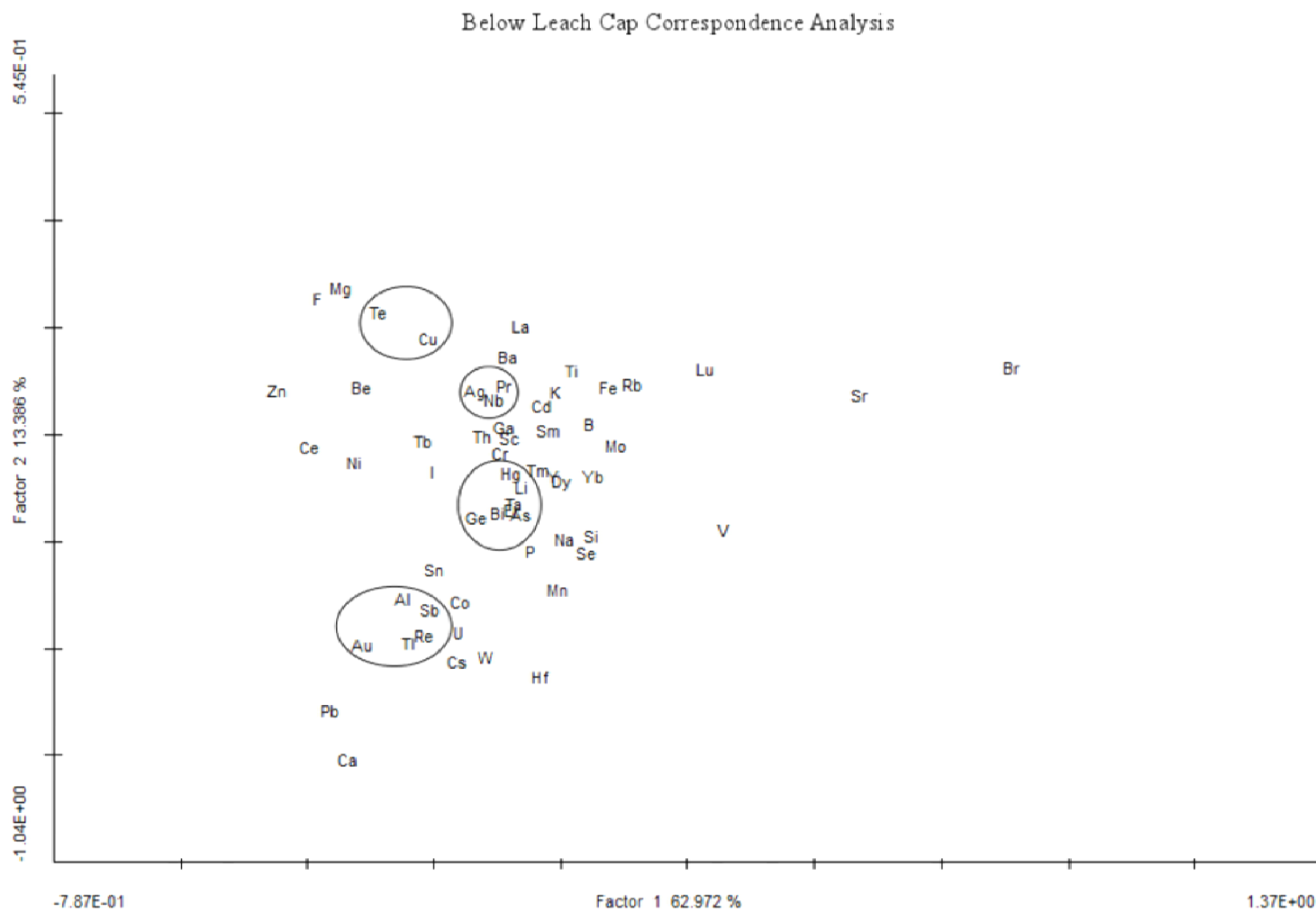


Figure 36: Correspondence analysis plot of factors 1 and 2 for all intervals below the oxide zone. Elements circled show close associations.

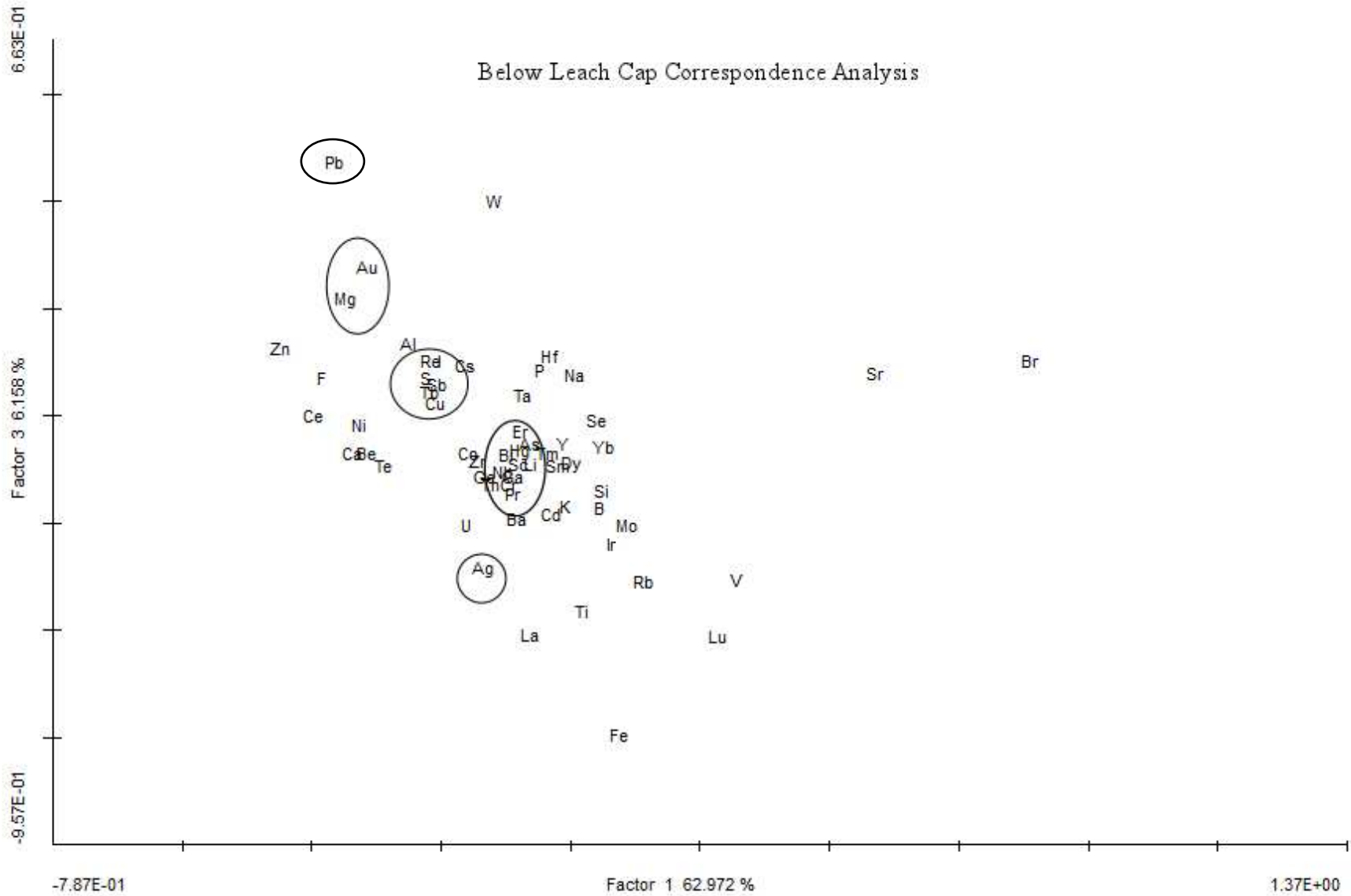


Figure 37: Correspondence analysis factor plot for factors 1 and 3 from data below the leached cap. Circled elements show associations of Carlin and base metal associated elements.

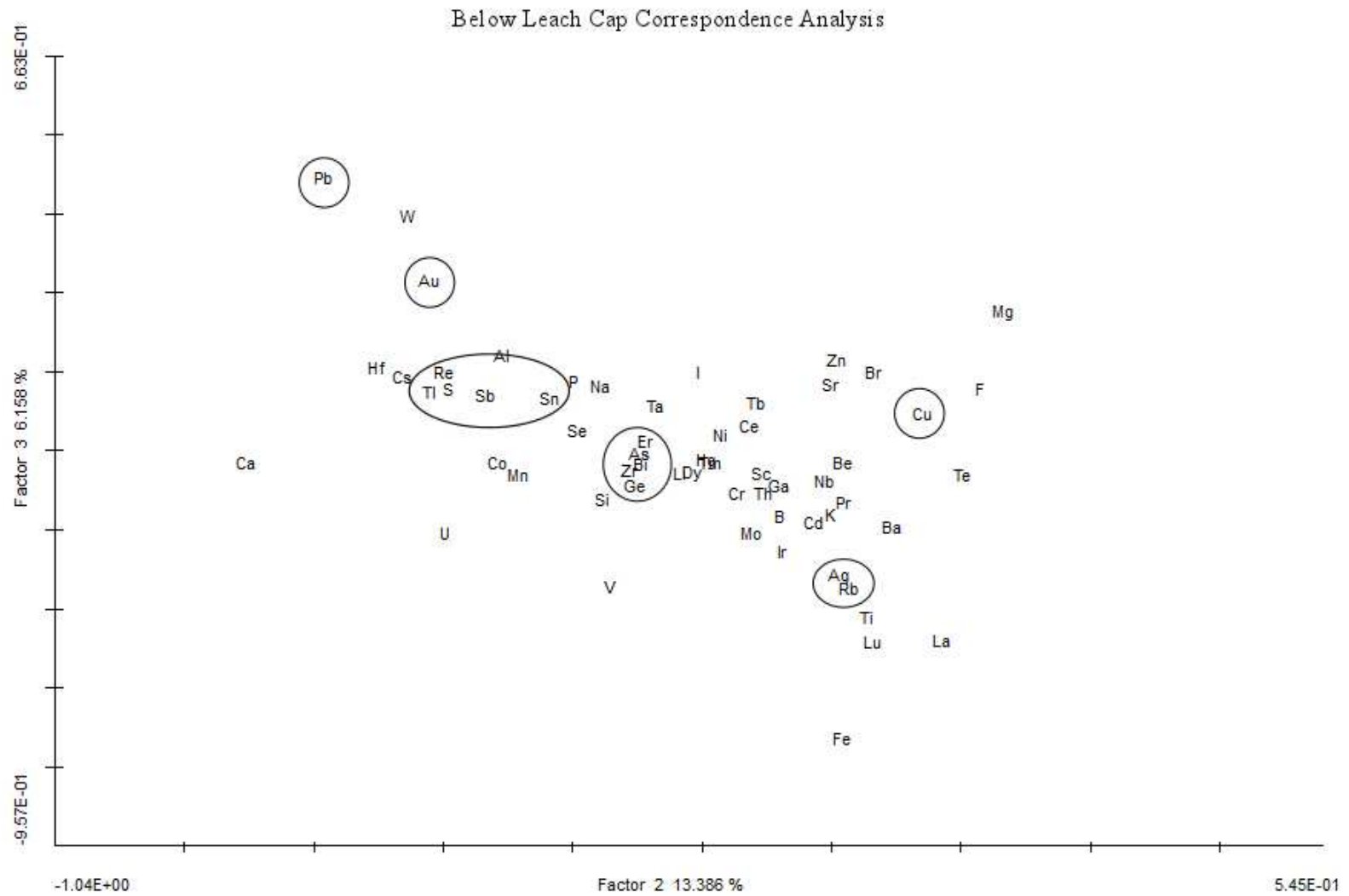


Figure 38: Correspondence analysis of below leach cap factor plot for factors 2 and 3 with elements of interest circled.

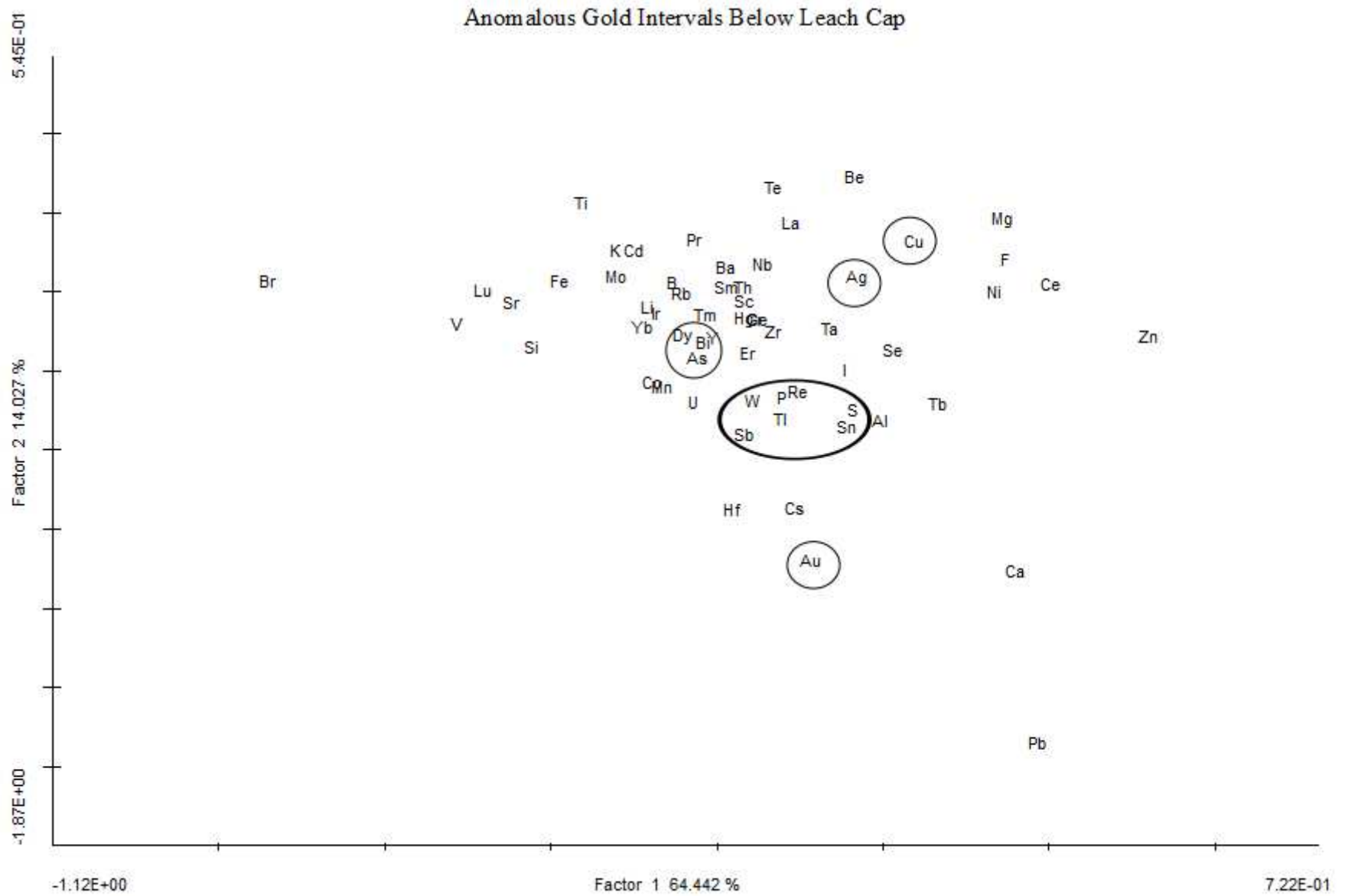


Figure 39: Correspondence analysis plot of factors 1 and 2 of elevated gold values below the oxide zone. Circled elements of of interest.

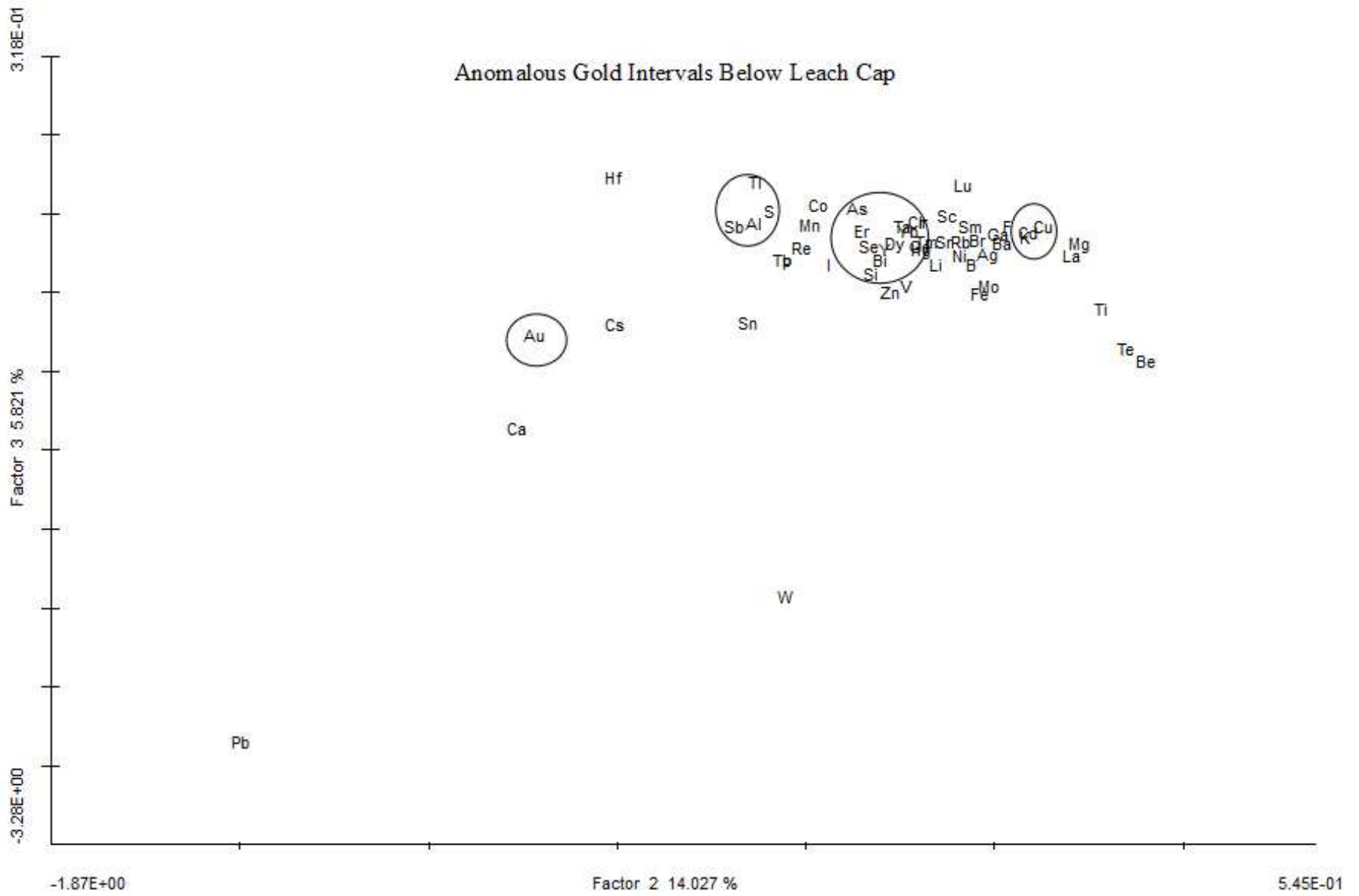


Figure 40: Correspondence plot of factors 2 and 3 for anomalous gold values below the oxide zone.

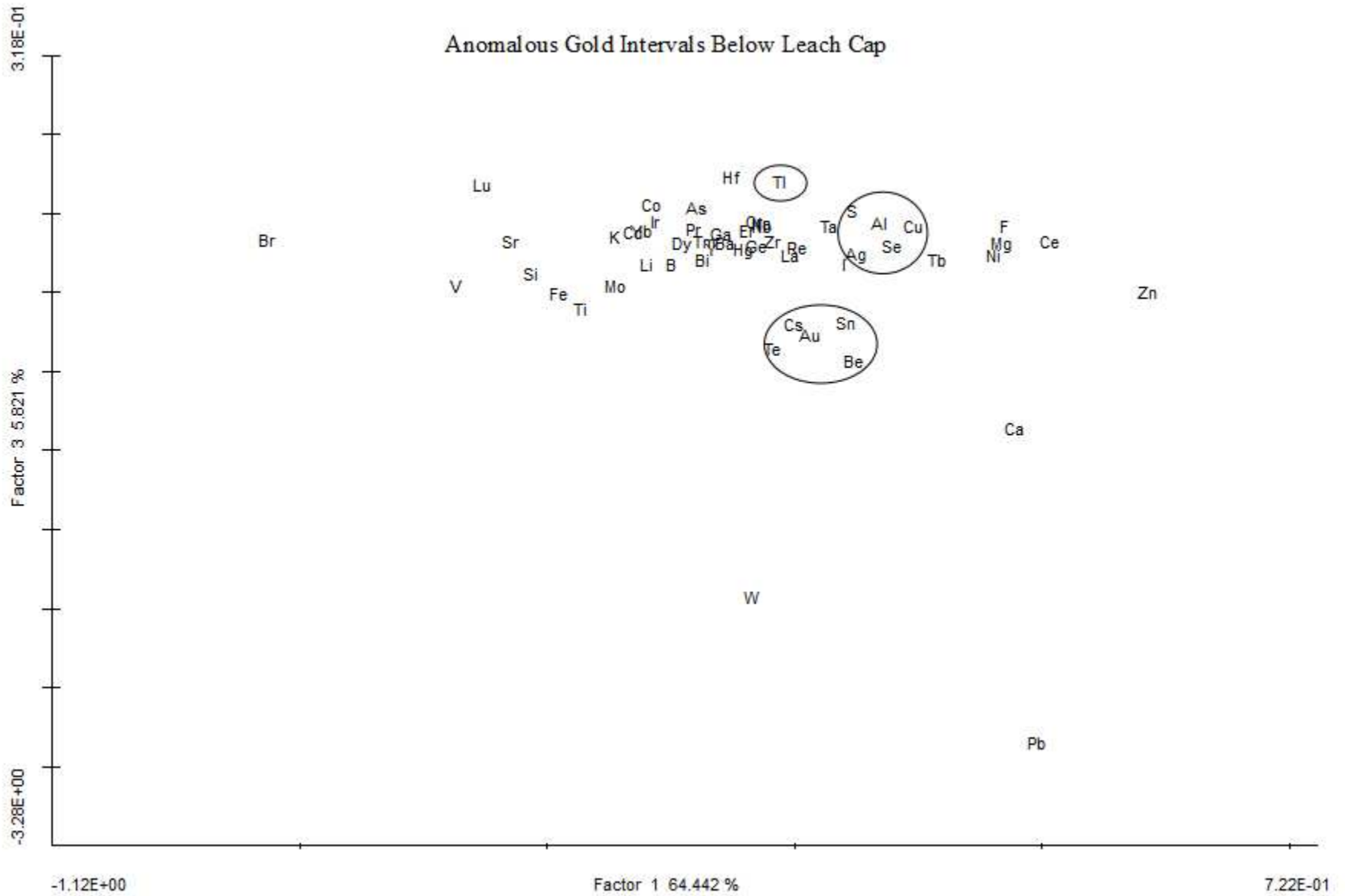


Figure 41: Correspondence analysis plot of factors 1 and 3 for anomalous gold values below the oxide zone. Close groupings of elements of interest are circled.

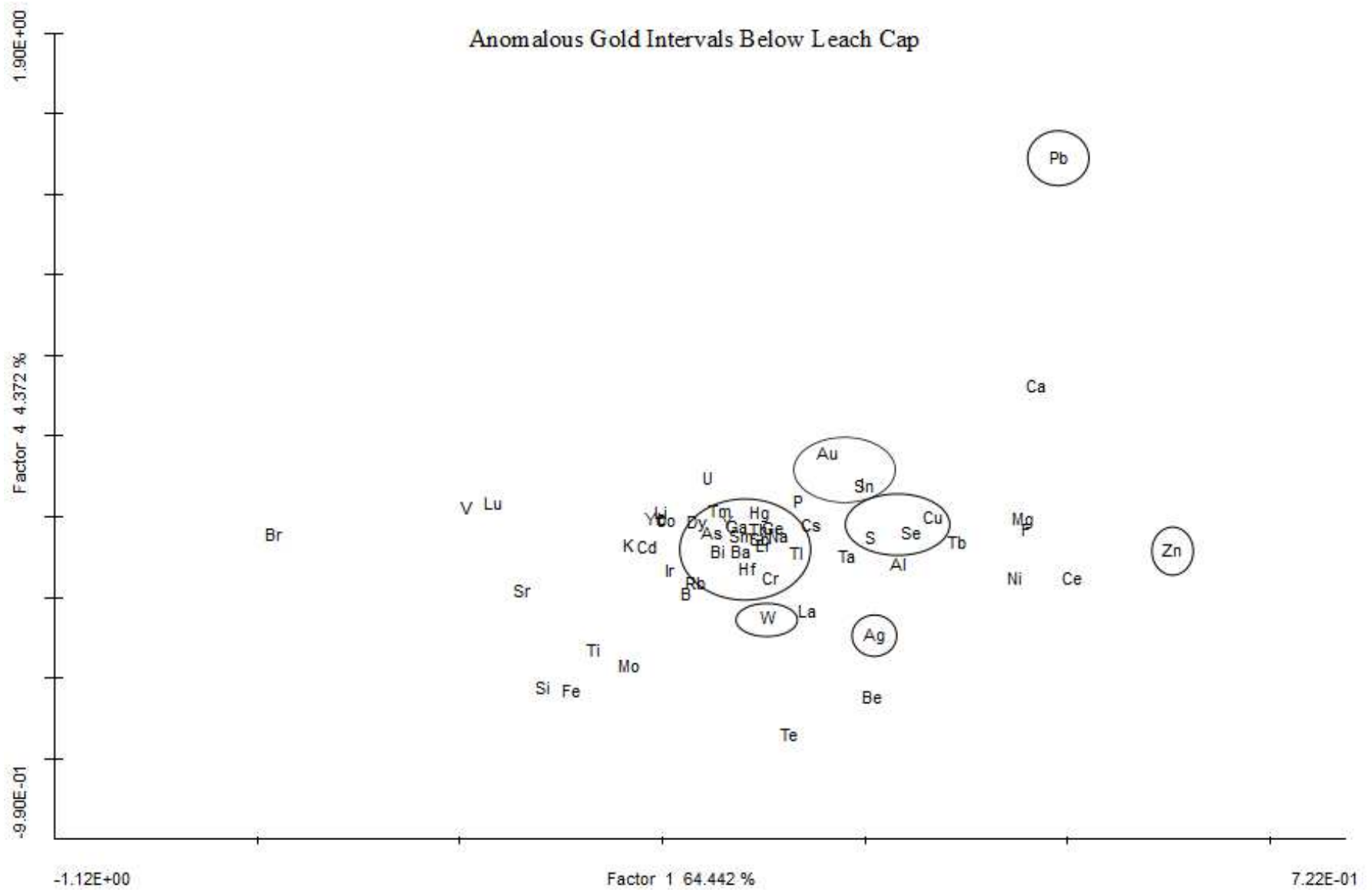


Figure 42: Correspondence analysis plot of factors 1 and 4 for intervals below the oxide zone with anomalous gold. Elements of note are circled to show associations or lack thereof.

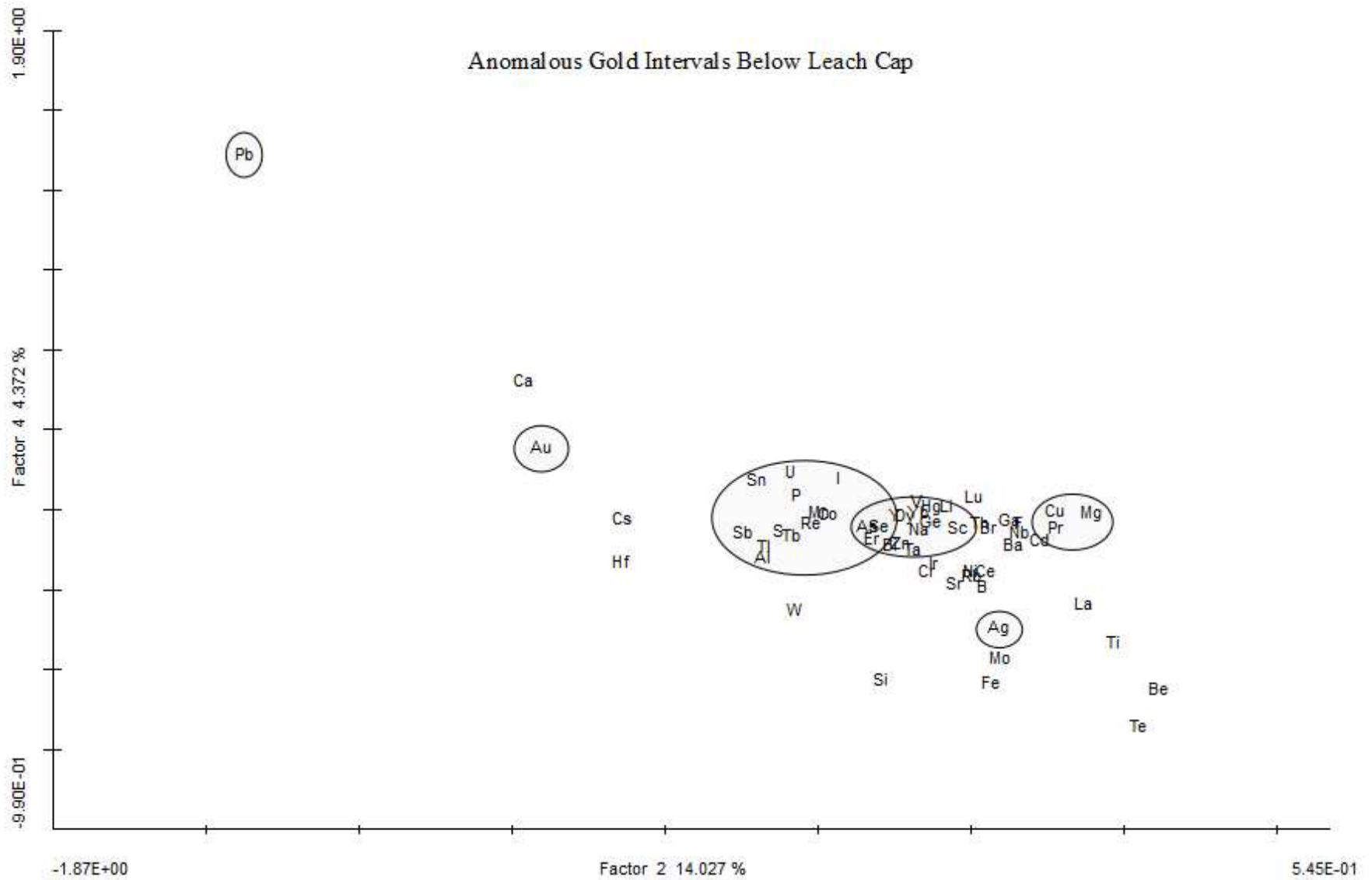


Figure 43: Correspondence analysis plot for anomalous gold intervals below the leached cap. Plot of factors 2 and 4 with elements of interest circled.

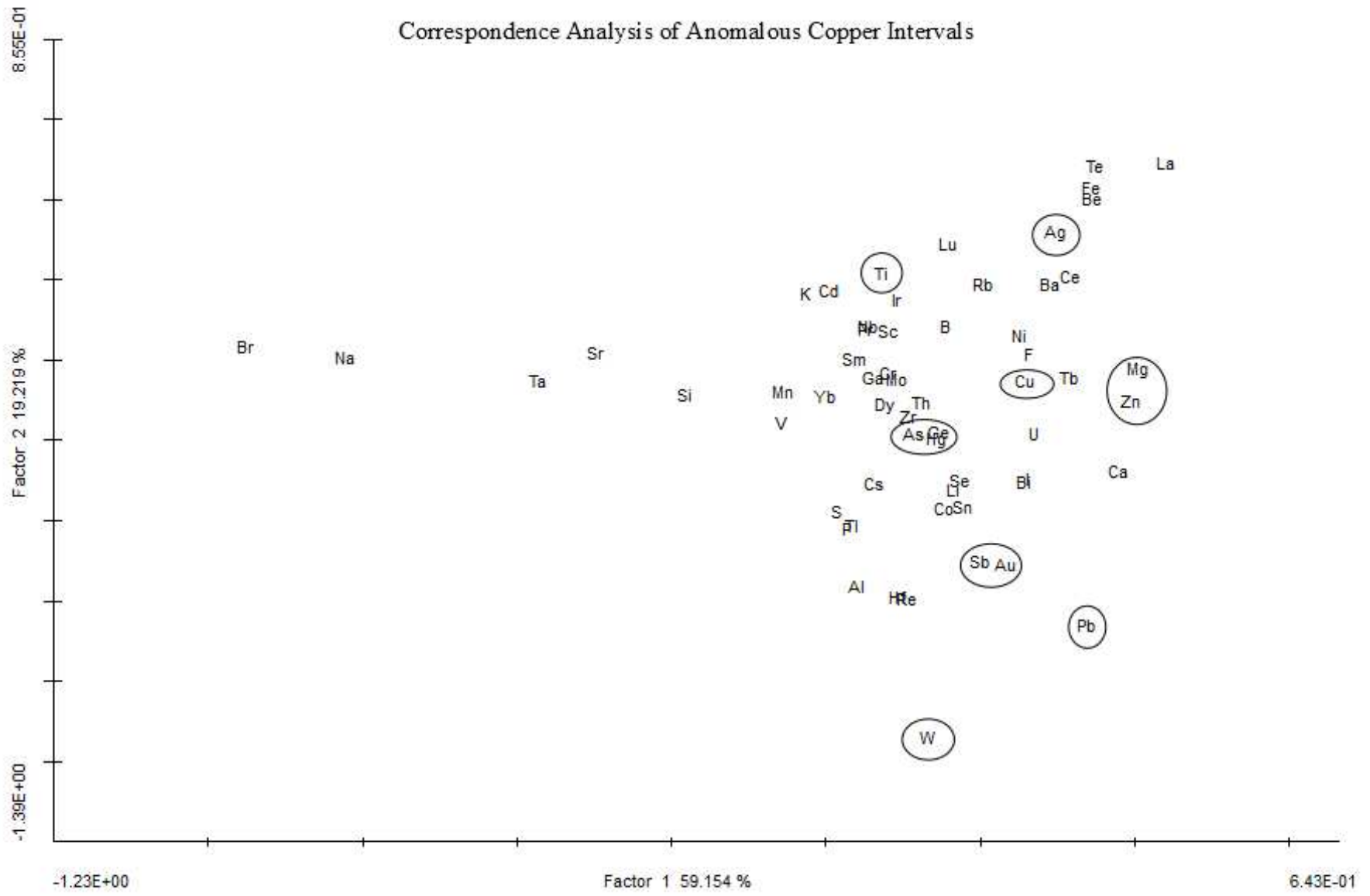


Figure 44: Correspondence analysis plot for intervals with anomalous copper. Plot of factors 1 and 2 with elements of interest circled.

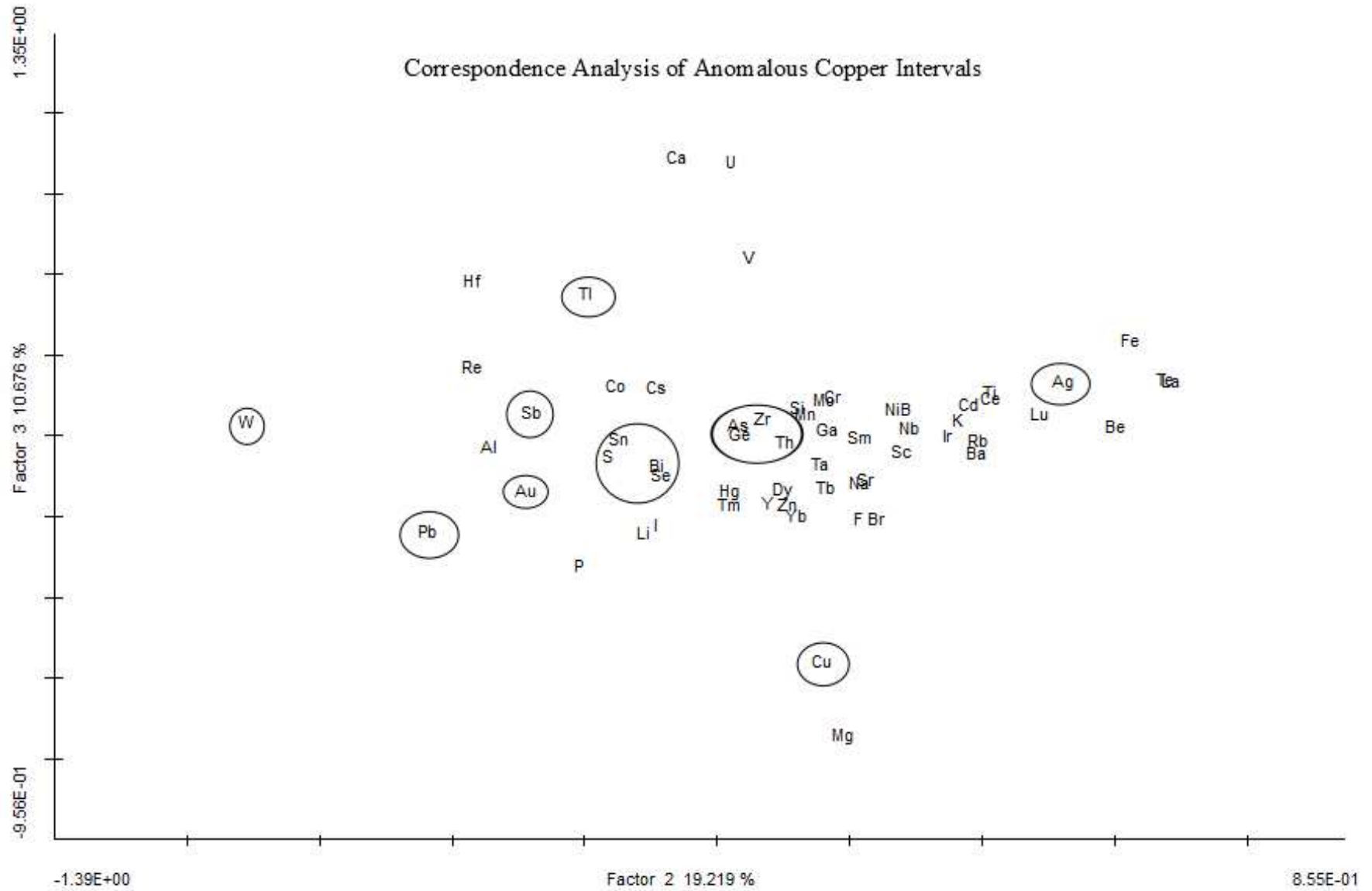


Figure 45: Correspondence analysis plot for factors 2 and 3 from data below the leach cap where copper is anomalous. Elements of interest are circled.

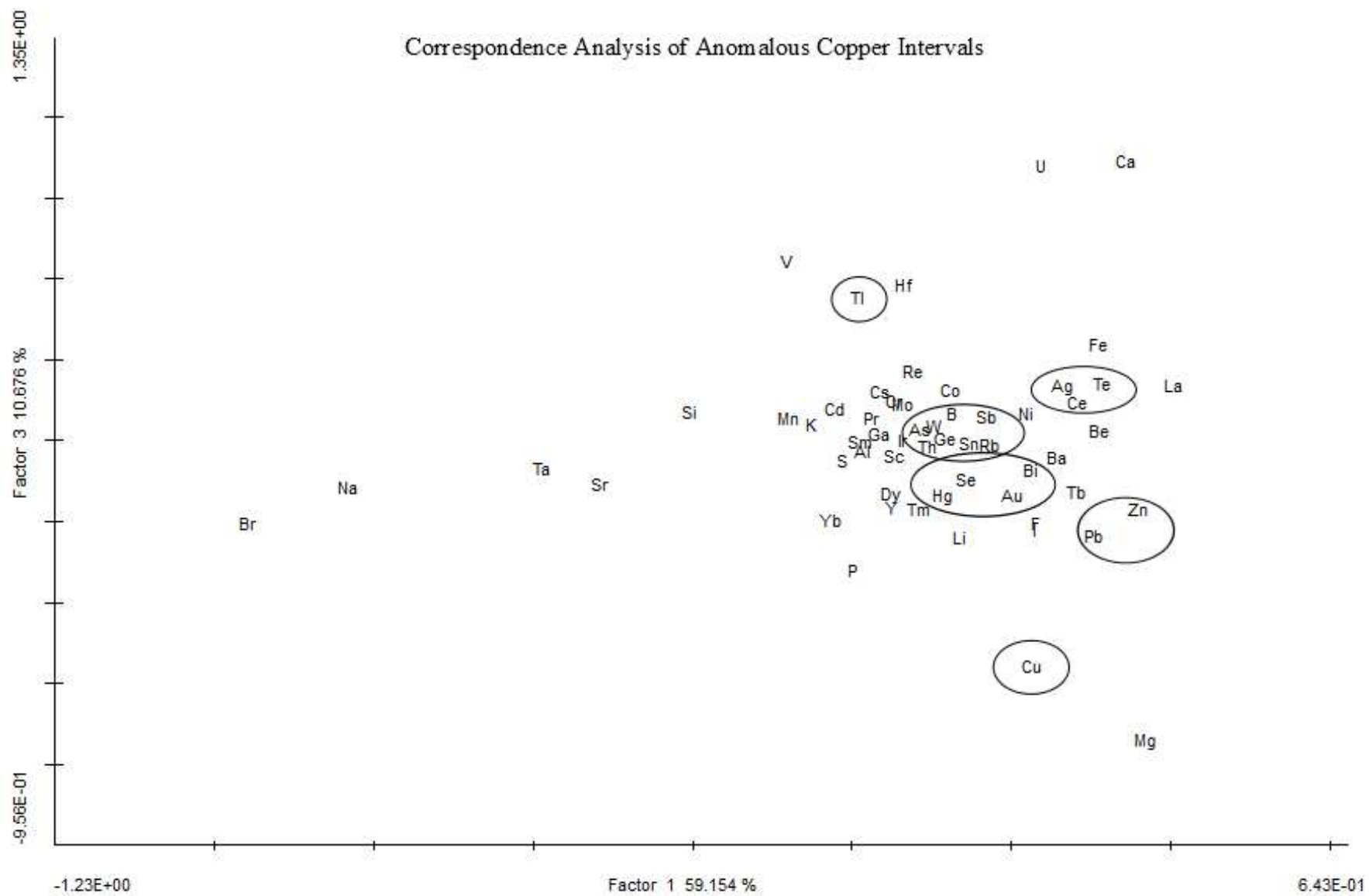


Figure 46: Correspondence analysis of anomalous copper intervals below leach cap. Plot of factors 1 and 3 with elements of interest circled.

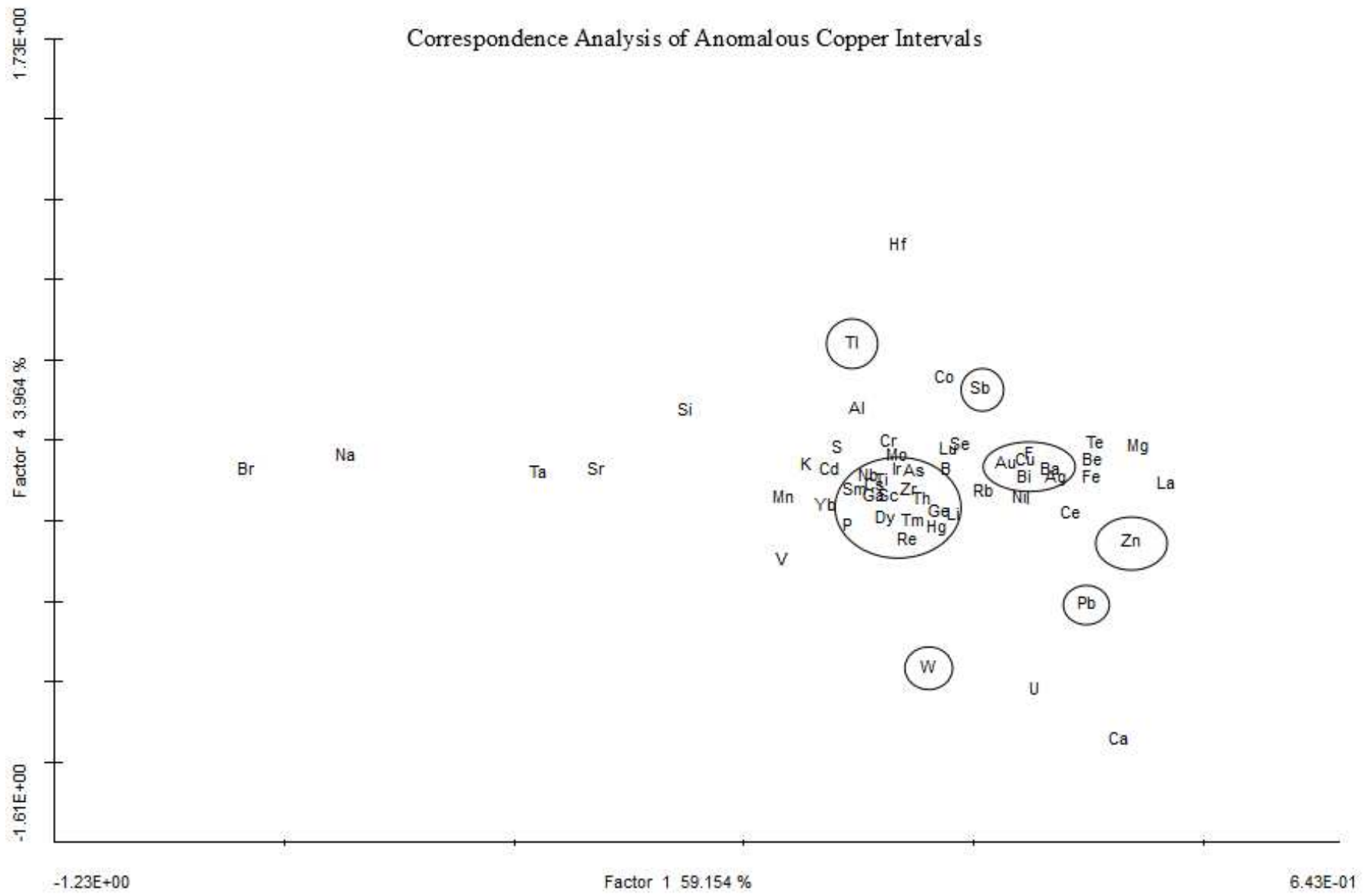


Figure 47: Correspondence plot of anomalous copper intervals below leach cap. Plot of factors 1 and 4 with elements of interest circled.

Principal Component Analysis

PCA was done using ioGas' built in software package and for each leveled dataset from the previous calculations (below the leached cap, anomalous gold intervals below the leached cap, and anomalous copper intervals below the leached cap). The strongest factors were chosen, based on their loadings, to be displayed. Factors identified as being related to either ore system were then imported to LeapFrog and used to make corresponding interpolant shapes that can be compared to ore shells created by Newmont.

Below Leached Cap Principal Component Analysis, as shown in Table 1, shows three factors with strong loadings that show similar trace element associations to the corresponding correlation matrix and correspondence analysis.

Factor PC2 (Table 1) shows strong loadings (> 0.5) of silver (0.6538), arsenic (0.6352), bismuth (0.6096), cobalt (0.7416), iron (0.6699), manganese (0.5877), nickel (0.6019), lead (0.5703), sulfur (0.7046), antimony (0.6022), tin (0.5452), thallium (0.5939), and zinc (0.6446). Factor PC2 also shows strong negative loadings (< -0.5) of calcium (-0.7589) and strontium (-0.7022). This factor shows a strong loading of both base metal associated elements such as lead and zinc as well as some typically Carlin associated elements of antimony, thallium, and arsenic. Negative loadings of calcium and strontium have been reported by Patterson (2005) as proxies for Carlin-type decarbonatization alteration styles. Figure 48 is a spatial plot of factor PC2 against the modeled gold shells and lithology. The plot of factor PC2 shows spatial proximity with the extent of the gold shape.

Factor PC3 (Table 1) shows strong loadings of gold (0.5764), silver (0.496), arsenic (0.5022), calcium (0.5309), copper (0.5534), mercury (0.5746), and tellurium (0.6469). This factor is also plotted spatially on Figure 49 to show the overlapping between factor 3 and the modeled gold grade shells. This factor contains some of the elemental signature found within Carlin mineralization..

Factor PC4 (Table 1) shows strong loadings of copper (0.5288), phosphorous (0.5071), uranium (0.5433), and vanadium (0.5338). This pattern is also seen in some redbed sedimentary rock-hosted copper-uranium deposits (M. Coolbaugh personal communication, 2014) but may be attributed to input of some oxidation effects on rocks thought to be completely below the leached cap and transitions zone. Patterson (2005) recognized similar loadings as a "phosphate group," in the Jerritt Canyon district.

Below Leached Cap PCA									
Element	PC1	Element	PC2	Element	PC3	Element	PC4	Element	PC5
Sm	0.829	Co	0.7416	Te	0.6469	U	0.5433	Cr	0.4543
La	0.8242	S	0.7046	Au	0.5764	V	0.5338	Th	0.4395
Ce	0.8191	Fe	0.6699	Hg	0.5746	Cu	0.5288	U	0.4247
Al	0.8165	Ag	0.6538	Cu	0.5534	P	0.5071	Mo	0.4084
Li	0.7636	Zn	0.6446	Ca	0.5309	Zr	0.4701	Sb	0.3775
Be	0.7629	As	0.6352	As	0.5022	Mo	0.4231	Tl	0.3656
Rb	0.7578	Bi	0.6096	Ag	0.496	Sn	0.418	Ce	0.335
K	0.7532	Sb	0.6022	W	0.4765	Ni	0.4066	Zr	0.3158
Na	0.7198	Ni	0.6019	Sr	0.4534	Ti	0.3962	S	0.2615
Sc	0.7071	Tl	0.5939	Si	0.4213	Bi	0.3546	Sm	0.2587
Cs	0.666	Mn	0.5877	Yb	0.4192	Y	0.3485	Cs	0.2538
Mg	0.6261	Pb	0.5703	Tl	0.3991	Zn	0.3421	As	0.2423
Th	0.6098	Sn	0.5452	Sb	0.389	Si	0.3093	La	0.215
Fe	0.5465	Au	0.4887	Bi	0.3644	Se	0.3004	Hg	0.1954
Ti	0.4938	Te	0.3656	Sn	0.3266	Pb	0.2926	V	0.1776
Co	0.4745	Cr	0.234	S	0.3122	Cr	0.2513	Na	0.1488
Y	0.4712	Zr	0.2191	Pb	0.2704	Rb	0.2116	Se	0.1474
Zr	0.4523	Cu	0.1957	Y	0.2588	Co	0.1907	Au	0.08733
Yb	0.433	Th	0.1803	K	0.2532	W	0.1855	Li	0.08384
Mn	0.4309	Cd	0.178	Sc	0.2518	Li	0.1835	Al	0.02182
Zn	0.3491	Sc	0.1561	Mo	0.2502	Ba	0.1817	Mg	0.002561
Ba	0.331	Cs	0.1049	Mg	0.2424	Te	0.1685	Si	3.74E-04
Ni	0.3199	Hg	0.04007	Na	0.2351	Al	0.1527	K	-0.01375
Sr	0.2999	Be	0.001178	V	0.2242	Cd	0.1398	Ni	-0.03938
Sn	0.2863	Al	-0.01244	Rb	0.1618	K	0.1342	Sn	-0.04163
Tl	0.1274	Mo	-0.05397	La	0.121	Sm	0.08717	Rb	-0.06463
Ca	0.08553	Si	-0.08221	Ba	0.103	Th	0.06621	Y	-0.06585
Ag	0.04752	U	-0.09808	Sm	0.08353	Yb	0.02899	P	-0.07859
S	0.04559	Ce	-0.09944	Ce	0.06964	La	0.01398	Ba	-0.08309
Te	-1.39E-04	Li	-0.1319	P	0.06653	Ag	0.01316	Yb	-0.08416
Sb	-0.009	Sm	-0.1342	Cs	0.01882	Mn	0.002625	Co	-0.08827
Bi	-0.03044	La	-0.1755	Mn	0.01306	Na	-0.01828	Ca	-0.09139
As	-0.03061	P	-0.2216	Al	-0.03418	Ce	-0.02573	Sc	-0.1039
Si	-0.04352	Se	-0.2369	Li	-0.03963	Cs	-0.04932	Be	-0.1097
Cd	-0.05053	Rb	-0.2606	Se	-0.05749	S	-0.08648	Ti	-0.1295
Au	-0.09767	Na	-0.2715	U	-0.07924	Fe	-0.08741	Cd	-0.1671
Se	-0.1257	Ti	-0.2751	Cd	-0.1228	Be	-0.09085	Bi	-0.178
Pb	-0.1411	Ba	-0.2933	Cr	-0.1521	Sr	-0.1049	Zn	-0.1851
Cu	-0.2188	W	-0.3024	Zr	-0.1776	Hg	-0.1098	Pb	-0.1922
Hg	-0.2545	K	-0.3173	Be	-0.1865	Ca	-0.1293	Sr	-0.1927
P	-0.2989	Mg	-0.4281	Ti	-0.1924	Sc	-0.1451	W	-0.199
Mo	-0.4317	Y	-0.4325	Th	-0.2058	Sb	-0.1586	Cu	-0.2063
W	-0.4569	Yb	-0.4407	Co	-0.2888	Mg	-0.2365	Fe	-0.2203
U	-0.4768	V	-0.4831	Fe	-0.2933	As	-0.276	Te	-0.2502
V	-0.4824	Sr	-0.7022	Zn	-0.3135	Au	-0.349	Ag	-0.2626
Cr	-0.5556	Ca	-0.7589	Ni	-0.3788	Tl	-0.3639	Mn	-0.4323
Variance %	23.38		18.12		10.37		7.602		5.159

Table 1: PCA results of data from below the leached cap. Values >0.5 are bolded and values < -0.5 are bolded and italicized.

Anomalous Gold Intervals Below Leached Cap Principal Component Analysis shows three interesting factors that can be correlated to multiple mineralization events (Table 2). Attempted spatial plots of these factors did not yield meaningful results, likely because of the restricted dataset.

PC2 shows strong loadings of cobalt (0.9103), iron (0.8462), nickel (0.7175), and zinc (0.8108). PC2 also shows negative loadings of calcium (-0.7514), chromium (\square 0.6512), molybdenum (\square 0.6393), silicon (\square 0.6194), uranium (\square 0.5563), and vanadium (0.6184).

PC3 shows high negative loadings of bismuth (-0.7327), copper (-0.7123), phosphorous (-0.5449), lead (-0.5352), tin (-0.8434), tellurium (-0.6066), and tungsten (\square 0.5144). The negative loadings of these elements may indicate the signature of a proximal intrusion-related skarn (M. Coolbaugh personal communication, 2014).

PC4 shows the most interesting loadings by displaying high loadings of the Carlin signature elements of gold (0.5735), arsenic (0.6977), mercury (0.7598), sulfur (0.7017), antimony (0.6967), and thallium (0.8398). This is also reflected in the correlation matrices and correspondence analysis plots.

Anomalous Gold Intervals Below Leached Cap PCA									
Element	PC1	Element	PC2	Element	PC3	Element	PC4	Element	PC5
K	0.8537	Co	0.9103	Sr	0.1784	Tl	0.8398	Th	0.5079
Sm	0.8223	Fe	0.8462	Au	0.1484	Hg	0.7598	Cd	0.4593
La	0.8215	Zn	0.8108	Cs	0.1454	S	0.7017	Mn	0.4221
Ce	0.8211	Ni	0.7175	Mg	0.1452	As	0.6977	Y	0.4183
Rb	0.8041	Al	0.4707	Cd	0.1346	Sb	0.6967	Sm	0.3869
Be	0.7945	S	0.4464	Yb	0.1129	Au	0.5735	Yb	0.381
Mg	0.7673	As	0.3825	Ca	0.08034	Ag	0.4789	P	0.3773
Li	0.7567	Se	0.3543	Sc	0.07341	K	0.3023	Sc	0.3288
Sr	0.6818	Mn	0.3437	Be	0.00155	Yb	0.2505	La	0.2981
Ti	0.6796	Be	0.2905	K	-0.01818	Cs	0.245	Ce	0.292
Sc	0.6664	Zr	0.283	Al	-0.04333	Y	0.2088	Se	0.2913
Th	0.6636	Cs	0.271	Na	-0.04362	Mg	0.1949	U	0.2541
Na	0.6373	Sc	0.2707	Ba	-0.04733	Sc	0.1886	Mg	0.2188
Al	0.6275	Cd	0.2471	Ce	-0.06193	Rb	0.1778	Cr	0.1698
Cs	0.5981	Li	0.2229	Tl	-0.06874	Sr	0.1699	Sn	0.1409
Ca	0.495	Tl	0.2057	Li	-0.08391	Ca	0.1081	Fe	0.1158
Mn	0.4579	Rb	0.08038	La	-0.09978	Si	0.08382	Ca	0.1109
Zr	0.4461	Sn	0.06886	Si	-0.1024	Te	0.07787	As	0.0777
Y	0.4386	Bi	0.06619	S	-0.1057	Fe	0.07587	Mo	0.07086
Ba	0.4059	Pb	0.05505	Cr	-0.1296	Sm	0.05785	Be	0.06984
Yb	0.3735	Th	0.04195	Sm	-0.1535	Mo	0.05129	Pb	0.03814
Te	0.2757	Sm	0.01815	Rb	-0.1909	P	0.04299	Sb	0.007943
Fe	0.254	Y	-0.02167	Se	-0.1986	Cr	0.03906	Hg	0.001567
Si	0.1916	K	-0.06105	Hg	-0.2011	Pb	-9.95E-04	Zn	-0.0186
Au	0.1539	Sb	-0.06403	As	-0.207	Al	-0.01405	Cu	-0.03468
Co	0.08204	Te	-0.08265	Co	-0.2158	Sn	-0.01614	V	-0.0417
Ni	0.06517	Ag	-0.1282	Ti	-0.2221	La	-0.02745	Tl	-0.0676
Mo	0.04649	Ce	-0.1513	Th	-0.2325	Ce	-0.03421	S	-0.07207
Bi	0.009136	La	-0.1519	Fe	-0.2385	Th	-0.05779	Ag	-0.09534
P	-0.03854	P	-0.207	Y	-0.2571	Li	-0.06919	Ti	-0.126
Se	-0.06197	Hg	-0.2076	Mn	-0.2791	Co	-0.08701	Au	-0.1276
Tl	-0.09065	Na	-0.2293	V	-0.3547	Be	-0.09022	Co	-0.1347
Zn	-0.1097	Ti	-0.2366	Zr	-0.3561	Mn	-0.1044	Ni	-0.1577
Sn	-0.1216	Au	-0.2372	Mo	-0.3735	Ba	-0.1177	K	-0.172
Sb	-0.1233	Cu	-0.3061	Zn	-0.3827	Na	-0.1331	Sr	-0.1924
Cr	-0.1306	Yb	-0.3222	Ni	-0.4016	Cu	-0.1431	Bi	-0.1968
V	-0.1616	Mg	-0.3334	Sb	-0.4458	Zr	-0.1687	Rb	-0.2054
S	-0.1662	Ba	-0.3569	Ag	-0.4713	U	-0.1737	Li	-0.2299
U	-0.212	Sr	-0.3843	U	-0.5106	Ni	-0.1822	Cs	-0.2411
W	-0.2147	W	-0.4878	W	-0.5144	Bi	-0.1833	W	-0.2627
As	-0.2502	U	-0.5563	Pb	-0.5352	W	-0.1879	Zr	-0.3001
Ag	-0.2518	V	-0.6184	P	-0.5449	Zn	-0.2115	Te	-0.3654
Cu	-0.256	Si	-0.6194	Te	-0.6066	Cd	-0.2353	Si	-0.3915
Cd	-0.2874	Mo	-0.6393	Cu	-0.7123	V	-0.2857	Ba	-0.413
Pb	-0.3223	Cr	-0.6512	Bi	-0.7327	Se	-0.3153	Al	-0.4758
Hg	-0.3716	Ca	-0.7514	Sn	-0.8434	Ti	-0.4177	Na	-0.5471
Variance %	22.3		16.6		11.08		9.658		7.236

Table 2: Table of PCA results from intervals below the leached cap where gold is anomalous. Elements are sorted by factor loadings. > 0.5 bolded; < -0.5 bolded and italicized.

Anomalous Copper Intervals Below Leached Cap Principal Component Analysis shows segregation of precious and base metals (Table 3). PC3 shows high loadings of zinc (0.6757), lead (0.6692), and cadmium (0.9037). PC4 consists of high loadings of gold (0.5865), antimony (0.5865), thallium (0.543), tellurium (0.5243), as well as chromium (0.7032). The segregation of metals between these two factors suggests separate mineralization events.

Copper Anomalous Intervals Below Leached Cap PCA									
Element	PC1	Element	PC2	Element	PC3	Element	PC4	Element	PC5
K	0.9813	Ti	0.6782	Cd	0.9037	Cr	0.7032	U	0.711
Rb	0.9399	Ba	0.5263	Zn	0.6757	Sb	0.5939	Tl	0.6903
Mg	0.9139	Co	0.422	Pb	0.6692	Au	0.5865	Zr	0.5229
Sm	0.8785	Na	0.3625	Li	0.4652	Tl	0.543	V	0.4204
Ce	0.8731	Al	0.3241	Co	0.4504	Te	0.5243	Th	0.3855
La	0.8705	Li	0.3055	Sb	0.408	Na	0.3816	Ni	0.3778
Th	0.8156	Ce	0.2777	Be	0.4049	Li	0.3613	Zn	0.3769
Ni	0.8055	Se	0.2632	Mn	0.3659	Cs	0.36	Mo	0.3013
Cs	0.7873	La	0.2403	Fe	0.3394	Bi	0.3588	Cd	0.2242
Be	0.7793	U	0.2369	Ni	0.3211	Hg	0.3452	S	0.2202
Sc	0.7721	Mg	0.2045	Se	0.243	Al	0.3167	Hg	0.2189
Te	0.7689	Cs	0.1859	Ag	0.2149	Si	0.3094	Sm	0.198
Zr	0.7683	V	0.1762	Y	0.1492	Cu	0.2522	Cu	0.1968
Bi	0.7353	Te	0.1752	Al	0.1442	Be	0.2177	Cr	0.1698
Al	0.7255	Sc	0.1611	Ba	0.1397	Ag	0.2112	Co	0.1586
Co	0.7147	Cd	0.1179	Rb	0.1234	Ba	0.1765	Rb	0.1522
Li	0.7115	Sm	0.06801	U	0.09259	Mg	0.1687	Sb	0.1386
Mo	0.6969	Zr	0.03389	Sc	0.08983	Ni	0.1566	Cs	0.1325
Y	0.689	Ni	0.0125	Bi	0.0891	Fe	0.1546	Ce	0.1169
Yb	0.6827	Tl	-0.00912	Sn	0.08251	Ti	0.1257	La	0.1041
Sr	0.6817	K	-0.02096	Th	0.05199	Sn	0.1156	Pb	0.08031
Fe	0.6511	Sr	-0.03681	Yb	-0.00965	Pb	0.08546	Mg	0.05216
Mn	0.5899	Rb	-0.04433	Cr	-0.02453	As	0.05143	K	0.04642
Ti	0.5882	Si	-0.05099	Te	-0.0367	Co	0.04084	Sc	0.03798
Ca	0.5511	Mo	-0.06173	Zr	-0.05823	V	-0.02551	Y	0.02152
Zn	0.5278	Cu	-0.08633	K	-0.08502	Zn	-0.04156	Li	0.01649
Na	0.5109	Be	-0.08806	P	-0.1027	K	-0.06866	As	0.01556
Sn	0.4738	Bi	-0.135	Mg	-0.1154	Ce	-0.1006	Ag	0.01522
Si	0.4398	Hg	-0.1586	Sm	-0.1428	S	-0.1033	Sn	-0.0609
Ba	0.4227	Th	-0.2018	Ti	-0.1652	La	-0.1144	Au	-0.07106
Ag	0.3226	Zn	-0.316	Au	-0.2197	Cd	-0.1243	Te	-0.07851
P	0.2595	Cr	-0.3193	Ce	-0.2575	Mn	-0.1265	Ca	-0.1238
S	0.1804	Ca	-0.3755	La	-0.2746	Rb	-0.159	W	-0.1278
Cu	0.1782	Y	-0.444	Na	-0.2793	U	-0.1595	Yb	-0.1702
Tl	0.1437	Yb	-0.4763	Cs	-0.2961	Mo	-0.1721	Al	-0.1893
Pb	0.1127	Fe	-0.5292	Hg	-0.3247	Zr	-0.1865	Se	-0.205
V	-0.05102	Mn	-0.5709	W	-0.3273	Sr	-0.2322	P	-0.2125
As	-0.08169	Sb	-0.5901	Cu	-0.3464	Ca	-0.2435	Sr	-0.2208
Sb	-0.1416	W	-0.6141	Tl	-0.3617	Sc	-0.2495	Ti	-0.24
Cd	-0.1836	Au	-0.6754	Mo	-0.3903	Th	-0.2712	Si	-0.2555
Au	-0.2578	Pb	-0.7024	As	-0.396	P	-0.2745	Fe	-0.2803
U	-0.3097	Sn	-0.7624	S	-0.454	Sm	-0.3475	Mn	-0.284
W	-0.3341	S	-0.7884	V	-0.4701	W	-0.419	Be	-0.3135
Se	-0.3573	As	-0.8547	Sr	-0.5906	Yb	-0.4208	Na	-0.3267
Cr	-0.3856	P	-0.8592	Ca	-0.6583	Y	-0.4307	Bi	-0.3339
Hg	-0.7572	Ag	-0.8822	Si	-0.7097	Se	-0.7162	Ba	-0.5115
Variance %	37.57		18.04		12.97		9.997		7.48

Table 3: PCA of copper anomalous intervals below the leached cap. Values > 0.5 are bolded and values < -0.5 are bolded and italicized.

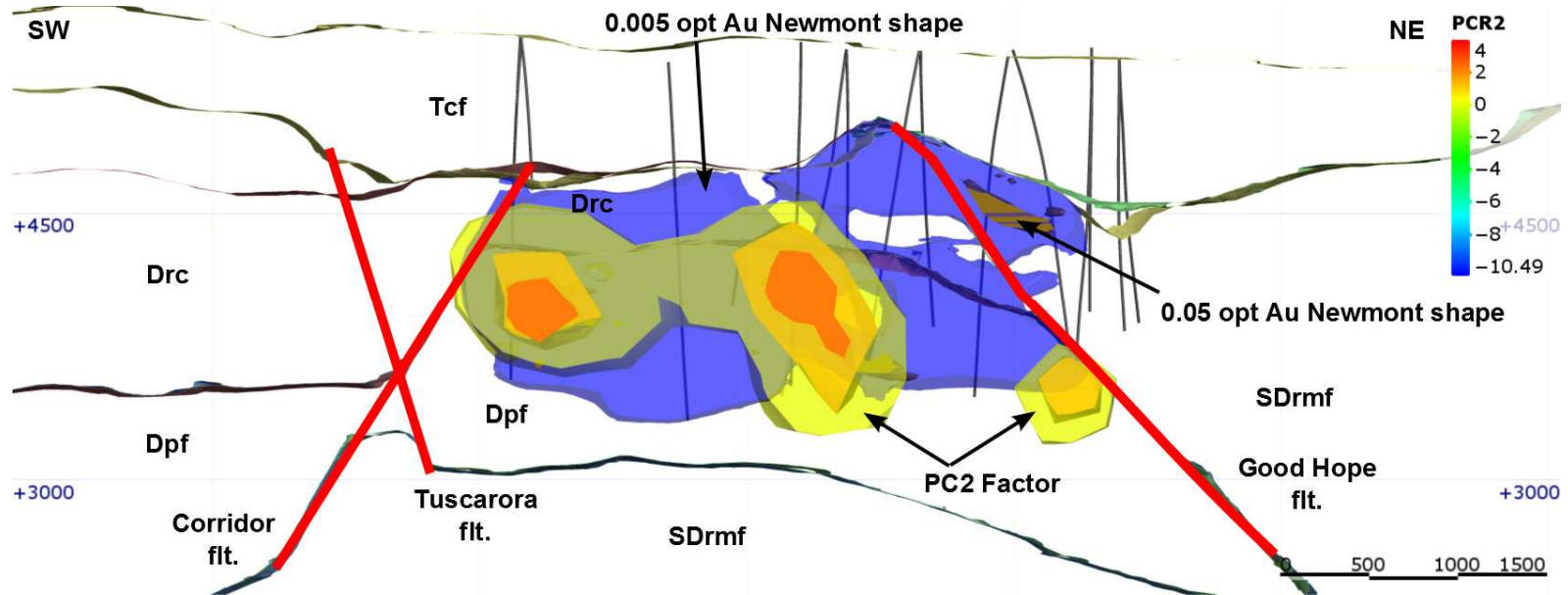


Figure 48: Spatial plot of PC2 from PCA of data below the leached cap. Annotated to show gold concentration shells, drill traces, major structures, and lithology. No vertical exaggeration; vertical scale is feet above sea level (blue numbers along vertical of figure), horizontal scale is meters. Scale shows warmer colors as areas of higher factor concentration. Blue enclosure is low grade gold ore zone based on Newmont modeling; brown enclosure is high grade gold ore zone. Note the general overlap of warmer colored enclosures of PC2 with annotated low (blue) and high (brown) grade gold shells. The PC2 factor is interpreted to be cospatial zones of both Carlin-type gold and base metal mineralization, and warmer colors are zones of higher concentration of associated groupings of elements. The elements of high loadings within PC2 reflect this suspected overlap of ore systems (Table 1).

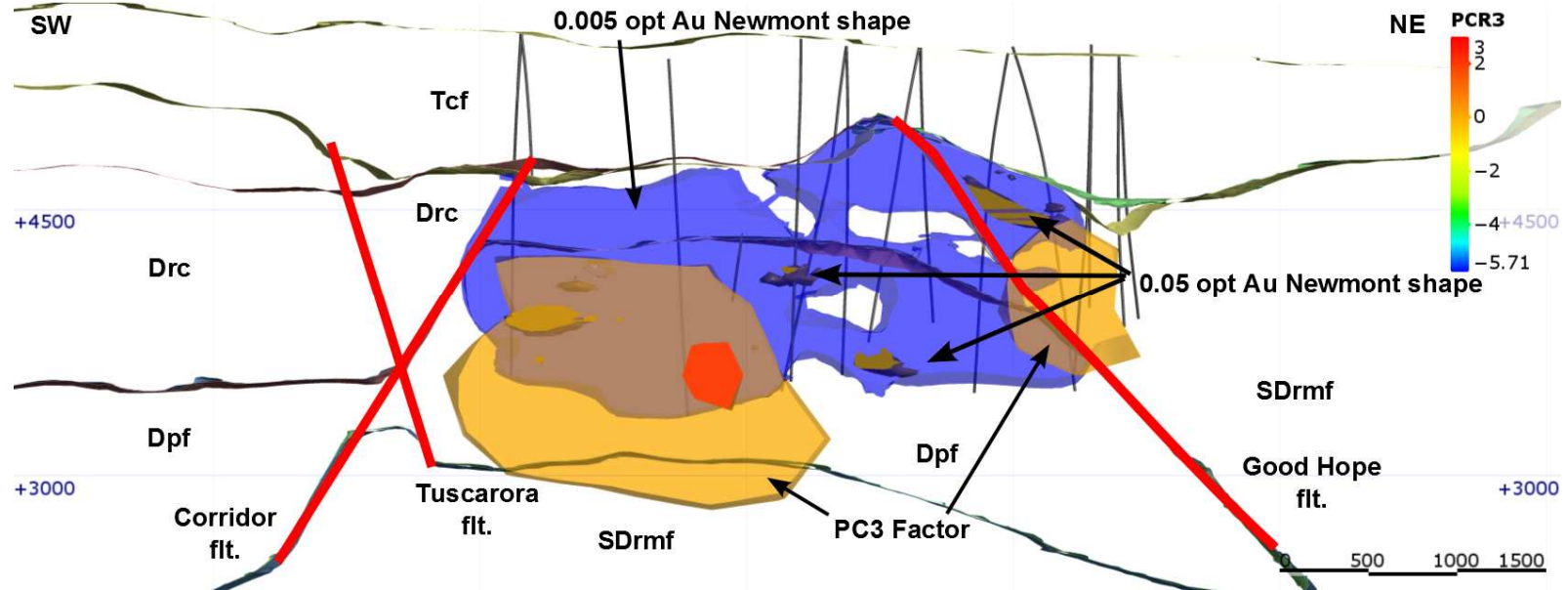


Figure 49: Spatial plot of PC3 from analysis of data below the leached cap. Scale shows warmer colors of higher PC3 values. Warmer colors of enclosures show an increase in abundance of grouped elements of factor PC3. Factor PC3 is interpreted to be Carlin-type gold mineralization and is reflected by the associated elements found in Table 1. Note relationship to gold concentration shells (blue enclosure is low grade, brown enclosure is high grade based on Newmont modeling shapes). Major structures and lithologies are annotated. No vertical exaggeration. Vertical scale in feet (blue numbers along vertical edges of figure), horizontal scale in meters.

Sulfur Isotope Analysis

Methods

Following the establishment of paragenetic relationships between sulfides, a suite of 6 samples were selected for stable isotope $\delta^{34}\text{S}$ analysis. This study was suggested by Peter Vikre, USGS, in order to evaluate sources of sulfur in sulfides at the Mike deposit (P. Vikre, personal communication, 2013). Base metal sulfide samples of galena, sphalerite, and chalcopyrite were chosen on the basis of being macroscopic and microscopically distinct mineral phases with no discernible intergrowths with other sulfides. Sphalerite and galena (187-1762.5 sp and 187-1762.5 gn), determined to be in equilibrium by petrography, were selected for $\delta^{34}\text{S}$ analysis and geothermometry calculations using the equation in Ohmoto and Rye (1979) (Table 4) (Fig. 52). Samples were ground into powder using a Dremel tool and placed into labeled glass vials. Care was taken to keep samples pure and uncontaminated by other minerals. These samples were then submitted to Simon Poulson at the Nevada Stable Isotope Lab on the University of Nevada, Reno campus. Samples were analyzed using the lab's Micromass Isoprime stable isotope ratio mass spectrometers and values were reported to the author. Values were then compared to compilations by Ohmoto (1986) and Ohmoto and Rye (1979), and isotope equilibrium temperatures were calculated for the sphalerite and galena pair.

$\delta^{34}\text{S}$ Results

The reported $\delta^{34}\text{S}$ values for all sulfides samples range from 3.4‰ to 6.7‰ (Table 4). The low variation in the measured values indicate little fractionation between phases

and a similar source of sulfur for the mineral phases (Ohmoto and Rye, 1979; Ohmoto, 1986). Based on the measured $\delta^{34}\text{S}$ values, the depositional fluids of the base metal sulfide phases were likely magmatically derived, but likely assimilated the sulfur characteristics of earlier sedimentary sulfur (Ohmoto, 1986; Ohmoto and Rye, 1979; Fig. 50). Measured isotopic values also show a similar pattern to other $\delta^{34}\text{S}$ values for porphyry copper deposits in North and South America (Fig. 51). Other $\delta^{34}\text{S}$ values, from the Carlin trend, have been aggregated and reported by Cline et al. (2005) that include pyrite values, which likely include sedimentary signatures (Fig. 53). These values are all greater than those reported in Table 4 for the samples of base metal sulfides. The values aggregated by Cline et al. (2005) show intrusion related mineralization isotopic values that have a wide range. The samples analyzed from the Mike thesis samples fit within this range (Fig. 53).

Sample	$\delta^{34}\text{S}_{\text{VCDT}}$ (‰)	Notes
153-1701 cpy	5.6	chalcopyrite
153-1891 cpy	4.8	chalcopyrite
187-1762.5 sp	5.5	sphalerite
195A-1911 sp	6.7	sphalerite
187-1762.5 gn	3.8	galena
188-1902A gn	3.4	galena
Temperature calculated from sphalerite-galena pair (187-1762.5) using equation from Ohmoto and Rye (1979)		401.77 C - 355.75 C +/- 20

Table 4: Table of sulfur isotope analyses and calculated isotope equilibrium temperatures using sphalerite and galena pair from sample 187-1762.5 (highlighted in bold).

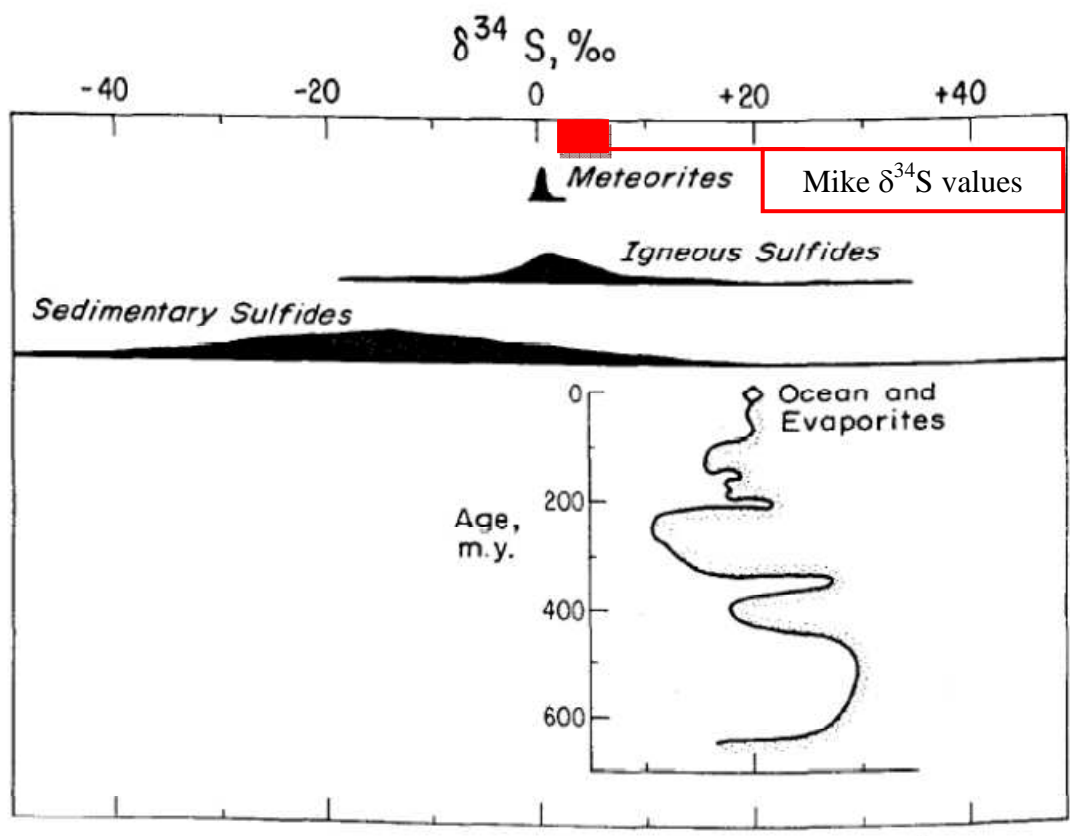


Figure 50: Figure displaying range of measured values of $\delta^{34}\text{S}$ values for sedimentary and igneous rocks as well as meteorites. Ocean values and evaporites through time are also shown. Mike study results annotated in red to show comparison (modified from Ohmoto and Rye, 1979).

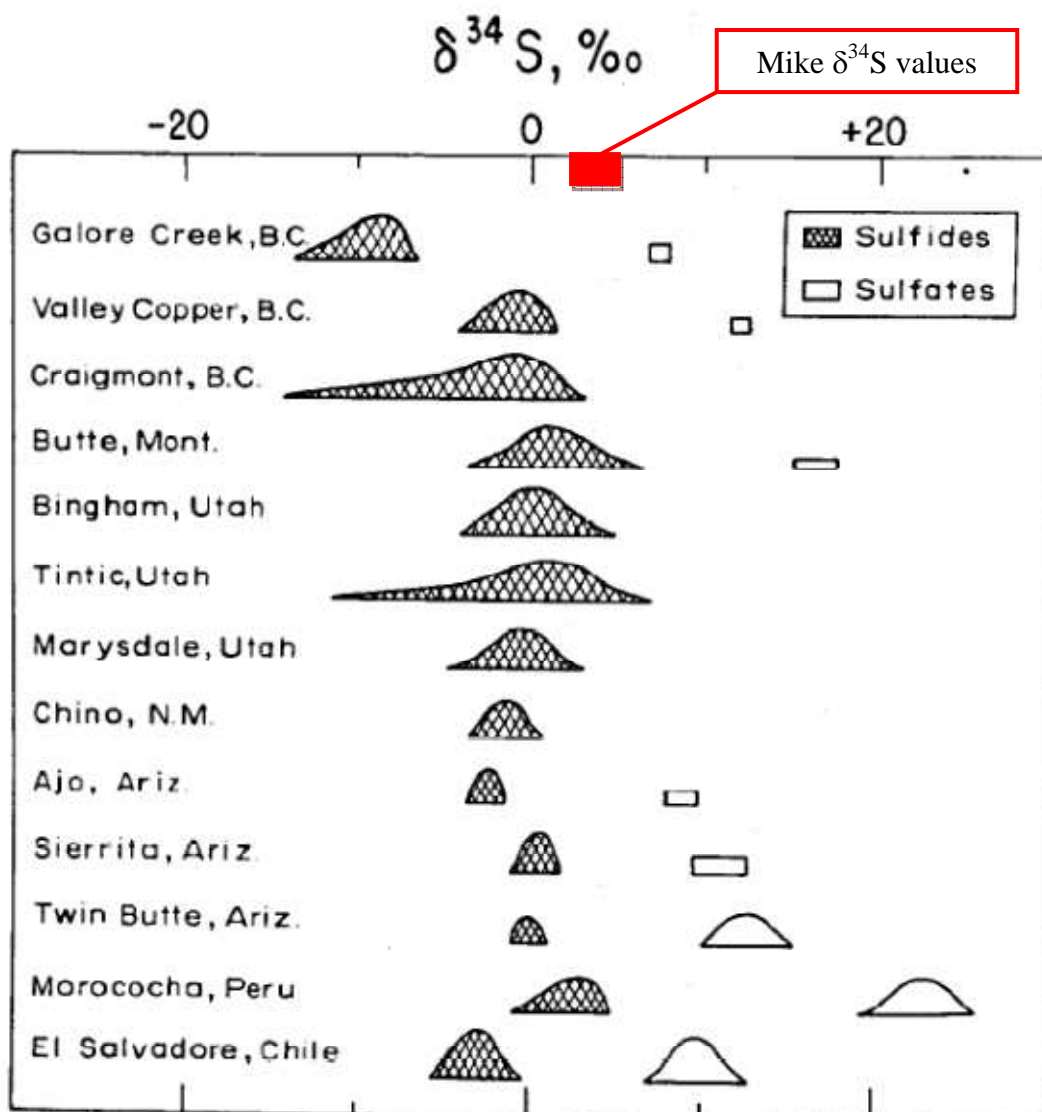


Figure 51: Modified from Ohmoto and Rye (1979). Figure showing measured sulfur isotope values for sulfides and sulfates from specific porphyry copper deposits. Mike study results annotated.

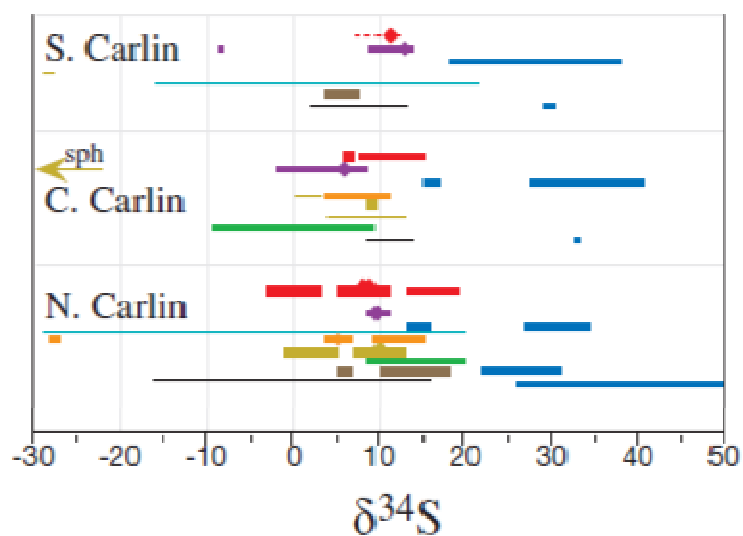
Isotope equilibrium temperatures were calculated for the sphalerite and galena pair from sample 187-1762.5. This was due to the pair being petrographically observed in equilibrium and mineralogically distinct. The other sphalerite and galena samples could not be constrained to these assumptions. Using the equation listed in Figure 52

from Ohmoto and Rye (1979), temperatures 401.77°C and $355.75^\circ\text{C} \pm 20^\circ$, were calculated.

Mineral Pair	Equation (T in Kelvin; $\Delta = \delta^{34}\text{S}_A - \delta^{34}\text{S}_B$)	Uncertainties ^a	
		1	2
Sulfates-chalcopyrite	$T = \frac{2.85 \times 10^3}{(\Delta \pm 1)^{1/2}} \quad (T > 400^\circ\text{C})$	$\pm 25^3$	$\pm 5^3$
	$T = \frac{2.30 \times 10^3}{(\Delta - 6 \pm 0.5)^{1/2}} \quad (T < 350^\circ\text{C})$	± 10	± 5
Sulfates-pyrite	$T = \frac{2.76 \times 10^3}{(\Delta \pm 1)^{1/2}} \quad (T > 400^\circ\text{C})$	$\pm 25^3$	$\pm 5^3$
	$T = \frac{2.16 \times 10^3}{(\Delta - 6 \pm 0.5)^{1/2}} \quad (T < 350^\circ\text{C})$	± 10	± 5
Pyrite-galena	$T = \frac{(1.01 \pm 0.04) \times 10^3}{\Delta^{1/2}}$	± 25	± 20
Sphalerite (pyrrhotite) -galena	$T = \frac{(0.85 \pm 0.03) \times 10^3}{\Delta^{1/2}}$	± 20	± 25
Pyrite-chalcopyrite	$T = \frac{(0.67 \pm 0.04) \times 10^3}{\Delta^{1/2}}$	± 35	± 40
Pyrite-pyrrhotite (sphalerite)	$T = \frac{(0.55 \pm 0.04) \times 10^3}{\Delta^{1/2}}$	± 40	± 55

^a1 = uncertainty in the calculated temperature due to the uncertainty in the equation (at $T = 300^\circ\text{C}$); 2 = uncertainty in the calculated temperature due to the analytical uncertainty of $\pm .2\%$ for Δ values (at $T = 300^\circ\text{C}$); 3 = uncertainties in the calculated temperature at $T = 450^\circ\text{C}$.

Figure 52: Table of geothermometry equations for sulfide pairs from Ohmoto and Rye (1979). Sphalerite-galena pair equation, outlined in red, was used for the Mike sample.



- ◆ Mean or mode
- H_2S (200°C, alunite proxy for main ore stage)
- H_2S (200°C, main ore stage)
- H_2S (150°C, late ore) stage)
- Supergene alunite
- Botryoidal py/mc (+/- sph)
- Carlin late ore stage Sb- and As-sulfides
- Carlin main ore stage iron
- Mixture syn/dia py and main ore stage iron sulfides
- Intrusion-related mineralization
- Sedex footwall (and MVT-like) mineralization
- Barite
- Syngenetic and diagenetic py +/- other sulfides

Figure 53: Modified figure from Cline et al. (2005) that shows aggregated sulfur isotope values for three parts of the Carlin trend. Note Central Carlin (C. Carlin) ranges of intrusion-related values (green) that include the Mike data.

Discussion and Conclusions

Petrography

Base metal mineralization overprinting and post-dating Carlin-type gold mineralization is in contrast to the petrographic report prepared by Larsen (internal Newmont report, 1994). Larsen observed more K-feldspar flooding and alteration. To date, thesis samples have only revealed two intervals in which K-feldspar is present, and one sample is within a vein. This, however, may be because the drill holes studied by Larsen in 1994 were further to the north-northwest than the holes that have been analyzed for this thesis. According to Branham and Arkell (1995), a hypothesized igneous source of the copper is located to the northwest based on geochemical data contours. It is, then, to be expected that calc-silicate hornfelsing and K-feldspar alteration products should increase to the northwest. This trend is seen in the samples analyzed in thin section with the best examples of calc-silicate hornfels and skarn being from drill hole locations to the north and west of the deposit. This pattern has been identified by both Norby and Orobona (2002) and Bawden (2002), and associated geophysical data show a cylindrical shaped body at approximately 1 km depth to the north of Mike.

analysis, in that it is a qualitative measurement of elemental concentrations, and not quantitative or that other pyrite generations were analyzed. Because the samples were not measured using LA-ICPMS, a true comparison cannot be drawn with the data shown in Large et al. (2009). A more comprehensive study including LA-ICPMS or SIMS of base metal and supposed Carlin-style rims on pyrite would be beneficial to the Mike project, as it could yield more useful information about the timing of the copper base metal and gold mineralization events at Mike in conjunction with petrographic results.

Geochemistry

In cross-examining the correlation matrices and correspondence analysis more robust correlations between single elements and multi-element groupings can be made (J. Carr, personal communication, 2014).

In data from intervals below the oxide zone at the Mike deposit, robust correlations based on data from the correlation matrix (Fig. 33) and factor plots of correspondence analysis (Figs. 36, 37 and 38) can only be made between copper and tellurium as well as gold, thallium, and antimony. Data from gold-anomalous intervals does not show any overlapping associations or correlations. Data from the anomalous copper intervals below the oxide zone only show an overlap between gold and mercury with a lesser association between gold, lead, and sulfur (Figs. 35, and 44-47).

A strong pattern across the multiple correlation matrices is present for gold and copper correlations when the data is compared. Gold correlates strongly throughout the Mike deposit with silver, arsenic, and antimony (Fig. 32-35). Gold also shows less extensive correlations with thallium and tellurium in both the bulk deposit correlation

matrix and the unoxidized deposit correlation matrix. Copper shows a strong association with bismuth, tin, tellurium, and tungsten. Lesser associations occur between copper and lead, silver, and molybdenum.

These correlations are also seen in the two forms of factor analysis performed on the data from ICP-MS analysis. Gold shows strong loadings with established Carlin signature elements including thallium, arsenic, antimony, mercury, and sulfur (Table 2). Base metals, especially copper, also share some factor loadings with gold, possibly indicating a small gold component to base metal mineralization (Table 1 and 2).

The gold at the Mike deposit shows a similar trace element signature to other Carlin-type deposits, as in Patterson and Muntean's 2011 paper on geochemistry at Jerritt Canyon. The presence of bismuth as a correlated element with copper, and gold in the bulk deposit data, suggests a magmatic source for primary copper. Other associated elements of tin, tellurium, and tungsten also support this (T. Thompson, personal communication, 2014). Combined analyses from several geochemical methods suggest confirmation that copper and gold are part of separate systems as hypothesized by Bawden (2002) as well as Norby and Orobona (2002), including a porphyritic source for the base metals. Geochemical relationships do not provide any details about timing relationships between the two ore systems.

Stable S Isotopes

$\delta^{34}\text{S}$ values for sphalerite, galena, and chalcopyrite from the Mike core thesis samples are within the range of other $\delta^{34}\text{S}$ values for intrusion-related mineralization along the Carlin trend. These values are also consistent with other porphyry related

deposit values from other localities (Ohmoto and Rye, 1979). These values are, however, higher than expected if the source were to have been purely magmatic in origin. The higher values are likely due to assimilation of sulfur from sedimentary pyrite and other sulfur-bearing minerals as the base metal-rich fluids rose and deposited sphalerite, galena, and chalcopyrite.

The equilibrium temperature calculated for the sphalerite and galena pair yields a temperature that would be expected to be associated with proximal to distal mineralization associated with a porphyritic or magmatic body. This temperature, however, can be called into question, as it is only one data point from the whole of the Mike deposit. Sphalerite and galena also have cross cutting relationships with each other, and so their interpretation of being in equilibrium may be suspect as well. More examples of sphalerite and galena pairs should be analyzed to better constrain isotopic values and calculated equilibrium temperatures. Isotope equilibrium temperatures could be compared to future fluid inclusion data to possibly link alteration minerals to the base metal event. Both the set of sulfur isotope values and the calculated equilibrium temperatures provide a good starting point for future sample analysis.

Future Work

Absolute age relationships would be important to establish at Mike, however, no suitable mineral species have been identified to be studied for reliable age dates. Even though apatite was found, its location was within a hydrothermally altered fault and was deemed not suitable for fission track dating methods due to the low annealing temperature of apatite (T. Thompson, personal communication, 2013). Adularia has only

been found in two locations, but was not of enough quantity, and could not be linked to the copper-base metal ore event. Igneous dikes, including the lamprophyre dike, have undergone severe clay alteration, leaving little in the way of suitable minerals for radiometric dating. Biotite from the lamprophyre dike could be dated, since it is a primary phenocryst, but it is unrelated to the copper-base metal event, and would not provide an age of mineralization.

No molybdenite has been found in petrographic work or macroscopic study. Radiometric dating methods on other sulfide minerals, including pyrite and chalcopyrite have not proved to provide reliable and tight constraints on age dates (M. Ressel and T. Thompson, personal communications, 2013). However, a study on low osmium pyrrhotite from the Chaoshan gold skarn in China has shown promising results as a potentially suitable mineral for radiometric dating (Wang et al., 2008). Re-Os dating of low osmium sulfides, determined by SEM analysis, could potentially show some promise in dating sulfides at the Mike deposit.

Expanding the geochemical analysis to include historical drill data would be the next step in understanding the geochemical signature of the two ore systems at Mike. Total digestion of unaltered, or weakly altered, host lithologies at Mike could help to provide constraints on PCA factors, and help to create better principal component factors for the two ore systems as well as helping to create better spatial distribution plots using 3D modeling software, such as LeapFrog Geo.

Deposit Model

The prevailing deposit model for the Mike deposit, proposed by Bawden (2001) and Norby and Orobona (2002) hypothesized a Cretaceous porphyry as the source of copper, lead, and zinc mineralization. This was followed by Eocene mineralization of Carlin-type gold hosted within carbonate replacement concentrated along the Good Hope fault and cross cutting, lesser, normal faults. Later uplift and erosion lowered the water table, providing at least two episodes of oxidizing conditions. Oxidation of pyrite allowed for the remobilization and concentration of copper and zinc due to supergene processes, forming lobes and horizons of copper oxide mineralization, including an abundance of chonicalcite due to the overwhelming amount of arsenic present within Carlin-type pyrites. Continued uplift and erosion exposed Paleozoic basement rocks of the Rodeo Creek unit and Roberts Mountain formation which were then buried by Tertiary Carlin formation.

Petrographic observations from this thesis study, however, challenge the original proposed timing of copper-base metal mineralization at Mike in relation to the Carlin gold mineralization. Where copper, zinc, and lead base metals are seen in conjunction with Carlin-type mineralization, base metals appear to be later.

According to Ressel and Henry's work on igneous geology of northeastern Nevada (2006), a plutonic complex below the Carlin trend is needed to account for the abundance of Eocene igneous rocks in the area. This complex is hypothesized to have been emplaced over a period of about 4 million years and is thought to be 50 km long and between 12 and 23 km wide, coincident with the northern and central Carlin trend, and underlies an area of approximately 1,000 km² (Ressel and Henry, 2006).

Based on the data from this thesis, predominantly the petrography, SEM work, and stable isotopes, base metal mineralization occurred post-Carlin deposition. An alternative model to Norby and Orobona's model for the generation of the Mike deposit is the emplacement of central Carlin trend structures including the Good Hope fault, north striking normal faults, and northeast cross cutting faults. Carlin gold mineralization occurred along major and minor structures within favorable sub lithologies within the Roberts Mountain formation, Popovich formation, and Rodeo Creek unit. The Roberts Mountain thrust acted as an impermeable cap for fluids to deposit under. A later, annular shaped intrusive body, possibly genetically related to Ressel and Henry's proposed plutonic batholith, was emplaced to the north-northwest of the present Mike deposit. Mineralizing fluids followed district scale structures and deposited chalcopyrite, sphalerite, and galena. The abundance of lead and zinc is likely due to the distal nature of the deposit in relation to the stock (John et al., 2010). Metasomatic and metamorphic products also occur around this time, creating low temperature calc-silicate assemblages that include wollastonite-chondrodite and vesuvianite-magnetite skarns as well as epidote-carbonate-diopside hornfels, other calc-silicate hornfels, and silica hornfels where parent rocks were predominantly siliciclastic. Changes in paleo water table levels allowed for the oxidation of Carlin-type pyrite and base metal sulfides, which allowed for the supergene process, described in detailed by Bawden (2002), and the enrichment of copper in the form of oxides and arsenates as well as zinc, both in association with limonite and biogenic sphalerite. Tilting, uplift, erosion, and burial proceeded.

References

- Branham, A., and Arkell, B., 1995, The Mike gold-copper deposit, Carlin Trend, Nevada
in Hagni, R., ed., Process Mineralogy XIII: Applications to Benefaction
Problems, Pyrometallurgical Products, Advanced Mineralogical Techniques,
Precious Metals, Environmental Concerns,. Ceramic Materials, Hydrometallurgy,
and Minerals Exploration: The Minerals, Metals, and Materials Society, p. 203-
211.
- Bawden, T.M., 2002, Supergene enrichment of copper at the Mike gold deposit, Carlin
Trend, Nevada. M.S. thesis, Stanford University.
- Bawden, T.M., Einaudi, M.T., Bostick, B.C., Meibom, A., Wooden, J., Norby, J.W.,
Orobona, M.J.T., Chamberlain, C.P., 2003, Extreme ³⁴S depletions in ZnS at the
Mike gold deposit, Carlin Trend, Nevada: evidence for bacteriogenic supergene
sphalerite: *Geology*, October, 2003, v. 31, no. 10, p.913-916.
- Cline, J.S., Hofstra, A.H., Muntean, J. L., Tosdal, R. M., Hickey, K. A., 2005, Carlin-
type gold deposits in Nevada: Critical geologic characteristics and viable models
in Hedenquist, J. and Thompson, J., eds., 100th Anniversary Volume: Society of
Economic Geologists, Littleton, CO, p. 451-484.
- Cohen, J. F., 2012, Footprints of porphyry Cu deposits: Vectors to the hydrothermal
center using mineral mapping and lithogeochemistry. MS thesis, Oregon State
University.
- Dickinson, W.R., 2006, Geotectonic evolution of the Great Basin: *Geosphere*, v. 2; no. 7;
p. 353–368

- Emsbo, P., Hutchinson, R. W., Hofstra, A. H., Volk, J. A., Bettles, K. H., Baschuk, and G. J., Johnson, C. A., 1999, Syngenetic Au on the Carlin trend: Implications for Carlin-type deposits: *Geology*, v. 27, no. 1, p. 59-62.
- Groves, David I., Mair, John L., Vielreicher, Richard M., and Hart, Craig J.R., 2005, The lithospheric setting of Carlin-type deposits: An important clue to their genetic associations and deposit associates, *in* Rhoden, H.N., Steininger, R.C., and Vikre, P.G., eds., Geological Society of Nevada Symposium 2005: Window to the World, Reno, Nevada, May 2005, p. 1-11.
- Guilbert, J.M., and Park, C.F., 1986, Porphyry base-metal deposits, *in* Guilbert, J.M., and Park, C.F., *The geology of ore deposits*, 1986, pp. 405-452.
- Henry, C. D., Faulds, J. E., Boden, D. R., Ressel, M. W., 2001, Timing and styles of Cenezoic extension near the Carlin Trend, northeastern Nevada: Implications for the formation of Carlin-type gold deposits: Geological Society of Nevada Special Publication No. 33, p. 115-128.
- Hofstra, A.H., and Cline J.S., 2000, Characteristics and models for Carlin-type gold deposits: Review in *Economic Geology*, v. 13, p. 163-220.
- John, D.A., Ayuso, R.A., Barton, M.D., Blakely, R.J., Bodnar, R.J., Dilles, J.H., Gray, Floyd, Graybeal, F.T., Mars, J.C., McPhee, D.K., Seal, R.R., Taylor, R.D., and Vikre, P.G., 2010, Porphyry copper deposit model, chap. B of Mineral deposit models for resource assessment: U.S. Geological Survey Scientific Investigations Report 2010-5070-B, 169 p.
- Large, R.R., Danyushevsky, L., Hollit, C., Maslennikov, V., Meffre, S., Gilbert, S., Bull, S., Scott, R., Emsbo, P., Thomas, H., Singh, B., and Foster, J., 2009, *Geology and*

trace element zonation in pyrite using a laser imaging technique: implications for the timing of gold in orogenic and Carlin-style sediment-hosted deposits: *Economic Geology*, v. 104, p. 635-668.

Larsen, B. R., 1994, Internal petrographic report, Newmont Mining Corp.

Mathur, R., Titley, S., Barra, F., Brantley, S., Wilson, M., Phillips, A., Munizaga, F., Makseav, V., Vervoort, J., Hart, G., 2009, Copper isotope fractionation used to identify supergene processes, *Society of Economic Geologists Special Publication* 14, p. 45-49.

Mathur, R., Dendas, M., Titley, S., Phillips, A., 2010, Patterns in the copper isotope composition of minerals in porphyry copper deposits in southwestern United States, *Economic Geology*, v. 105, p. 1457-1467.

Norby, J.W., and Orobona, J.T., 2002, Geology and mineral systems of the Mike Deposit: Nevada Bureau of Mines and Geology Bulletin 111. p. 143-167.

Patterson, L. M. and Muntean, J. L., 2011, Multi-element geochemistry across a Carlin-type gold district: Jerritt Canyon, Nevada: in Steininger, R. C. and Pennell, W. M. (eds.), *Great Basin Evolution and Metallogeny: Geological Society of Nevada 2010 Symposium Proceedings*, Reno, p. 1119-1152.

Roberts, R.J., Hotz, P.E., Gilluly, J., and Ferguson, H.G., 1958, Paleozoic rocks of northcentral Nevada: *American Association of Petroleum Geologists Bulletin*, v. 42, no. 12, p. 2813-2857.

Teal, L. and Branham, A., 1997, Geology of the Mike Gold-Copper Deposit, Eureka County, Nevada in Vikre, P., Thompson, T.B., Bettles, K., Christensen, O.D., and Parratt, R. eds. *Carlin-type Gold Deposits Field Conference: Society of Economic*

Geologists Guidebook Series, v. 28, p. 257-276.

Thompson, T.B., 2011, Origins of fluids associated with Carlin-type ore systems, Great Basin Evolution and Metallogeny: Geological Society of Nevada 2010 Symposium Proceedings, Reno, p. 201-219.

Titley, S. R., 1982, The style and progress of mineralization and alteration in porphyry copper systems, southwestern North America: Tucson, Univ. Arizona Press, p. 93-116.

Wang, J.Z., Li, J.W., Zhao, X.F., Ma, C.Q., Qu, W.J., Du, A. D, 2008, Re-Os dating of pyrrhotite from the Chaoshan gold skarn, eastern Yangtze craton, eastern China: International Geology Review, v. 50, p. 392-406.

Wells, J.D., and Mullens, T.E., 1973, Gold-bearing arsenian pyrite determined by microprobe analysis, Cortez and Carlin gold mines, Nevada: Economic Geology, v. 68, pp. 187-201.